UNIVERSITY OF SOUTHAMPTON

Marine high-resolution reflection seismology:

acquisition, processing and applications

Rory Quinn

A thesis submitted for the degree of
Doctor of Philosophy

Department of Geology
Southampton Oceanography Centre
Faculty of Science

December 1997

UNIVERSITY OF SOUTHAMPTON

ABSTRACT

FACULTY OF SCIENCE

DEPARTMENT OF GEOLOGY

Doctor of Philosophy

MARINE HIGH-RESOLUTION REFLECTION SEISMOLOGY: ACQUISITION, PROCESSING AND APPLICATIONS

Rory Quinn

The primary aim of this research is to assess the application of Chirp technology to marine archaeology. The development of acquisition, processing and modelling methodologies for evaluating sites of archaeological interest on and below the seabed are discussed.

Chirp frequency-modulated systems offer pre-determined, repeatable source-signatures for high-resolution, normal incidence seismic reflection data acquisition. The design and application of an optimal processing sequence for Chirp sub-bottom data demonstrates the importance of a detailed knowledge of the source-signature. Improvement of greater than 60 dB in signal-to-noise ratio is obtained from correlating the frequency-modulated reflection data with the transmitted pulse. Effective deterministic deconvolution of correlated data is achieved by the application of an inverse filter designed on the Chirp Klauder wavelet. Interpretability of deconvolved data is enhanced by the calculation of instantaneous amplitudes. Signal-to-noise ratio and reflector continuity are increased by the application of predictive filters whose performance is aided by the repeatability of the Chirp source-signature.

The limits of vertical resolution (R_v) and horizontal resolution (R_h) of Chirp sources are defined by: $\frac{2}{\Delta f} \geq R_v \geq \frac{1}{\Delta f}$ and $\frac{V_p twt}{2} \tan\frac{\theta}{2} \geq R_h \geq \frac{V_p}{2}\sqrt{\frac{twt}{f_d}}$ respectively, where Δf is the bandwidth of the reflection data, V_p the compressional wave velocity, twt the two-way travel time to the reflector, θ the beam-angle of the Chirp source and f_d the dominant frequency component in the recorded data.

Buried wooden artefacts can be readily imaged by Chirp-sourced reflection seismology. Compressional wave velocity parallel to the wood grain (V_L) is consistently faster than that across-grain (V_R and V_T). Theoretical and experimental predictions of reflection coefficients (K_R) calculated for wood buried in unconsolidated marine sediments are typically large and negative (K_R = +0.27 to -0.79; K_{Roak} = -0.03 to -0.64). Variations in K_R are dependent upon the burial-sediment, wood species and structural coherency of the artefact.

Synthetic modelling demonstrates that small changes in the seafloor impedance profile causes random switches in the polarity of the Chirp pulse. Reflection coefficients are calculated from Chirp sub-bottom data using amplitude-time relationships and polarity information derived from trace-mixing. Calculations from Chirp data acquired over a partially buried 17th Century oak wreck provide an average K_R of -0.26, in agreement with the predicted range.

A pseudo 3-dimensional Chirp survey of the excavated *Mary Rose* wreck site (East Solent, UK) identified two *brightspot* anomalies, buried to a depth of 4-5 m, trending east-west adjacent to the western margin of the excavation hole. These anomalous reflectors are interpreted as infilled palaeo-scour features associated with the wrecking and subsequent degradation of the *Mary Rose*. Fill material comprises wreck fragments and coarse sediment sourced from the ship's ballast. Longitudinal scour features were previously unrecognised on the site, and represent the first time such palaeo-scour marks have been recognised in the sedimentary record.

Integrated Chirp and side-scan sonar surveys of the *Invincible* site (East Solent, UK) demonstrate the capability of high-resolution acoustic techniques to: identify the extent and coherency of semi-exposed wrecks, determine the wrecking history of a site and act as an effective management tool. The distribution of wreck material is primarily controlled by storm-associated wave action, depositing the bulk of fragmented wreck-structure to the north and north-east of the *in-situ* port side. Evidence suggests that current site stability is controlled by a combination of tidally induced currents and anthropogenic activity.

Table of contents

Acknowledgements

Special thanks to my supervisors, Dr. Jon Bull (Geology) and Dr. Justin Dix (Oceanography), for their guidance, encouragement and discussion over the past three years. I am indebted to Jon Adams (Archaeology) whose insight was invaluable in this project. This research is funded by NERC Grant GR3/9533.

The comments of manuscript reviewers improved the style and content of the work presented within: Professor A.H. Stride, Dr. J. Alexander, Dr. H. Chamley and anonymous reviewers. Thanks to Dr. Laurence Hopkinson (SOC), Dr. Tim Minshull (Bullard Labs, Cambridge University), Dr. Bob Whitmarsh (SOC) and Dr. Neil Kenyon (SOC) for reviewing parts of this thesis.

Thanks to GeoAcoustics Ltd., Great Yarmouth, UK for kind permission to publish the Chirp source-signature, support over the three years and the ready availability of equipment. Thanks to Dr. Tony Briscoe and Dr. Roger Pinnington of the Institute of Sound and Vibration Research (University of Southampton) for helpful discussion.

Many members of the archaeological community offered valuable discussion and dive-time over the past three years: Professor David Peacock (Archaeology Department, University of Southampton); Alex Hildred and Chris Dobbs (Mary Rose Trust); Chris Underwood (NAS); Sarah Draper, Brian Sparks and Gary Momber (Hants and Wight Trust for Maritime Archaeology); John Bingeman (Government Licensee, *Invincible* site) and Arthur Mack. Special thanks to Dave Burden who acted as skipper and provided many knots and moments of know-how.

I also thank many members of the Geology Department who helped in this research and life in general, especially: Dom & Jo, Eta, Gavin, George, Giles, Joe, Laurence, Paul, Rakesh, Rob & Megan, Robin and Steve.

To my parents and Gráinne and Conor for unfaltering support and belief.

"All that's constant
Is the fact of change:
Pearl of love; grit of pain."

Seán Dunne (Letter to Lisbon, 1996)

Rory
December 1997

Chapter 1

Introduction

1.1 *Introduction*

Since the development-led boom in rescue archaeology in the 1960s and 1970s, the nature of funding and a growing recognition of the non-renewable nature of the archaeological resource, have prompted more circumspect attitudes to excavation (Cleere, 1989; Hunter and Ralston, 1993). Over the past three decades, emphasis in land-based archaeology shifted towards the use of laboratory instrumentation to analyse human cultural artefacts and performing site evaluations in advance of land development (Wynn, 1986). Time required to excavate entire sites had become a luxury archaeologists can no longer afford. To redress the need for manual excavation, a rapid method of non-destructively evaluating a site was required. Land-based archaeologists began using high-resolution geophysics as early as the 1940's (Wynn, 1986) as a rapid, non-invasive technique to investigate archaeological sites under threat from development. A similar situation exists today in marine archaeology as that which existed in land-based archaeology in the 1960's.

The sole legislation governing the treatment of underwater maritime sites in British waters is The Protection of Wrecks Act 1973. This Act empowers Government to designate by Order the site of what is, or what may prove to be, the wreck of a vessel which it considers should be protected from unauthorised interference because of its historical, archaeological or artistic importance. Currently, 42 sites within the UK are designated under the Act. The Order identifies the site and extent of the restricted area in which certain activities are prohibited except under the authority of a licence issued by Government agencies (ADU, 1997).

In the present climate, social and environmental concerns have created political pressures, typically manifested as recommendations to government concerning the protection and monitoring of all underwater archaeological sites. In 1989, the Joint Nautical Archaeology Policy Committee (JNAPC) voiced these concerns in a series of recommendations to Government, outlining the disparity between the protection of archaeological sites on land and underwater. One of the recommendations highlighted by the JNAPC (1989) is: *Commercial seabed operators and statutory undertakers active on the seabed should be encouraged to carry out archaeological implication surveys before the seabed is disturbed and co-operate with archaeologists during potentially destructive work. They should be encouraged to contribute to the costs of rescue excavation of threatened sites.*

The Department of Environment's Planning Policy Guidance Note (PPG) 16, Archaeology and Planning (1990), states that: *Archaeological remains should be seen as a finite and non-renewable resource, in many cases highly fragile and vulnerable to damage and destruction. In particular, care must be taken to ensure archaeological remains are not needlessly or thoughtlessly destroyed. They contain irreplaceable information about our past*

and the potential for an increase in future knowledge. They are part of our sense of national identity and are valuable both for their own sake and for their role in education, leisure and tourism.

Although PPG 16 is concerned with the terrestrial archaeological resource, PPG 20 (1992), which covers planning policy for the coastal areas of England and Wales, implies PPG 16 is relevant below the low water mark, outlining that: *the coastal zone ... has a rich heritage above and below water.* Thus, while there is no legal obligation for developers to undertake archaeological evaluations prior to offshore development, the implication is that the marine archaeological resource is as valuable and vulnerable as that on land, and should be treated with equal respect.

A rapid, inexpensive method of surveying underwater archaeological sites is needed prior to development within the coastal zone. Marine archaeology budgets tend to be relatively small and usually insufficient to fund independent development of new instruments (Mazel, 1985). Instead, the field often has to "borrow" technology from outside disciplines.

Over the past three decades, a range of seismic reflection techniques have been deployed in the search for sites of archaeological interest in the marine environment (Frey, 1971; Redknap 1990). During this period, relative success has been met with the use of high-resolution side-scan sonar and echosounder systems to identify archaeological artefacts lying on the seabed (Caston, 1979; Hobbs *et. al.* 1994). Such systems are limited however, as they cannot penetrate the subsurface and are therefore unable to image buried artefacts. In consequence, a number of workers have used sub-bottom profiling systems in an attempt to image buried features (Rao, 1988; Chauhan and Almeida, 1988). The suitability of these systems has been restricted by poor resolution and navigational control, ineffectiveness in shallow waters and the absence of any form of post processing of the raw seismic data. Table 1.1 lists the typical frequency content, vertical resolution and penetration of conventional sub-bottom profiling systems.

System	Frequency (kHz)	Vertical Resolution (m)	Penetration (m)
Pinger	3 - 12	0.2	10 - 40
Boomer	1 - 5	0.5 - 1	50 - 100
Sparker	0.1 - 1	2	100 - >1,000

Table 1.1: Typical frequency content, vertical resolution and penetration of conventional sub-bottom profiling systems (After Kearey and Brooks, 1991).

Recent advances in acquisition and processing technology have culminated in the development of a system known as *Chirp*, a high-resolution, digital, frequency-modulated (FM) sub-bottom profiling system. Chirp systems offer vertical resolution on a decimetre scale within the top 30 to 40 m of unconsolidated sediment, the capability to operate in shallow water depths,

and the acquisition of sub-bottom data in SEG-Y format which allows straightforward transfer to off-line processing packages. When Chirp systems are utilised in conjunction with DGPS (Differential Global Positioning System) and consistent survey methodologies, navigational accuracy of +/- 1m is attainable.

1.2 *Scope and objectives*

The primary objective of this thesis is to assess the application of Chirp technology to marine archaeology. The development of acquisition, processing and modelling methodologies for evaluating sites of archaeological interest on and below the seabed are discussed. Chapters 4, 5, 7 and 8 comprise manuscripts submitted to archaeological and geophysical journals (references to these papers are made as footnotes at the beginning of each chapter). Chapters 3 and 5 investigate characteristics of Chirp sub-bottom data using single-trace synthetic models. Due to this thesis structure, some repetition occurs in the introduction and discussion sections of chapters.

Chapter 2 details survey methodologies and parameters used in the acquisition of data presented in this thesis. Particular reference is made to the acquisition of Chirp sub-bottom data. The vertical and horizontal resolution of Chirp sources are discussed in Chapter 3. This aspect of the system is particularly pertinent as the vertical resolution of conventional sub-bottom systems is inadequate to image and assess buried archaeological material in the marine environment. Synthetic models are presented to compare to accepted criteria for vertical resolution. The effects of sediment attenuation on the frequency content of Chirp data and the resolution of Chirp systems is outlined. Chapter 4 details an optimal processing sequence for Chirp sub-bottom data. One of the major advantages of Chirp systems over conventional sub-bottom profilers is that they transmit a pre-determined, repeatable waveform which aids post-processing, interpretability and quantitative data analysis.

Prior to this research, no work has been conducted on imaging buried wooden material utilising marine reflection seismology. The likelihood of imaging wooden artefacts utilising Chirp sources is discussed in Chapter 5. Theoretical reflection coefficients of different wood species buried in unconsolidated marine sediments are calculated and experiments on wooden samples from a 16th Century oak wreck are used to validate the theory. A method for estimating reflection coefficients directly from sub-bottom data is outlined in Chapter 6 using Chirp data from a 17th Century oak wreck. The effects of a geoacoustically layered seafloor on the polarity of the Chirp pulse is modelled using single-trace synthetic seismograms, and implications of polarity switches in the calculation of reflection coefficients are outlined.

The final two chapters present case studies of Protected wreck-sites within the East Solent, UK. Chapter 7 details the results and interpretation of a pseudo 3-dimensional Chirp survey of the tidally dominated *Mary Rose* wreck site. The second case study, presented in Chapter 8, discusses the effectiveness of repeated Chirp and side-scan surveys over vulnerable archaeological sites within the coastal zone. Conclusions are drawn about the applicability of

Chirp technology to marine archaeology and the effectiveness of high-resolution reflection seismology as a management tool for marine archaeology.

Chapter 2

Data acquisition and survey methodology

2.1 *Introduction*

Chirp systems use recent developments in powerful and affordable digital electronics and desktop computing facilities to aid processing and acquisition techniques to produce high-quality, high-resolution sub-bottom images in real time. Chirp swept-frequency sources typically operate in a range of 1-15 kHz, and offer vertical resolution on a decimetre scale in the top *circa* 30 m of unconsolidated marine sediments. Combined digital, high-resolution sub-bottom and side-scan data acquisition, in conjunction with consistent survey methodologies, can provide a suite of data to assist with the interpretation of the shallow geology and marine archaeology in the near coastal zone.

Data acquisition and marine geophysical survey methodologies are discussed in this chapter. Particular reference is made to the acquisition of Chirp sub-bottom data and the navigation systems available to the surveyor. The acquisition of side-scan sonar data is well documented (Clay, 1977; Fish and Carr, 1990) and is not discussed here.

2.2 *Data acquisition*

2.2.1 *Chirp technology*

Chirp profilers are digital, frequency-modulated (FM) sources with a pre-determined and repeatable source signature for high-resolution, normal incidence seismic reflection data acquisition. Chirp systems generate wideband quantitative acoustic data that can be used for sediment classification and estimation of sediment physical properties (Schock and LeBlanc, 1990). The original system was developed at the University of Rhode Island (URI) under a research programme which began in 1981, funded by the Office of Naval Research (Schock and LeBlanc, 1990).

Schock and LeBlanc (1990) showed that the performance of off-the shelf sub-bottom profilers (*e.g.* boomers, pingers) was inadequate for performing quantitative measurements of the seafloor. The main problems associated with conventional systems include poor pulse repeatability, poor signal-to-noise ratio (SNR) of recorded data, inadequate vertical resolution and uncalibrated and non-linear electronics. In order to redress these shortcomings, a real-time digital sub-bottom system was designed at URI between 1985 and 1989 (Schock and LeBlanc, 1990).

Chirp systems comprise calibrated, linear electronic components and ensure a repeatable source signature by transmitting FM pilot signals containing pre-determined phase and amplitude corrections, ensuring no anomalies occur in the transducers or the transmitting and receiving electronics. The SNR of Chirp data is improved through matched filter processing

by correlating the reflection data with the pre-determined transmitted pulse. If reflections or noise do not match the outgoing Chirp waveform, the filter attenuates the unwanted signal. The wide bandwidth of Chirp systems limits the classic trade-off between penetration and vertical resolution in the sub-bottom by transmitting a range of frequencies, ensuring optimum penetration *and* resolution. The effective resolution of Chirp wideband sources is discussed in detail in Chapter 3.

Figure 2.1 displays an example of the linearly-swept Chirp pulse, together with its power spectrum. A typical Chirp sub-bottom profile is shown in Figure 2.2.

2.2.2 *University of Southampton Chirp system*

The University of Southampton Chirp system is a modified GeoAcoustics GeoChirp Model 136A towed transducer system. Individual components and system specifications are outlined in Table 2.1 and discussed below in more detail.

Sub-sea	**Tow Fish**	• Model 136A • Surface tow catamaran
	Transducers	• 4 model 137D transducers
	Hydrophone	• Mini-streamer with built-in pre-amplifier • Bandwidth: 500 Hz to 15 kHz
	Sub-sea electronics bottle	• Chirp generation & power amplifier. • Power output: 400 W • Depth rating: 600 m
	Transmitted signal	• *Pulse length*: 16 or 32 ms • *Frequency*: 2-8 or 1.5-11.5 kHz
	Tow cable	• Multi-core soft deck cable • Multi-core armoured cable
Surface electronics	**Profiling Unit**	• Provides the main processing facilities • Multi-pin connector provides all power and signal interconnections to sub-surface electronics and towfish. • Trigger provides a divided profiling rate. • Power: 2000 W maximum
	Sonar Enhancement System	• SE881 workstation. • Video display monitor. • GUI interface operator terminal. • Thermal line-scan recorder. • Two helical scan 8mm tape drives. • Internal and external hard disks

Table 2.1: Technical specification of the Southampton University GeoChirp profiling system.

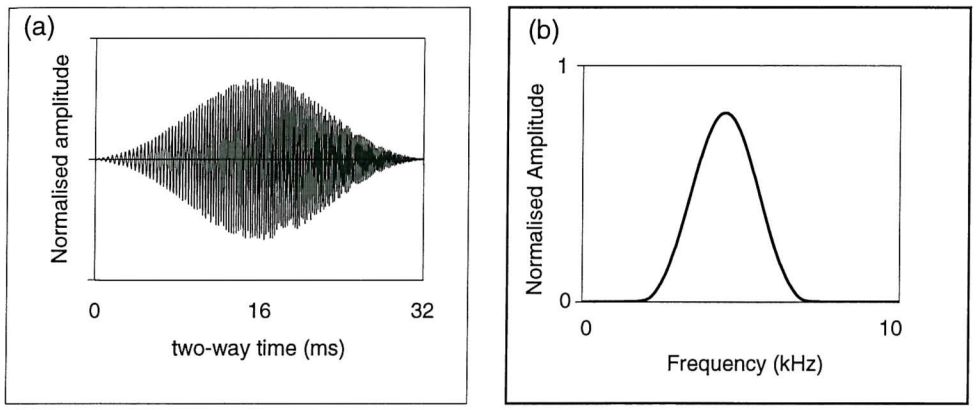

Figure 2.1: (a) An example of a 32ms, swept-frequency Chirp pulse; (b) The associated power spectrum.

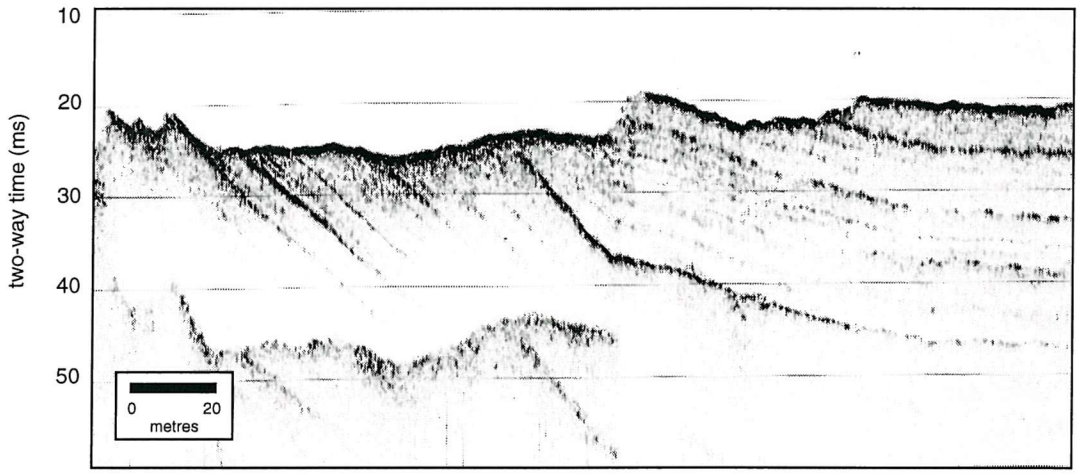

Figure 2.2: Typical Chirp profile acquired over Hamstead Ledge, West Solent, UK. Data acquired ustiling a GeoAcoustics GeoChirp Model 136A towed transducer system, transmitting a 32ms, 2-8 kHz swept-frequency source at a transmit rate of 4 pulses per second.

- *Sub-sea system (Figure 2.3)*

The GeoChirp is configured with the electronics bottle on the tow-fish and the receiving hydrophone attached and towed directly from the rear of the fish. The multi-core tow cable provides all power and signal connections between the surface processing system and the fish. Two tow fish options are available: the standard Model 136A tow fish (Figure 2.3a) and the surface tow catamaran (Figure 2.3b). Four Model 137D transducers are mounted on one of the above fish. The towed hydrophone comprises an 8-section mini-streamer and in-built power amplifier, with a bandwidth of 0.5 to 15 kHz (Figure 2.3c). The separate transmitting and receiving electronics preserves the linearity of the acquisition system and allows simultaneous transmission and reception (Schock *et al.*, 1994). All tow cable, transducers and hydrophone connections are provided by the sub-sea electronics bottle, which controls power amplification and Chirp generation. The transmitted Chirp signal may be varied in pulse-length (16ms or 32ms) and bandwidth (2-8kHz - high penetration mode; 1.5-11.5kHz - high resolution mode). Figure 2.4 a illustrates the basic towfish and surface electronics connections.

- *Surface electronics (Figure 2.4 b)*

Profiling Unit

The Profiling Unit (PU) controls the triggering and acquisition rates of the Chirp system. A single multi-pin connector provides all signal and power connections for the towfish via the deck and tow cables. The trigger rate, which can be varied from 1 to 10 pulses per second, is defined by the master clock and the divider on the profiling unit. Interconnections between the Profiling Unit and Sonar Enhancement System are via BNC cables.

Sonar Enhancement System

The Sonar Enhancement System (SES) is used for the acquisition, processing, display and digital storage of the Chirp data. The SES comprises a workstation with an OS-9^{TM} based operating system, video display monitor, an operator terminal with a graphical user interface (GUI), thermal line-scan recorder and two helical scan 8mm tape drives of 2.3Gb capacity. The SE881 workstation is the core of the SES system, comprising a power supply, processing boards, acquisition board, display board and hard disk drive for data-storage and system software. Digital data is acquired in SEG-Y format, enabling post-processing of sub-bottom data in industry-standard seismic processing software (Chapter 4). Data may be stored in uncorrelated or correlated format. The SES allows on-board processing of Chirp data, including bandpass filtering, bottom tracking, wave motion compensation and slant-range correction of side-scan sonar data.

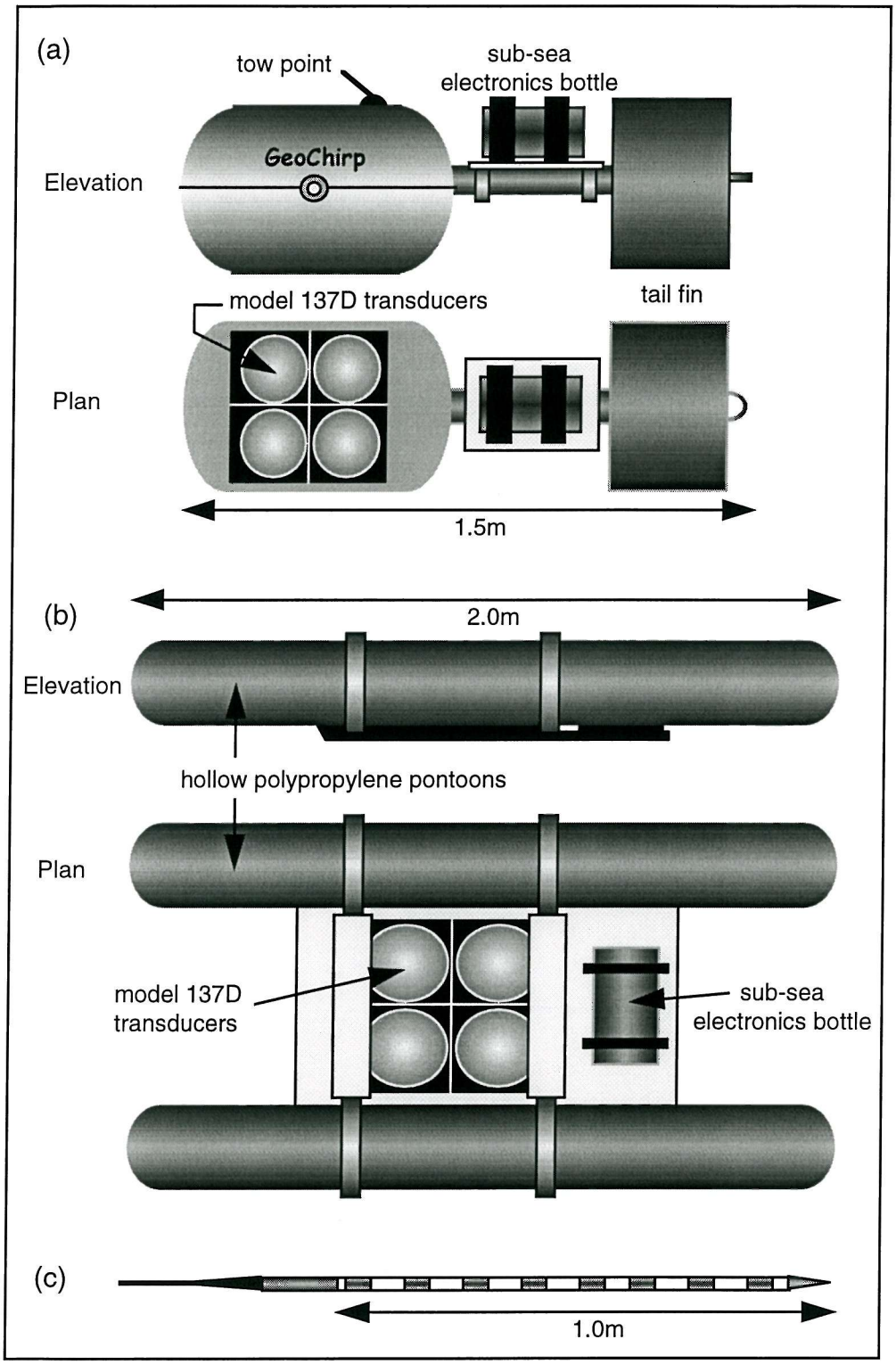

Figure 2.3: Diagram illustrating the main components of the GeoAcoustics GeoChirp acquisition system: (a) Model 136A towfish; (b) Catamaran deployment; (c) 8-section, neutrally buoyant mini-streamer.

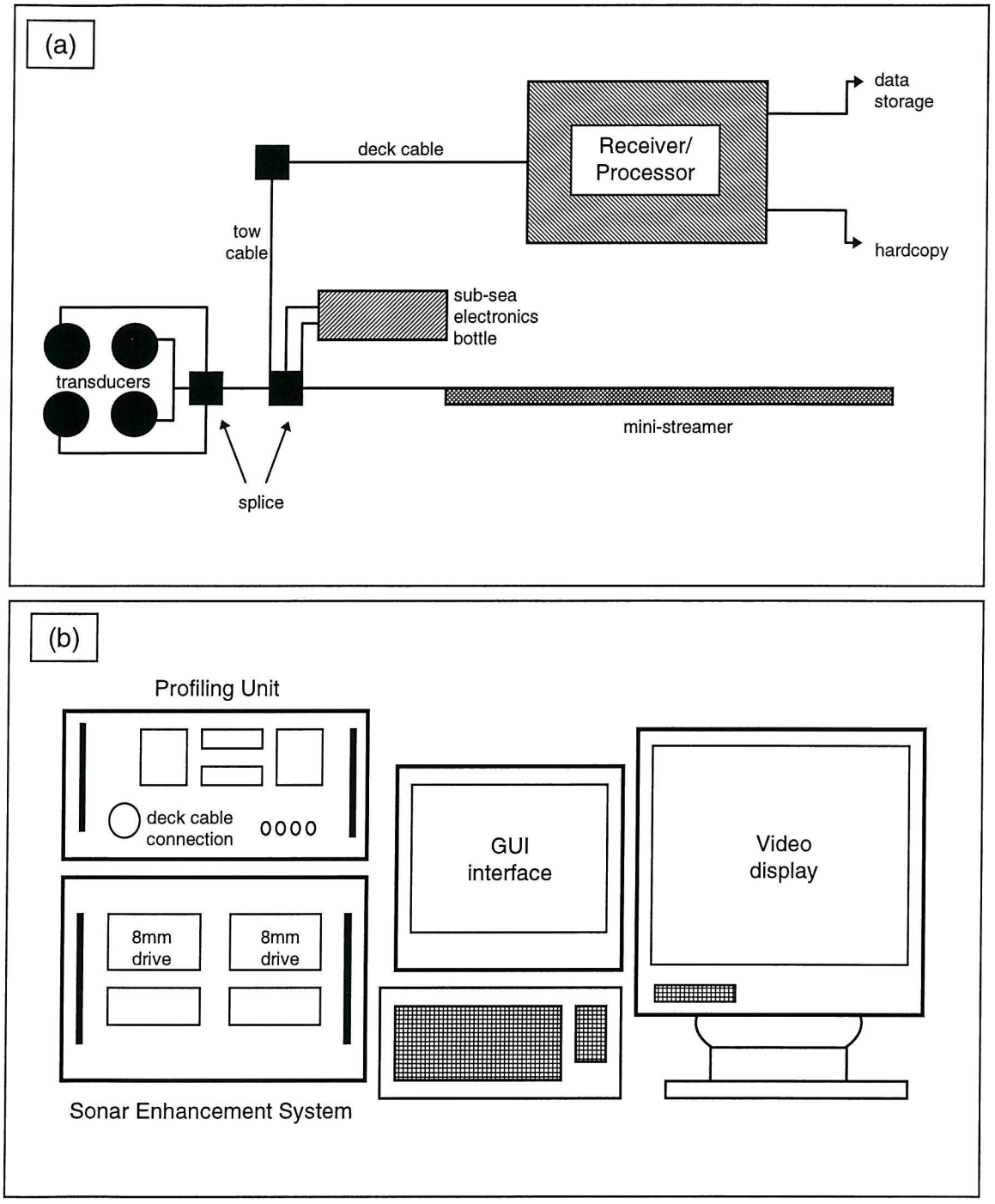

Figure 2.4: (a) System block diagram of the GeoAcoustics GeoChirp profiling system. (b) Diagram of the main surface electronics components - profiling system, sonar enhancement system, GUI interface and video display monitor.

- *Chirp calibration*

Calibration of the Chirp system is conducted in the acoustic test facility (a water-filled wooden vat) at GeoAcoustics Ltd, Great Yarmouth. A perfect Chirp pulse is transmitted by the immersed transducers over the desired frequency range, reflected off the bottom of the vat and received by the hydrophone streamer. The received signal, which is distorted due to the frequency response of the transducers, receiver and the system electronics, is recorded and digitised. Analysis of the received signal allows a transfer function to be designed, which is in turn used to create an inverse function and applied to the transmitted Chirp waveform, thus compensating for the system non-uniform response. In this manner, the linearity of the system is preserved by compensating for the frequency response of the source and receiving electronics. An assumption in this iterative process is that system characteristics and the source-signature do not change with time. Experimental tests by GeoAcoustics Ltd. suggest that there is no change in the source-signature characteristics, but transducers and transducer-plate coupling characteristics are eventually modified over time.

2.2.3 *Chirp data acquisition*

Figure 2.5 summarises the acquisition and processing of Chirp sub-bottom data with noise-free synthetic illustrations. At the time of pulse transmission, an FM pilot signal containing predetermined phase and amplitude corrections is generated for the power amplifier. The output from the power amplifier is converted to the Chirp pulse (Figure 2.5 i) via the transducers mounted on the towfish. The transmitted pulse propagates through the water column, into the sediment pile and reflects from acoustic impedance contrasts in the sub-surface (represented by the impulse response of Figure 2.5 iii). Sub-bottom reflections are recorded by the mini-streamer and amplified before being digitised by an analogue-digital (A/D) converter. The recorded seismogram is:

$$x(t) = e(t) * s(t), \qquad (2.1)$$

where e(t) is the earth's impulse response and s(t) the transmitted Chirp pulse (Figure 2.5 iv). The digitised signal is subsequently processed by the SE881 workstation, correlating the digitised data with the transmitted waveform (Figure 2.5 v). Cross-correlation of the recorded seismogram with the Chirp pulse yields:

$$x'(t) = e(t) * w(t), \qquad (2.2)$$

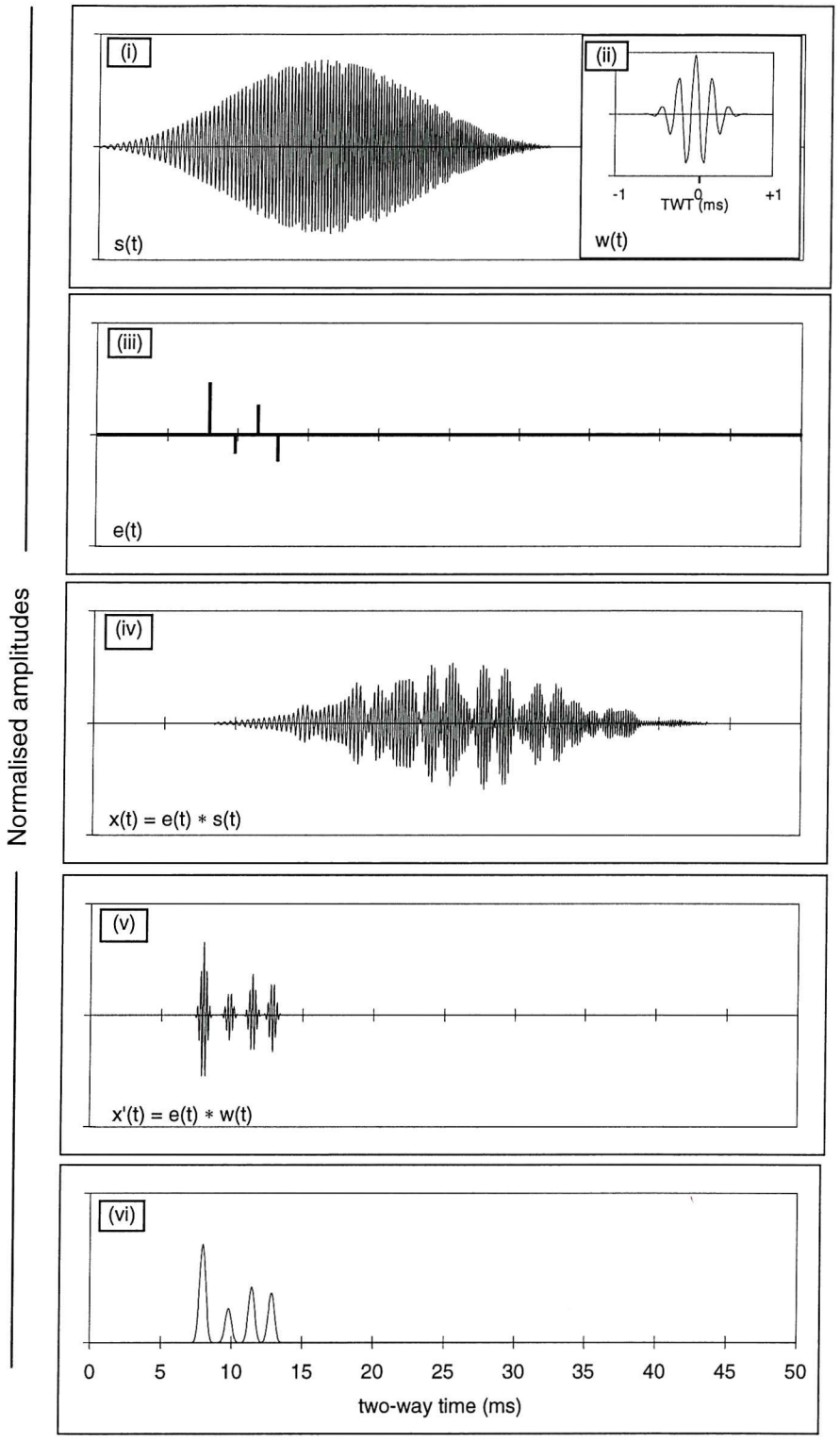

Figure 2.5: Synthetic data illustrating the convolution and correlation of Chirp data.
[i] s(t) = 32ms transmitted Chirp pulse
[ii] w(t) = s(t)∗s(t) = autocorrelation of the Chirp pulse (zero-phase Klauder wavelet)
[iii] e(t) = Impulse response
[iv] Recorded seismogram: x(t) = e(t)∗s(t)
[v] Correlated seismogram: x'(t) = e(t)∗w(t)
[vi] Instantaneous amplitude representation of the correlated seismogram.

where x'(t) is the correlated seismogram (Figure 2.5 v) and w(t) the zero-phase Klauder wavelet, *i.e.* the autocorrelation of s(t). Chirp data is normally displayed by calculating the instantaneous amplitude [R(t)][1] of the correlated data, where:

$$R(t) = \sqrt{x^2(t) + y^2(t)}\ , \qquad (2.3)$$

where x(t) is the signal and y(t) the quadrature (Taner, 1979; Yilmaz, 1987). The calculation of R(t) yields the seismogram displayed in Figure 2.5 vi.

2.2.4 *Navigation*

The Global Positioning System (GPS) is a constellation of 21 US military satellites orbiting 20,000 km above the earth's surface. The satellites transmit signals detailing their geographical positions, which can be read by suitable receivers, enabling users to ascertain their position to within 100 m accuracy. For many applications however, an accuracy of 100 m is insufficient. This inaccuracy in position fixing is termed *selective availability*, and is predominantly due to in-built random errors in satellite signals imposed by the US Department of Defence.

The accuracy can be improved upon utilising differential GPS (DGPS), by installing a GPS receiver at a known reference site on land. This enables errors in the GPS system to be determined by comparing observed and calculated ranges to the satellite constellation. The differential corrections can then be transmitted via a radio link to a second GPS receiver located on the survey vessel, improving the accuracy to a level of 1 to 10 m - depending on the quality of signal received by the reference station, terrain and the type of GPS receiver utilised by the surveyor. One problem with this set-up is that the surveyor is required to establish and maintain the reference receiver.

Radio Data System (RDS) is a method of transmitting data over an inaudible frequency-modulated (FM) subcarrier. RDS enables DGPS corrections to be broadcast over a wide geographical area. A network of GPS reference stations, located at 20 FM broadcast transmitters and 4 repeater stations, has been erected by C&MT Ltd. in the UK. The reference stations generate DGPS correction messages and transmit them in a piggy-back signal on the RDS sub-carrier, Classic FM. The name of this service in the UK is Focus FM. The majority of GPS receivers accept an industry standard DGPS correction known as RTCM SC104 and this is the format utilised by Focus FM. The main advantage of this service is that the user is not required to establish a reference station.

[1] The calculation of instantaneous amplitudes and its implications are considered in Chapter 4, Section 4.3.1.

2.3 *Survey methodology*

2.3.1 *Survey design*

Successful surveying is dependent upon good planning and consistent methodology. Prior knowledge of the following site-parameters is advantageous as they are important in the choice of survey equipment and vessel: seabed substrate, bathymetry, environmental conditions and orientation/type of archaeological structures/material. Ideally, information on all of these parameters is sought prior to survey; practically however, this type of information is not always available.

As outlined above, there are two choices for Chirp deployment - the sub-sea towfish and the surface-tow catamaran. Bathymetry, availability of survey vessels and site-location are the dominant controls of which deployment is utilised. The advantage of deploying the catamaran is that it does not require an on-board winch system and may be successfully deployed in water depths as shallow as 2m. The main disadvantage, however, is that in open-waters, the catamaran tends to be less stable than the towfish, and data-quality suffers from signal break-up. Conversely, the towfish deployment requires a mechanical winch system and cannot be deployed manually as the weight of the towfish exceeds 150 kg. However, the towfish is very stable in the water and suffers from less signal break-up.

Navigation is of utmost importance in marine geophysical surveying. Large-scale reconnaissance surveying is often conducted using stand-alone GPS receivers, whereas more detailed archaeological site surveys require DGPS systems. As outlined in Section 2.2.2, there are two options which provide positioning fixing on this scale: Focus FM or a self-maintained land reference station. The main advantage of the surveyor maintaining his own reference station is that it is a flexible, accurate and cost-effective system (providing a reference station is available to the surveyor); whereas the use of Focus FM is dependent upon subscription. The major disadvantages of self-maintained reference stations are signal range (typically <20 km) and interference from commercial radio users such as Taxi drivers and merchant shipping. Interference effects may cause the differential link to fail and abruptly end a planned survey - effectively wasting the cost of boat-hire and the surveyors time. Although the problem may be intermittent, it is unpredictable. The advantage of Focus FM is the permanent differential link, with a cost-dependent accuracy: premium rate (1-2 m); basic rate (10 m).

Both premium rate Focus FM and a self-maintained reference station have been used in the acquisition of navigation data presented in this thesis.

2.3.2 *Acquisition parameters and survey methodology*

Chirp and side-scan sonar data presented in this thesis were acquired using the parameters outlined in Table 2.2 and the surface electronics configuration in Figure 2.6 a and b. Acquisition parameters and trigger rates are listed in the introductory sections of the relevant chapters.

Trigger source	External (Triggered from Profiling Unit)
Trigger rate	4 pulses per second
Channel allocation	0 = Uncorrelated Chirp 1 = Correlated Chirp 2 = Sidescan port transceiver 3 = Sidescan starboard transceiver
Non-delayed window	Channels 0, 2, 3 (0-96 ms)
Delayed window	Channel 1 (96-229 ms)
Sample Period	40 μs
Chirp pulse	2-8 kHz
Side-scan frequency	100 kHz

Table 2.2: Parameters input into the Analogue Menu of the SES and Profiling Unit for the acquisition of Chirp (correlated and uncorrelated) and digital side-scan data.

Using these parameters, the trigger signal for both the Chirp and side-scan systems is derived externally from the Profiling Unit. Channel 0 has a user-defined 10 dB gain amplification for the acquisition of uncorrelated Chirp data. It is recommended that a standard channel configuration is used, as it makes set-up and connections more consistent. The sample period is determined by the source signal bandwidth. For the maximum source frequency of 11.5 kHz, the Nyquist is 43 μs, therefore a sampling rate of 40 μs ensures the returned signal is not aliased. Channel 1 is used to record correlated Chirp data, and has a user-defined delay time of 96 ms which corresponds to the system response time of correlating the sub-bottom data with the source-signature.

2.3.3 *Data storage*

Two options are available for data storage - two 8mm dual scan helical tape drives and a choice of an internal (500 Mb capacity) and external (1Gb capacity) hard disk. Each 8mm tape, with a 2.3Gb capacity, equates to between 4 and 25 survey hours depending on data density. The advantage of recording directly to tape is the amount of space accessible. The disadvantages include a time delay in the start and end of recording and slow play-back time which can be a problem when reviewing data on-board the survey vessel. Conversely, recording directly to hard disk ensures immediate writing and play-back of data, but is limited by the size of the disk.

Acquisition of data in SEG-Y format ensures the transfer of data to off-line processing and interpretation packages is straightforward. The optimal processing of Chirp sub-bottom data is discussed in detail in Chapter 4. The main advantages of digital data acquisition include improvement in sub-bottom and side-scan data quality through post-processing and the ability to quantitatively analyse the geophysical signature of anthropogenic material. All

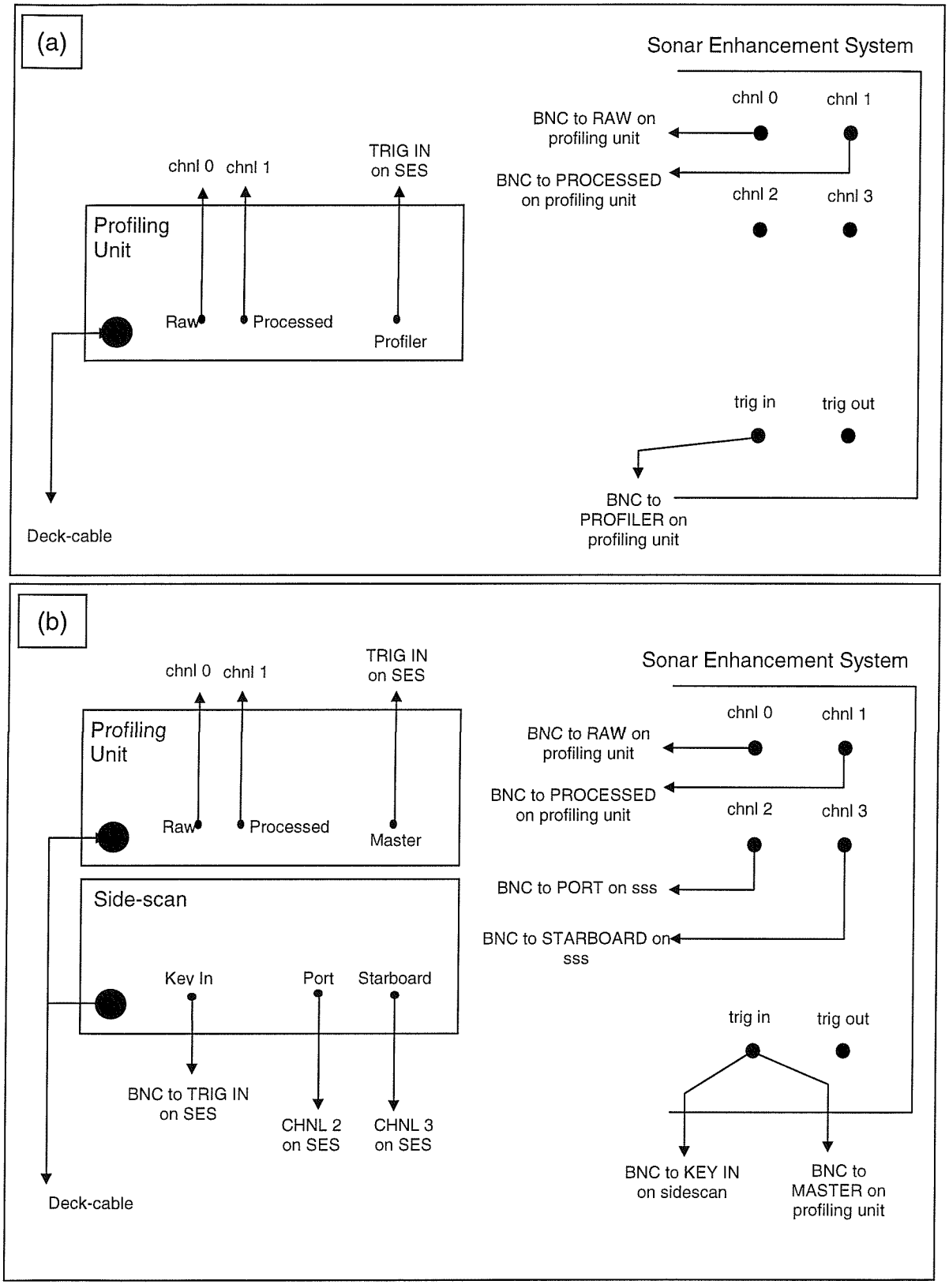

Figure 2.6: Illustration of the surface electronics configuration for the acquisition of: (a) Chirp uncorrelated and correlated sub-bottom data (b) Chirp correlated and uncorrelated sub-bottom data and digital side-scan sonar data.

post-processing of Chirp data presented in this thesis was conducted in the ProMAX^{TM} 6.0 software package (Advance Geophysical Corporation) mounted on a Sun Ultra workstation.

Chapter 3

The effective resolution of Chirp sources

3.1 *Introduction*

Seismic resolution limits define how close two points can be in the sub-surface, yet still be distinguished. In this chapter, both vertical and horizontal (or lateral) resolution of Chirp sources are considered.

Synthetic models, examining the seismic response of convolving the zero-phase Chirp Klauder wavelet (Figure 3.1) with two spikes of increasing separation distance, are presented as a control on the vertical resolution of Chirp sources. Comparisons are made between the results of this modelling exercise and the accepted criteria for vertical resolution as outlined by Rayleigh (Jenkins and White, 1957), Ricker (1953), Widess (1973) and Kallweit and Wood (1982). The discussion on horizontal resolution of Chirp sources compares the resolution predicted by the Fresnel Zone to that predicted by the frequency dependent beam angle of Chirp sources. The final section in this chapter discusses the effects of sediment attenuation on the effective resolution of chirp sources.

Figure 3.2 illustrates the notation used throughout this discussion. All calculations and modelling exercises conducted in this chapter are for a 2-8 kHz Chirp source {f_d = 5 kHz, and band ratio (f_u/f_l) of 2 octaves)} of 32 ms duration, sampled at a rate of 40μs and transmitted by an array of 4 transducers with a beam angle of 45°. Generalised results relating to Chirp sources are inferred from these exercises.

3.2 *Vertical resolution (R_v)*

3.2.1 *Introduction*

Vertical seismic resolution describes how closely two points can be in a vertical plane, yet still be distinguished. Conventionally, vertical seismic resolution is expressed in terms of the wavelength of the dominant frequency (f_d) of the seismic signal. The generally accepted threshold for vertical resolution is a quarter of the dominant wavelength (Yilmaz, 1987). This treatment however, does not account for the frequency content of a Chirp wideband signal. In this chapter, emphasis is placed upon the temporal resolution of Chirp sources in terms of time and frequency components, rather than in terms of wavelengths and thickness (which inherently require a knowledge of interval velocities).

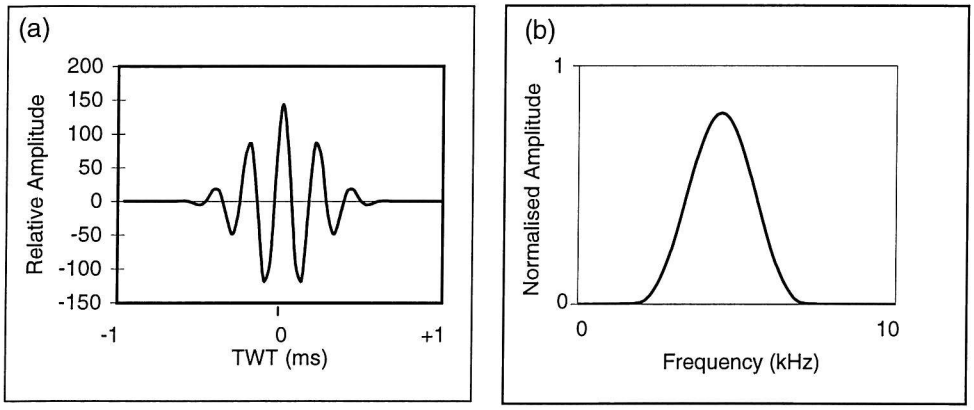

Figure 3.1: (a) The zero-phase Klauder wavelet - the autocorrelation of the 32ms, 2-8 kHz Chirp pulse; (b) The associated power spectrum.

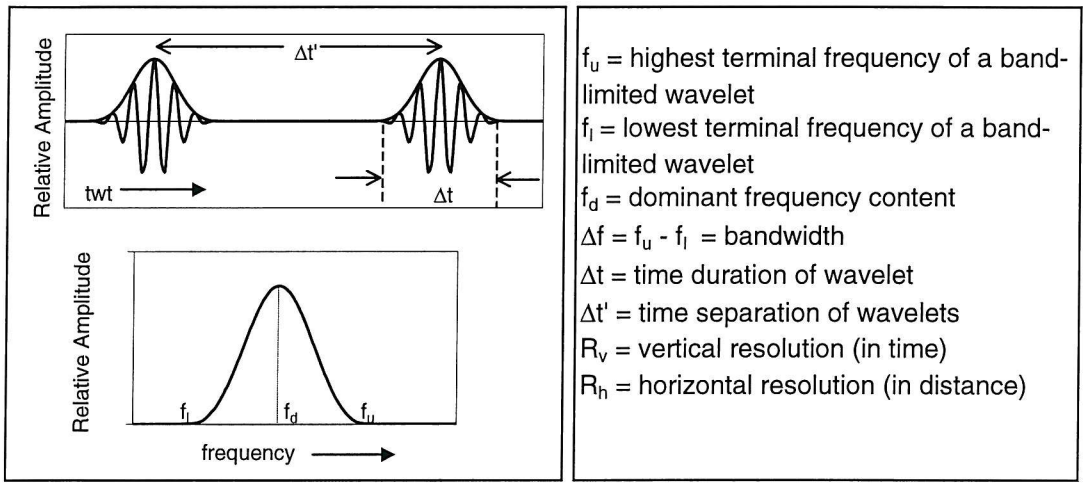

Figure 3.2: A graphical representation of notation used in the discussion on seismic resolution of Chirp sources.

3.2.2 *Temporal resolution and signal bandwidth*

The relationship between temporal resolution and signal bandwidth is defined by the *uncertainty principle* (Clarebout, 1976; Clay, 1977) as:

$$\Delta f \Delta t \geq 1, \qquad (3.1)$$

where Δf is the bandwidth and Δt the time duration of the wavelet. Intuitively, for two wavelets of duration Δt separated by $\Delta t'$, the wavelets are resolvable when $\Delta t \leq \Delta t'$, and are on the limit of resolution when $\Delta t = \Delta t'$ (Figure 3.2). The uncertainty principle therefore defines the minimum bandwidth required to identify two points separated by Δt. Equally, the relationship can be used to define the vertical resolution of a wideband seismic source of bandwidth Δf as:

$$R_V = \frac{1}{\Delta f}. \qquad (3.2)$$

Schock and LeBlanc (1990) and Parent and O' Brien (1993), without justification, propose that the vertical resolution of Chirp sources is controlled by the length of the Klauder wavelet, approximately equal to the inverse of the bandwidth. This proposal is in direct agreement with equation 3.2.

3.2.3 *Criteria for vertical resolution*

A unifying definition of vertical resolution is absent, as a precise definition is rather subjective. The complexity of the issue is outlined by Koefoed (1981) who proposed that vertical resolution is controlled by three aspects of the seismic wavelet - the width of the central lobe, side lobe ratio and side tail oscillations. Koefoed concluded that an improvement in any one of these aspects leads to a deterioration of one of the other aspects. The limits of vertical resolution are variably defined as:

(a) *Rayleigh's criterion*

The criterion established by Rayleigh (Jenkins and White, 1957; Kallweit and Wood, 1982) is to define the peak-to-trough separation as the limit of resolution (Figure 3.3 ii). In other words, two wavelets are resolved when their separation distance exceeds the peak-to-trough separation of an individual wavelet, *i.e.* when $\Delta t' > b/2$.

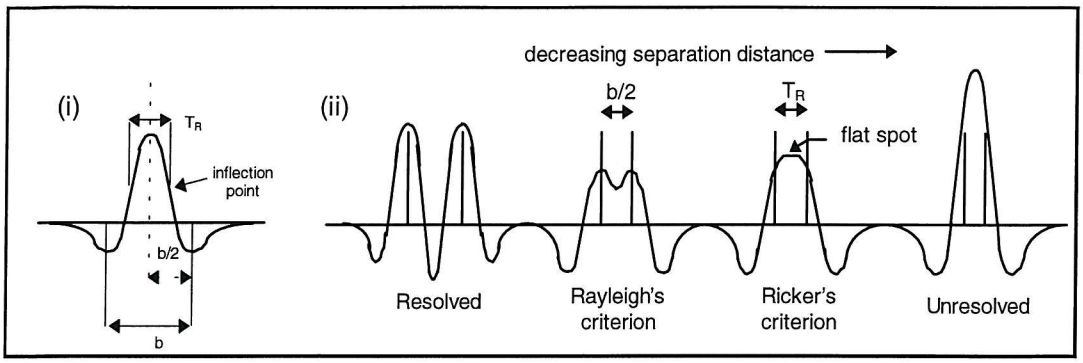

Figure 3.3: The limits of resolution as defined by Rayleigh and Ricker. (i) For a wavelet, b = wavelet breadth; b/2 = peak-to-trough time; T_R = separation between inflection points. (ii) Rayleigh's limit of resolution occurs when wavelets are separated by the peak-to-trough time interval, b/2; Ricker's limit occurs when wavelets are separated by a time interval equal to the separation of inflection points, T_R. (modified from Kallweit and Wood, 1982).

(b) *Ricker's criterion*

Ricker (1953) studied the composite waveform as a function of separation and observed the central maxima of two waveforms merge as separation decreases, finally merging into a single peak with no subsidiary maxima. Ricker chose the vertical resolution criterion to be that separation where the composite waveform has a "flat-spot" (zero-curvature) at the central maximum (Figure 3.3 ii). A point of zero curvature occurs when two spikes are separated by an interval (T_R) equal to the separation between the inflection points on the central maximum of the convolving wavelet (Figure 3.3 i).

(c) *Widess' criterion*

Both Rayleigh's and Ricker's criterion were defined using two spikes of equal amplitude and polarity. Widess (1973) described the results of convolving a zero-phase wavelet with two spikes of equal amplitude, but opposite polarity. Widess concluded that the "theoretical threshold of resolution" occurs when wavelet separation is one-eighth of a wavelength of the dominant frequency of the propagating wave.

(d) *Kallweit and Wood's criterion*

The main objective of Kallweit and Wood's (1982) work was to develop concepts for the resolution of zero-phase wavelets unifying the viewpoints outlined above, thereby removing polarity considerations from resolvability. Kallweit and Wood concluded that the temporal resolution of a broadband wavelet with a white spectrum is controlled by the highest terminal frequency (f_u), and the resolution limit approximates to $1/(1.5f_u)$ provided the band ratio of the wavelet exceeds 2 octaves. These authors further concluded that the practical limit of resolution occurs at a quarter wavelength condition and approximates to $1/(1.4f_u)$.

Table 3.1 summarises the criteria outlined above for the vertical resolution of a seismic source.

Criterion	**R_v**
Rayleigh (Jenkins and White, 1957)	$\frac{b}{2}$
Ricker (1953)	T_R
Widess (1973)	$\frac{\lambda_d}{8} = \frac{v_p}{8f_d}$
Uncertainty principle (Clarebout, 1976; Clay, 1977)	$\frac{1}{\Delta f}$
Kallweit & Wood (1982)	$\frac{1}{1.4f_u}$
Yilmaz (1987)	$\frac{\lambda_d}{4} = \frac{v_p}{4f_d}$
Schock & LeBlanc (1990) Parent & O' Brien (1993)	length of compressed Chirp pulse (*i.e.* Klauder wavelet)

Table 3.1: Table summarising the criteria for vertical seismic resolution as outlined in the text.

3.2.4 *The effective vertical resolution of Chirp sources*

Figure 3.4 shows the results of convolving the zero phase Klauder wavelet with two spikes of equal amplitude and polarity, with separation distance increasing at a constant interval of 40μs (corresponding to the sample rate of the Chirp source waveform). The modelling rationale follows that of Rayleigh and Ricker in examining the resolution of two spikes of equal amplitude and polarity. The synthetic seismograms display both the seismic response of the composite wavelets and the instantaneous amplitude of the waveform {R(t)}.[1] The calculation of R(t) effectively applies an envelope function to the data, smoothing the time series. Chirp sub-bottom data is conventionally displayed in this manner.

The interference composites in Figure 3.4 destructively interfere until a separation distance of 0.28 ms (model g) is realised. At this separation, the envelope function of the composite waveform fits Ricker's criterion for vertical resolution, with a point of zero curvature in the centre of the composite waveform. Model h, with an increment of 40μs on model g, fits Rayleigh's criterion, where the wavelets are clearly resolved into two maxima of equal amplitude corresponding to the spatial positioning of the spikes in the impulse response (separation of 0.32 ms).

[1] See Section 4.3.1 of Chapter 4 for further discussion.

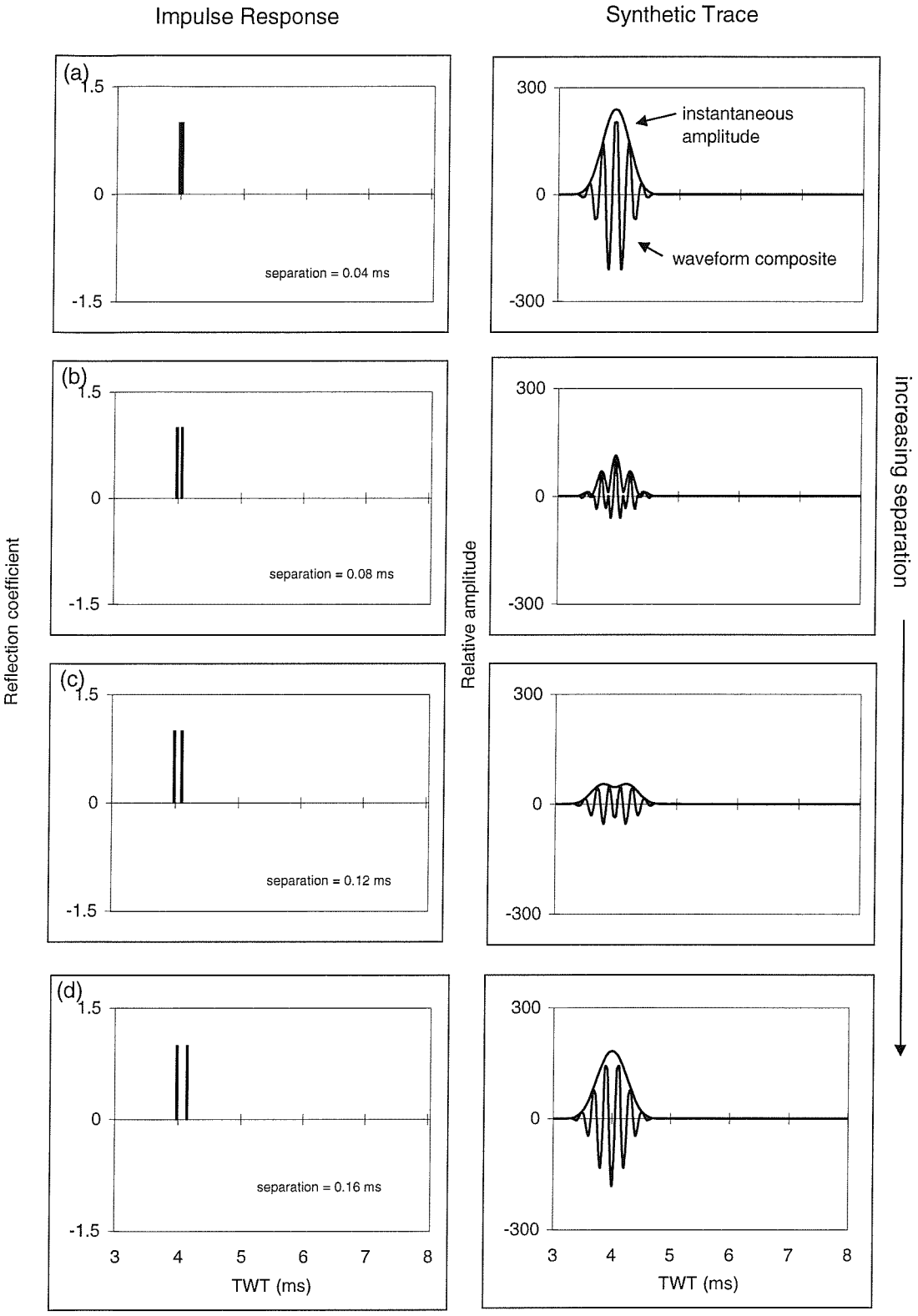

Figure 3.4: (a-h) The seismic response of the Klauder wavelet convolved with two spikes of increasing separation - impulse responses are shown on the left and synthetic traces on the right (continued overleaf).

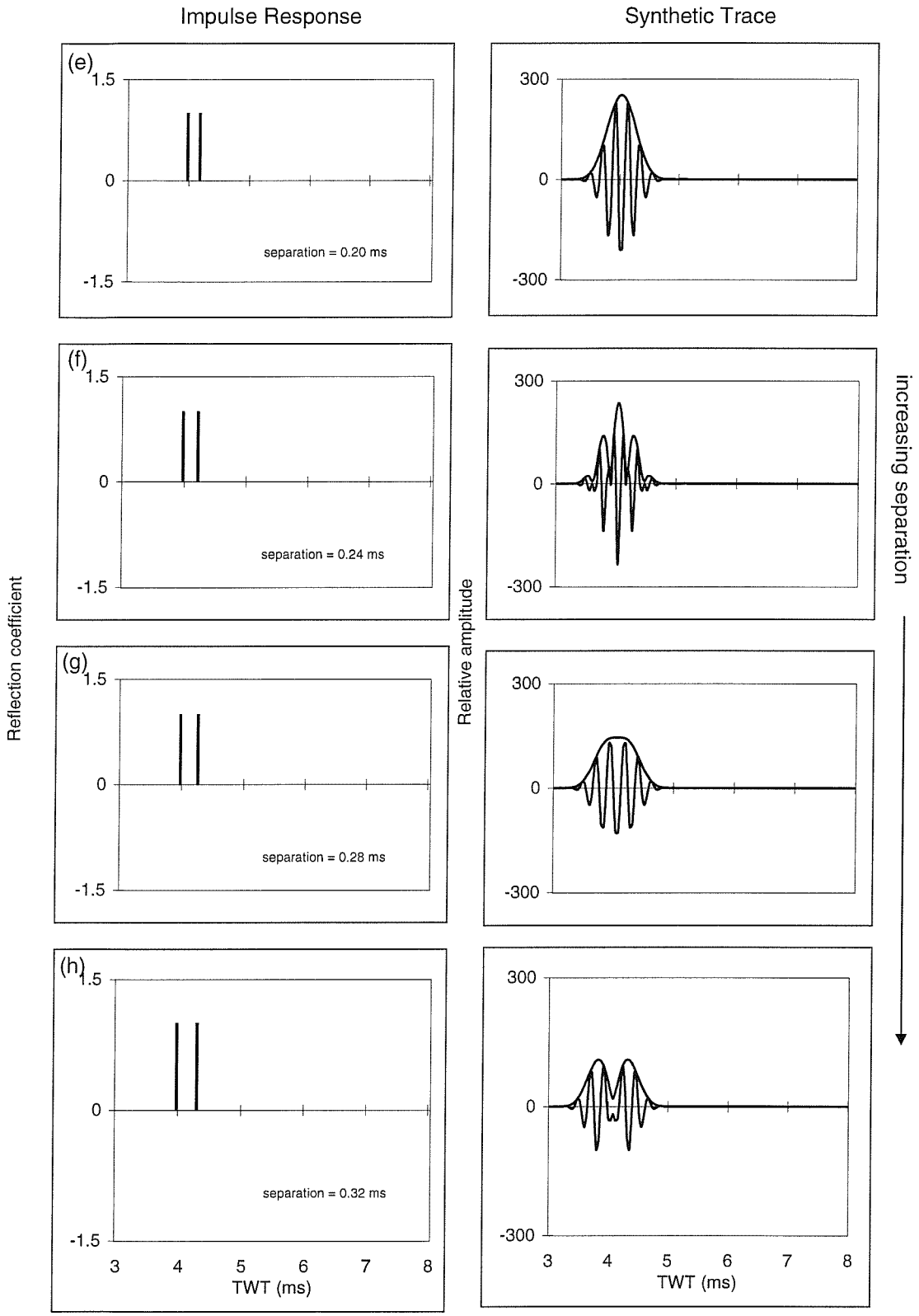
Impulse Response
Synthetic Trace
(e)
1.5
0
-1.5
separation = 0.20 ms
300
0
-300
(f)
separation = 0.24 ms
(g)
separation = 0.28 ms
(h)
separation = 0.32 ms
3
4
5
6
7
8
TWT (ms)
Reflection coefficient
Relative amplitude
increasing separation

Closer examination of the wavelet complexes (ignoring the envelope function) shows that two separate waveforms can be distinguished in models c to e. In model c, the envelope function also successfully discriminates two distinct reflections, corresponding to the positions of the spikes in the impulse response. However, in model f, the composite waveforms destructively interfere once again, and three distinct reflections appear instead of two. Therefore, the separation distance in model g is the first separation distance truly representing the effective resolution of the 2-8 kHz source. The wavelets cease interfering with one another once this critical separation distance is passed. This implies that close examination of correlated Chirp data (prior to the calculation of reflection strength) may uncover resolution aspects unrecognisable in data subsequent to the application of the envelope function.

Table 3.2 lists the comparative time- and spatial- vertical resolutions for the criteria outlined above.

Criterion	R_v (ms)	R_v (m)
Rayleigh	Model (h): $\Delta t' = 0.32$	0.240
Ricker	Model (g): $\Delta t' = 0.28$	0.210
Widess	$\frac{v_p}{8f_d}$ = *N/A.*	0.038
Uncertainty principle	$\Delta t = \frac{1}{\Delta f} = 0.16^{\bullet}$	0.125
Kallweit & Wood	$\frac{1}{1.4f_u} = 0.09$	0.068
Yilmaz	$\frac{v_p}{4f_d}$ = *N/A.*	0.075
Schock & LeBlanc Parent & O' Brien	Klauder wavelet length $(\Delta t) = 0.16^{\bullet}$	0.125

Table 3.2: Summary of the vertical resolution in time (centre column) and space (right column) calculated from models (Figure 3.4) and theory using a 2-8 kHz Chirp source (with a dominant frequency of 5 kHz) travelling through sediments of $V_p = 1500\ ms^{-1}$. All calculations ignore attenuation effects, assuming the bandwidth of the signal is preserved.

Deconvolution is a process that attempts to increase vertical resolution by compressing the seismic wavelet in time. Ideally, deconvolution compresses the seismic wavelet to a single spike (or Dirac-delta function), thereby broadening the power spectrum. The synthetics presented in Figure 3.4 are not deconvolved. Deconvolution of synthetics is pointless, as it is possible to compress the Klauder wavelet to the ideal spike by designing a decon-operator around the source wavelet. Therefore, the modelling exercise represents the worst case scenario, or lowest limit of resolution.

If we accept that the vertical resolution of the wideband Chirp source must be dependent upon the entire frequency content of the source-signature and not only upon the dominant frequency component, the uncertainty principle is the criterion which governs the resolution of Chirp sources. If we further accept that Rayleigh's criterion represents the limits of resolution of

the instantaneous amplitude of the wavelet, then model h (with a separation distance of 0.32 ms) defines the lowest limit of vertical resolution. For Chirp sources, this approximates to twice the value predicted by the uncertainty principle ($0.16^{\bullet}$ ms, Table 3.2), or:

$$\Delta f \Delta t \cong 2 . \qquad (3.3)$$

So, the *lower limit* (worst case scenario) to the vertical resolution of Chirp sources may be written as:

$$R_v \leq \frac{2}{\Delta f} . \qquad (3.4)$$

The *upper limit* (best case scenario) of vertical resolution is dependent upon the signal-to-noise ratio of the data, attenuation effects and the success of data deconvolution. Realistically, the upper limit of resolution of the wideband Chirp source must be dependent upon the entire bandwidth of the waveform (Equation 3.3), and not merely the dominant frequency of the source. These proposals suggest the temporal resolution of the source signal is constrained by the relationship:

$$\frac{2}{\Delta f} \geq R_v \geq \frac{1}{\Delta f} . \qquad (3.5)$$

It must be stressed that this relationship is a generalisation, and is entirely dependent upon the definition of resolution (in this case Rayleigh's criterion is used). For the 2-8 kHz Chirp source, the limits of vertical resolution are: $0.25m \geq R_v \geq 0.125m$

3.3 *Horizontal resolution (R_h) of Chirp sources*

Horizontal resolution refers to how closely two reflecting points can be situated laterally, yet be imaged as two separate points rather than one (Yilmaz, 1987). The generally accepted control on horizontal resolution is the Fresnel zone, a circular area on a reflector whose diameter is dependent upon the depth to the reflector, the compressional wave velocity of material above the reflector and the dominant frequency of the incident seismic wave. The radius of the Fresnel zone (R_{fz}) is given by the relationship:

$$R_{fz} = \frac{V_p}{2} \sqrt{\frac{twt}{f_d}} , \qquad (3.6)$$

where V_p is the average velocity, twt is the two-way time of the reflector and f_d is the dominant frequency in the recorded data (Yilmaz, 1987). When two reflecting points fall within the radius described by the Fresnel zone, the points are unresolved. In general, the radius of the Fresnel Zone increases with depth of penetration.

The beam angle of a Chirp source, and therefore the footprint of the system, is dependant upon the transducer array and the bandwidth of the source. Beamwidth figures at certain frequencies for a 4-transducer Chirp array are listed in Table 3.3.

Frequency (kHz)	Beamwidth (°)
3.5	55
5.0	45
7.0	35

Table 3.3: Beamwidth figures for the 4-transducer Chirp array (courtesy of GeoAcoustics Ltd.).

Simple trigonometry defines the radius of the Chirp footprint (R_{cf}, the circular area of the reflector insonified by the system) as:

$$R_{cf} = \frac{V_p twt}{2} \tan\frac{\theta_d}{2}, \qquad (3.7)$$

where θ_d is the beam angle of the system associated with the dominant frequency component of the Chirp source.

The final factor effecting horizontal resolution of seismic data is the trace interval. In the case of marine seismic surveying, this factor is dependent upon survey speed (ms^{-1}) and the pulse rate (s^{-1}) of the survey system by:

$$\text{Trace Interval} = \text{survey speed} / \text{pulse rate}. \qquad (3.8)$$

In practice, the radius of the Fresnel zone will never increase to a size as large as that predicted by the Chirp footprint. Therefore the upper and lower limits of the horizontal resolution of Chirp sources may be defined as:

$$\frac{V_p twt}{2} \tan\frac{\theta_d}{2} \geq R_h \geq \frac{V_p}{2}\sqrt{\frac{twt}{f_d}}. \qquad (3.9)$$

For a 2-8 kHz source, propagating in a medium of $V_p = 1500\ ms^{-1}$, the limits of horizontal resolution at a two-way travel-time of 10 ms (7.5 m) are: $3.11m \geq R_h \geq 1.06m$, reinforcing the requirement of towing the Chirp towfish as close to the seabed as possible in order to maximise the horizontal resolution. As outlined above, the other controlling factor on horizontal resolution is the trace interval. Typically, Chirp surveying is conducted at a rate of 4 knots, or 2 ms^{-1}, with a pulse rate of 4 s^{-1}, equating to a trace interval of 0.5 m. The trace interval in this case is of the same order as the Fresnel zone and the chirp footprint. It is therefore a significant factor in the effective horizontal resolution, and should be considered in data interpretation.

3.4 Attenuation effects

Attenuation by marine sediments is arguably the most important factor determining the effective resolution of the Chirp source. Figure 3.5a is a plot of compressional wave attenuation in marine sediments against mean grain diameter (ϕ) compiled by LeBlanc *et al.*, 1992b. These data display an increase in attenuation with increased ϕ with a maximum observed at fine sand. With further increase in ϕ, attenuation decreases in the silt region and drops gradually.

The zero-phase Chirp Klauder wavelet is designed to have a Gaussian shaped power spectrum (Figure 3.1). This zero phase (or linear phase) characteristic results in the pulse being symmetrical about its peak value. Non-linear phase, caused by phase dispersion of the pulse as it propagates through an attenuating medium, modifies the shape of the pulse so the time domain representation of the wavelet is no longer symmetrical (LeBlanc *et al.*, 1992b). The Chirp wavelet is effectively stretched in time due to attenuation effects, broadening the time duration of the pulse (Figure 3.5b). As the Chirp source signature is known exactly, effective deterministic deconvolution will, to a varying degree, offset the effects of pulse-broadening by compressing the wavelet in time. Source-signature deconvolution is discussed in detail in Chapter 4, Section 4.3.1.

Attenuation effects are manifested in the frequency content of the reflected Chirp data by a downshifting of the dominant frequency, f_d, in the power spectrum (Chapter 4, Section 4.3.1; LeBlanc *et al.*, 1992b; Schock *et al.*, 1989; Panda *et al.*, 1994). Figure 3.5c displays the shift in f_d for a 2-10 kHz Chirp pulse propagating through sand silt and clay. This *shift* in f_d is a measurable quantity and has been used to directly convert frequency shift per metre to a measurement of sediment attenuation (LeBlanc *et al.*, 1992b; Panda *et al.*, 1994). The shift in f_d to a lower frequency causes an unavoidable increase in the size of the Fresnel zone, and so lowers the horizontal resolution of the system.

Figure 3.6 illustrates the effects of sediment attenuation on the frequency content of Chirp sources. The profile, shot through a sequence of laminated marine muds and clays, was acquired utilising a 2-8 kHz Chirp source of f_d = 5 kHz. The dominant frequency component in the power spectra decreases with depth of penetration, from 5 kHz at the seafloor (5 ms) to 2.9 kHz in the sediment pile above the bedrock reflector (22 ms). This corresponds to an overall downshifting of 2.1 kHz in 17 ms (or 12.75 m penetration assuming $V_p = 1500\ ms^{-1}$). Figure 3.5c (after LeBlanc *et al.*, 1992b) predicts a shift of approximately 200 Hz in the dominant frequency component for a 2-10 kHz Chirp pulse propagating in marine clays at a depth of 13 m. The attenuation effects in the Strangford Lough data are an order of magnitude higher than those predicted by LeBlanc *et al.*, 1992b for fine-grained marine sediments. These high attenuation

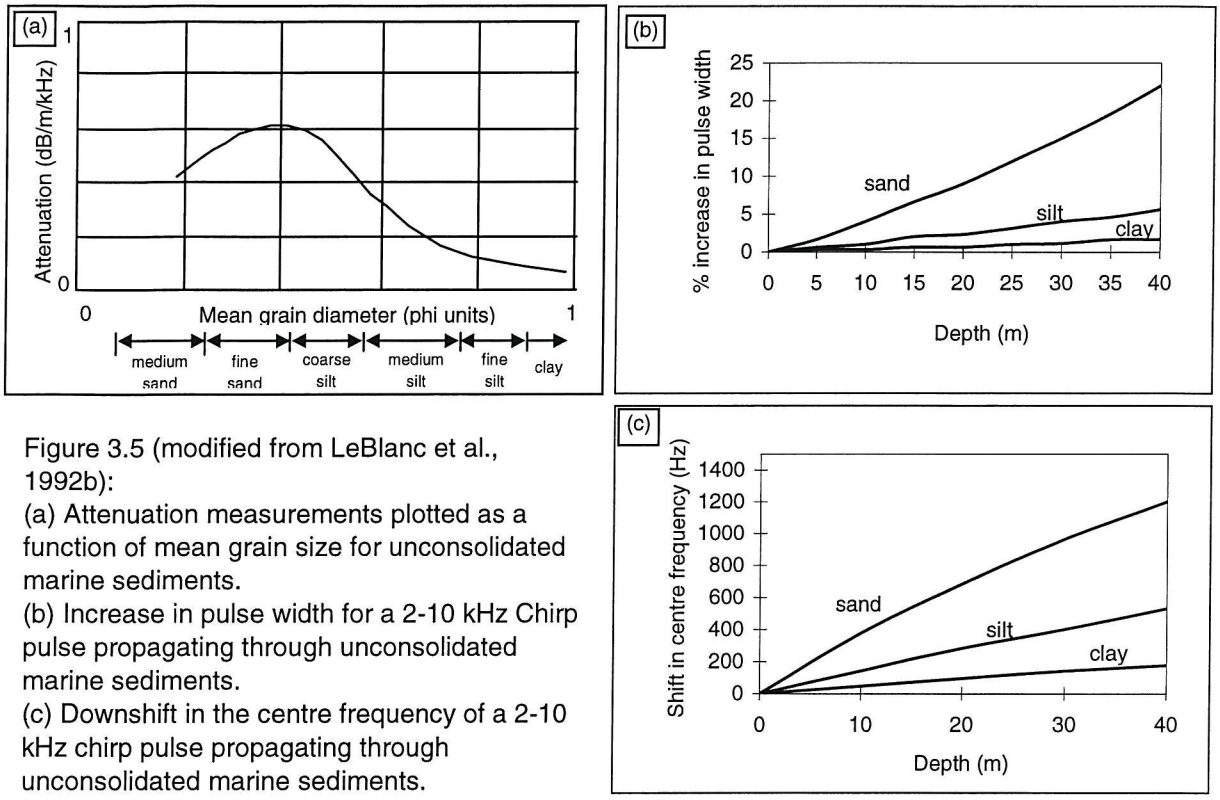

Figure 3.5 (modified from LeBlanc et al., 1992b):
(a) Attenuation measurements plotted as a function of mean grain size for unconsolidated marine sediments.
(b) Increase in pulse width for a 2-10 kHz Chirp pulse propagating through unconsolidated marine sediments.
(c) Downshift in the centre frequency of a 2-10 kHz chirp pulse propagating through unconsolidated marine sediments.

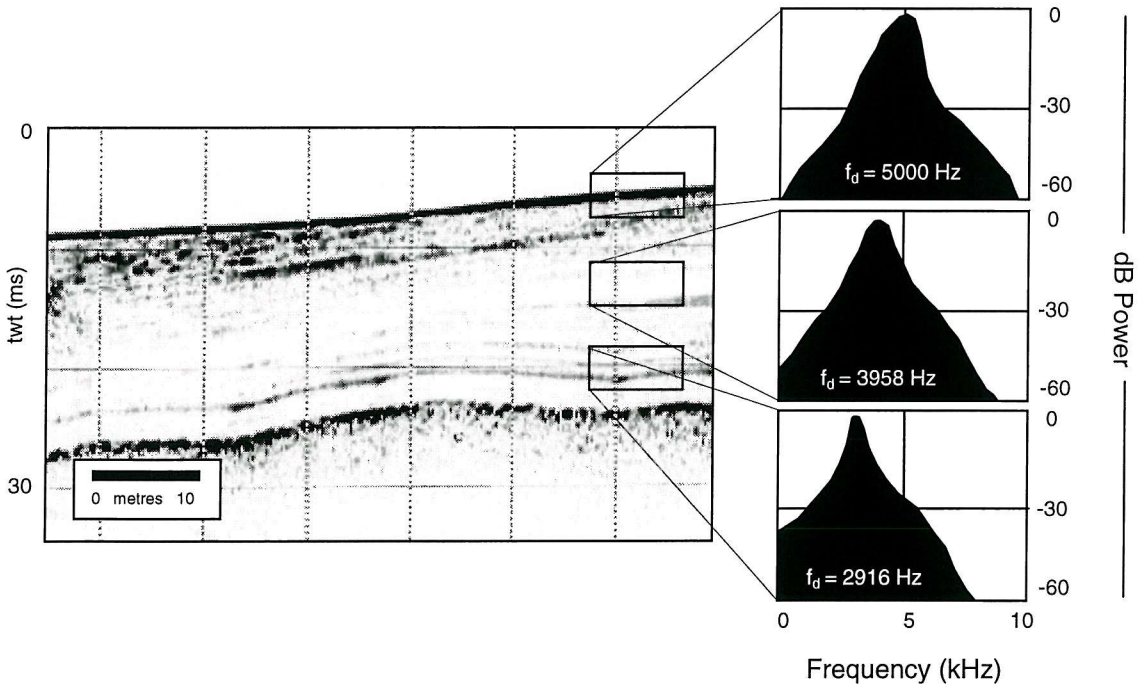

Figure 3.6: Diagram illustrating the effects of sediment attenuation on the frequency content of Chirp sources. The profile, shot through a sequence of laminated marine muds and clays in Strangford Lough (Northern Ireland), was acquired utilising a 2-8 kHz Chirp source of f_d = 5 kHz. The power spectra average the frequency content of 40 traces over 2 ms time windows of increasing depth: 4-6ms (seafloor), 13-15 ms and 19-21 ms. Frequency analysis is conducted on correlated data, sampled at an interval of 40 μs.

effects *may* be attributable to the destructive interference of the high frequency component (caused by interference composites from sediment laminae), leading to an overall decrease in bandwidth and substantial decrease in the dominant frequency component. This attribute of Chirp data is further discussed in Chapter 6.

Attenuation effects are very important when selecting the operating frequency band of the Chirp source for optimum resolution and penetration. In sand-dominated environments, where attenuation effects are highest, a source signature with a relatively small bandwidth and low f_d is desirable. In contrast, clay- and silt-rich environments will attenuate the Chirp source to a much lesser extent, and so relatively wideband sources with a higher f_d is desirable for optimum penetration and resolution. However, as outlined in the above paragraph, the presence or absence of sediment lamination is also an important factor in choosing the source signature for site investigation.

3.5 *Conclusions*

- The vertical resolution of Chirp sources are dependent upon the bandwidth (Δf) of the reflection data by:

$$\frac{2}{\Delta f} \geq R_v \geq \frac{1}{\Delta f}$$

- The horizontal resolution of Chirp sources are constrained by:

$$\frac{V_p twt}{2} \tan\frac{\theta_d}{2} \geq R_h \geq \frac{V_p}{2}\sqrt{\frac{twt}{f_d}},$$

  where V_p is the compressional wave velocity, twt the two-way travel time and θ_d the beam angle associated with the dominant frequency component, f_d.

- Sediment attenuation causes a lithology-dependent broadening of the Chirp wavelet, a downshifting of the dominant frequency component and an associated decrease in bandwidth. These factors adversely affect both the vertical and horizontal resolution of the Chirp source.

— Chapter 4 —

Optimal processing of marine high-resolution seismic reflection (Chirp) data[1]

4.1 *Introduction*

Chirp sub-bottom profilers are high-resolution FM sources offering vertical resolution on the decimetre scale in the top c. 30m of unconsolidated sediments. Typical applications of Chirp systems are in areas of marine bottom-sediment classification, marine foundation, pipeline laying, platform and well-site evaluation and archaeological and environmental impact surveys.

The principal feature that distinguishes Chirp systems from short-pulse, single-frequency profilers (e.g. boomers and pingers) is the nature of the Chirp source-signature. The sonar system transmits computer-generated, swept-frequency pulses (Figure 4.1a) which are amplitude- and phase-compensated (Schock *et al.*, 1989; LeBlanc *et al.*, 1992a; Panda *et al.*, 1994). This precise waveform control helps suppress source-ringing (a common problem affecting the vertical resolution of short-pulse profilers). The Chirp waveform is weighted in the frequency domain to possess a Gaussian spectrum (Figure 4.1b) and the autocorrelation of the Chirp pulse is the zero-phase Klauder wavelet shown in Figure 4.1c.

Chirp technology therefore presents the uncommon case amongst high resolution sub-bottom systems of a determined, repeatable source-signature, and hence a greater probability of recognising signal in the presence of noise. The following discussion summarises the optimal processing of uncorrelated Chirp data and highlights the inherent advantages to the seismic processor in a resolved source-signature. Emphasis is placed upon the processing of these data to aid interpretability of high resolution profiles, rather than quantitative sediment analysis. Results indicate that the application of predictive filter techniques to Chirp sub-bottom data is successful in increasing both the SNR and the lateral continuity of the data.

4.2 *Methodology*

Uncorrelated single-fold data presented in this paper were acquired in the East Solent, U.K. in May 1995 utilising a Chirp towed transducer system comprising 4 transducers coupled to a plate and a single-section hydrophone. The hydrophone (bandwidth of 0.5 to 15 kHz) comprises an 8-section mini-streamer and in-built power amplifier. Throughout the survey, a 32ms Chirp pulse (Figure 4.1 a) of bandwidth 6 kHz (sweep of 2-8 kHz) with a repeat period of 250 ms and a sample interval of 40μs was employed. The dominant frequency (or carrier frequency), f_d, of this pulse is 4.6 kHz (Figure 4.1b). The Chirp section used in this paper represents a continuous, single channel profile of 200 traces, with an average trace-interval of

[1] Quinn, R., Bull, J.M. and Dix, J.K., *Marine Geophysical Researches,* in review.

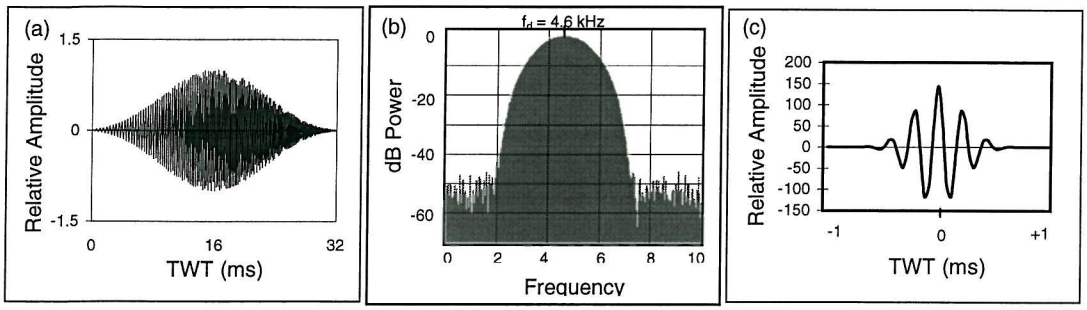

Figure 4.1: (a) The 32 ms frequency-modulated pulse linearly sweeping from 2-8 kHz. (b) Power spectrum of the Chirp pulse. (c) Zero-phase Klauder wavelet - the autocorrelation of the Chirp pulse.

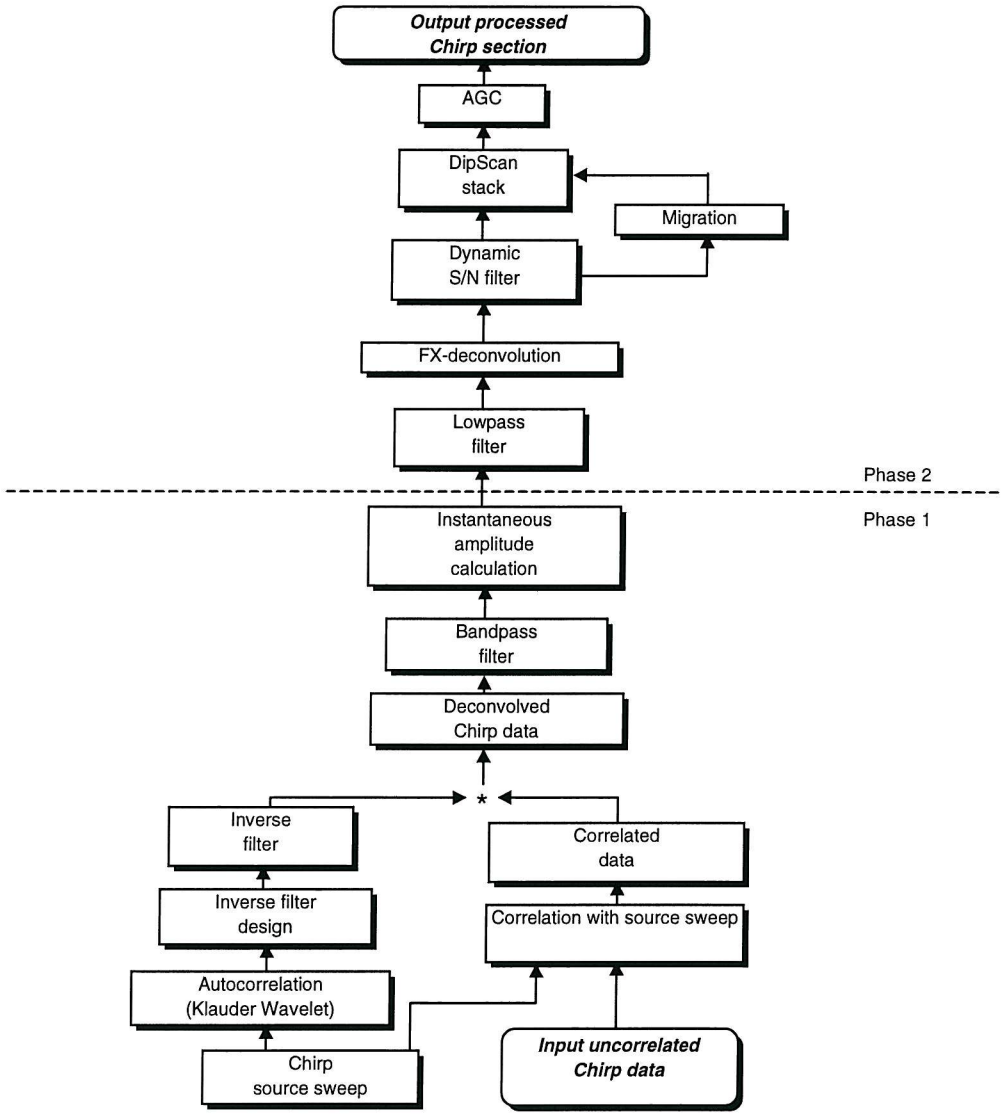

Figure 4.2: Flow chart outlining the processing sequence applied to uncorrelated Chirp data. Phase 1 = correlation and deconvolution; Phase 2 = filtering.

0.6m acquired in an average water depth of 7.5 m. All data processing is conducted in the ProMAX^{TM} 6.0 software package (Advance Geophysical Corporation) mounted on a SUN Ultra workstation.

Processing algorithm and parameter suitability were assessed by their effects on both single- and multi-trace Chirp seismograms. Processing of the uncorrelated data is divisible into two phases (Figure 4.2): (1) correlation and deconvolution; (2) filtering.

Two methods are employed to demonstrate the effects of the processing algorithms on the uncorrelated data. The first method is the presentation of the full profile at significant stages within the processing sequence. The second mode of display is single-trace seismograms (together with associated power spectra) in which the effects of each step in the processing sequence can be examined in detail (Figure 4.3). Trace 3100 is chosen as the display trace as it possesses a relatively low SNR and the effects of each processing stage can be readily appreciated.

4.3 *Chirp data processing*

4.3.1 *Phase 1 - correlation and deconvolution*

A zero-phase correlation of the uncorrelated data was performed utilising the source sweep in Figure 4.1a. The resulting correlated data are effectively the superposition of the Klauder wavelet (Figure 4.1c) on the earth's impulse response, plus some noise component. The results of correlation with the source sweep are illustrated in the profile of Figure 4.4 and the single-trace seismogram of Figure 4.5a. In the complete profile, the major reflection events (seabed at 10 ms and bedrock profile between 20 and 25 ms) are distinguishable, but sharp detail in the sediment pile is lacking due to the ringiness of the Klauder wavelet. However, the correlation process has increased the overall SNR of the data, aiding interpretability (compare the power spectra of Figures 4.3 and 4.5a). A noticeable characteristic of the correlated data is the downshifting of the carrier frequency from 4.6 kHz in the source sweep to 4.2 kHz in the reflection data. A similar effect was recognised by LeBlanc *et al.* (1992b) and Panda *et al.* (1994) and attributed to sediment attenuation causing the centre frequency of the Chirp pulse spectrum to shift to a lower frequency.

Subsequent to correlation, a source-signature deconvolution (Figure 4.2, Phase 1) is performed to reduce the ringiness of the correlated data. The solution to the deconvolution problem is said to be deterministic (Yilmaz, 1987) as the Chirp source-signature is known exactly. An inverse filter (the inverse of the Klauder wavelet) is calculated and this operator is convolved with the correlated data. A comparison of the correlated and deconvolved seismograms in Figures 4.5a and 4.5b demonstrates that individual reflectors are enhanced by this process, and previously indistinguishable events are revealed. However, this process fails to convert the seismogram into a series of pure spikes representing the desired impulse response due to the presence of noise.

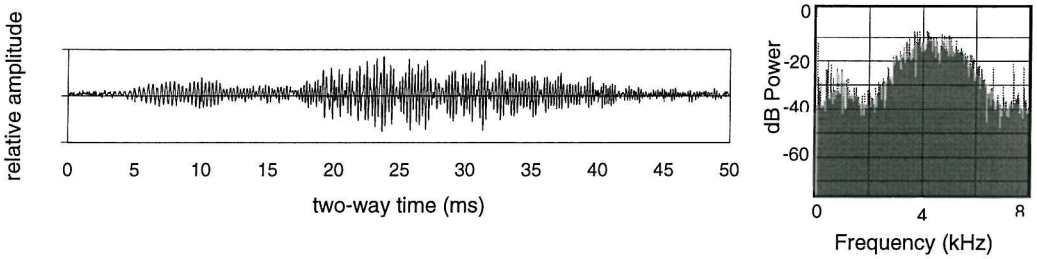

Figure 4.3: Single uncorrelated Chirp seismogram (Trace 3100) with associated power spectrum.

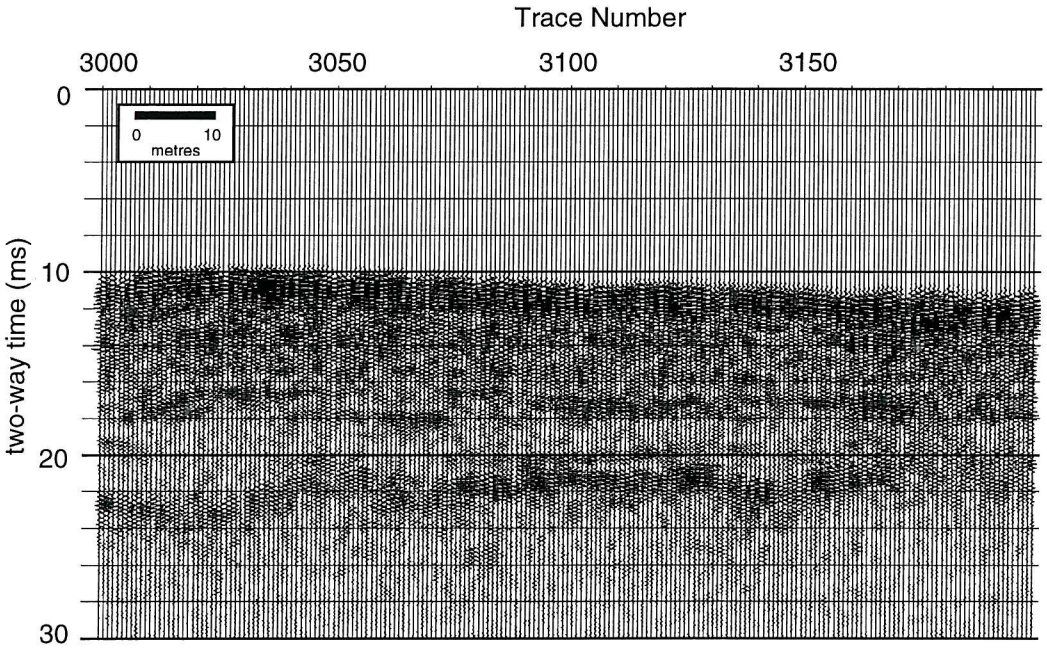

Figure 4.4: Correlated Chirp profile of 250 traces with an average trace interval of 0.6m. The seabed and bedrock interfaces are imaged at approximately 10 ms and 23 ms two-way travel time respectively.

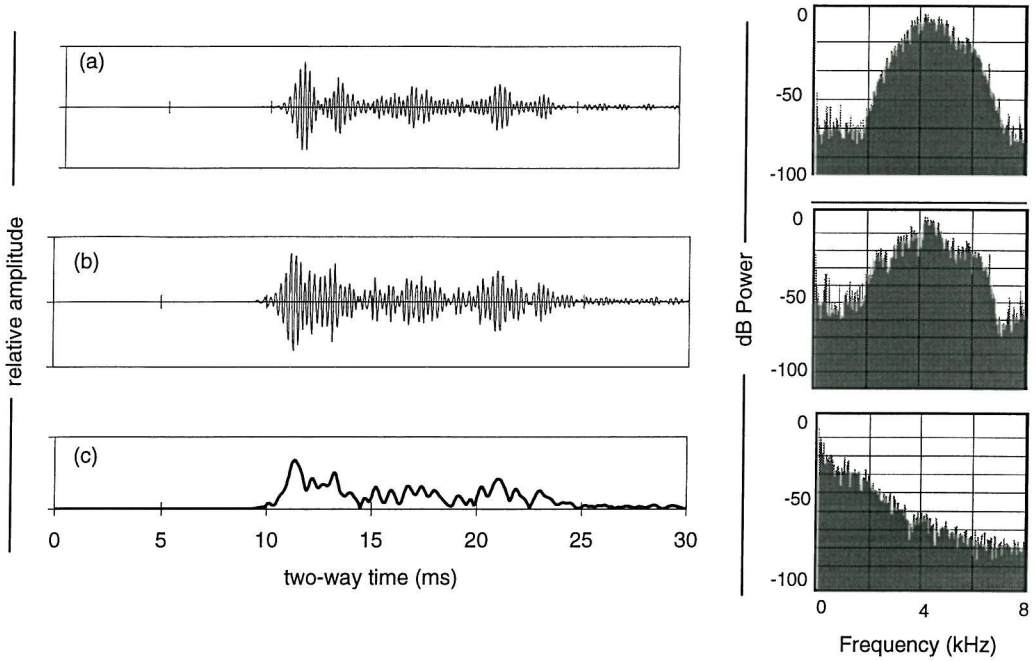

Figure 4.5: Diagram illustrating the three initial stages in the processing history of the Chirp profile. Single trace seismograms (Trace 3100) are displayed with their associated power spectra. (a) Zero-phase correlation (b) Source-signature deconvolution of 4.5a (c) Instantaneous amplitude calculation of 4.5b.

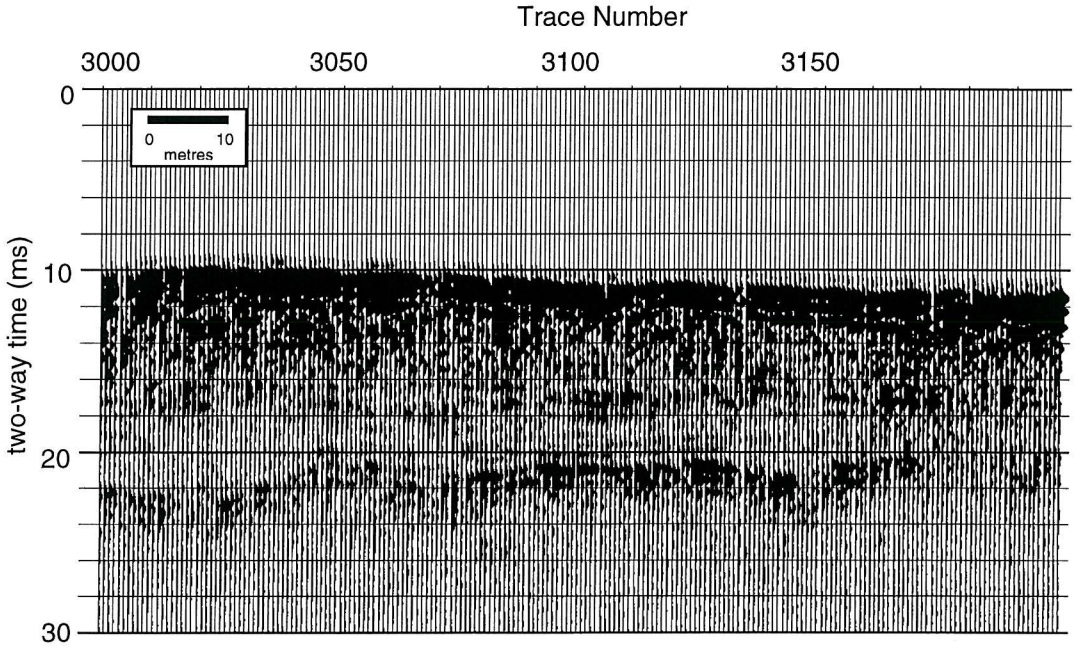

Figure 4.6: Correlated Chirp profile subsequent to source-signature deconvolution and instantaneous amplitude calculation.

In order to increase the interpretability of the deconvolved Chirp data, the instantaneous amplitude (a measure of the reflectivity strength), R(t), of the signal is calculated. R(t) "is proportional to the square root of the total energy of the seismic signal at an instant in time" (Yilmaz, 1987):

$$R(t) = \sqrt{x^2(t) + y^2(t)} \qquad (4.1)$$

where x(t) is the signal and y(t) is its quadrature (Taner *et al.*, 1979; Yilmaz, 1987). In the calculation of the instantaneous amplitude for Chirp data, only the signal component [x(t)] is used. This irreversible function effectively applies an envelope function to the deconvolved data, smoothing the time series and changing the ringy signal (Figure 4.5b) into a distinct, low-frequency function (Figure 4.5c). The dominant frequency component is down-shifted from 2-8 kHz to 0-4 kHz at the -70 dB points. A downside to this application is a complete loss of polarity information as the data becomes fully rectified. Figure 4.6 is the deconvolved Chirp profile subsequent to the instantaneous amplitude calculation. The stratigraphy is now relatively well-defined. The seabed is characterised by a triple reflector (unrecognisable in the correlated seismogram) and the bedrock reflector is composed of two closely spaced, sub-parallel reflectors.

4.3.2 *Phase 2 - filtering*

The principal aims of the second phase in the processing sequence are to increase the overall SNR by the application of predictive filters and to enhance the lateral coherency of the data. The output from the instantaneous amplitude calculation is initially bandpass filtered to remove the high-frequency noise component (Figure 4.7a).

Subsequently, the FX-deconvolution algorithm Fourier transforms each input trace, applies a Wiener prediction filter (in distance) for each frequency in the 20-2200 Hz range and then inverse transforms the data back to the time domain (Figure 4.7b). When the data is transformed from the time domain to the frequency domain, each sample in the transformed data possesses both real and imaginary components. Events with similar dips appear as a sinusoidally complex signal along the given frequency slice and can de described in the form $(\cos \omega t + i \sin \omega t)$, while the time section is divided into small windows to better approximate the assumption of constant linear dip. The prediction filter is used to predict the signal one trace ahead across the frequency slice, and any difference between the predicted waveform and the actual one is classified as noise and filtered out of the section (ProMAX 6.0 User Manual). In practice the Wiener filter is run in one direction and subsequently run in the opposite direction and the resulting predictions are averaged to reduce errors (ProMAX 6.0 User Manual).

As a final stage in the filtering process, the FX-deconvolved data is passed through a dynamic signal-to-noise (SN) filter (Figure 4.7c). This process eliminates the requirement of a time-variant bandpass filter design (and application) which is difficult to design with the relatively small data window of the Chirp data (typically 10-40 ms for the 32ms Chirp pulse). Additionally, this process enhances the lateral coherency of data by weighting each frequency derived function from the local SNR. The theory used to approximate the weighting function is similar to

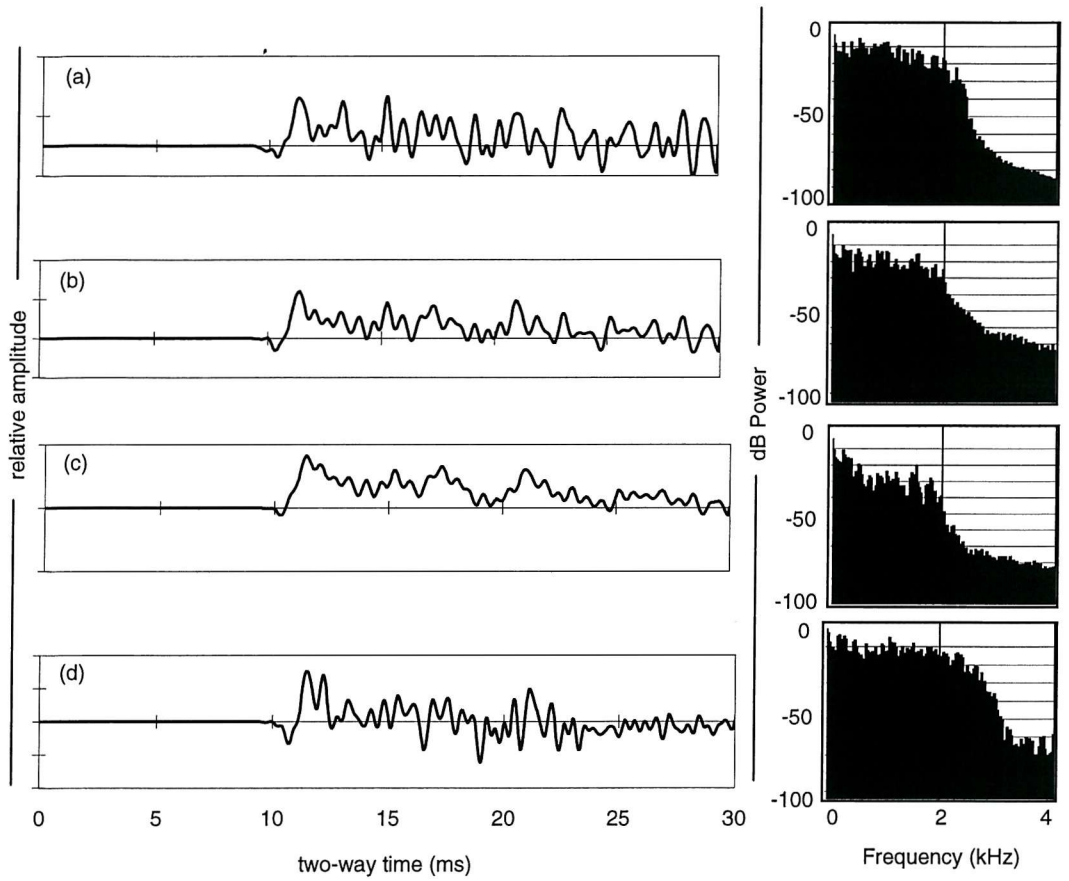

Figure 4.7: Diagram illustrating the final 4 stages in the processing history of the Chirp profile. Single-trace seismograms (Trace 3100) are displayed with their associated power spectra. (a) Bandpass filtered 4.5c (b) FX-deconvolution of 4.7a (c) Dynamic SN filter of 4.7b (d) Dip-scan stack of 4.7c.

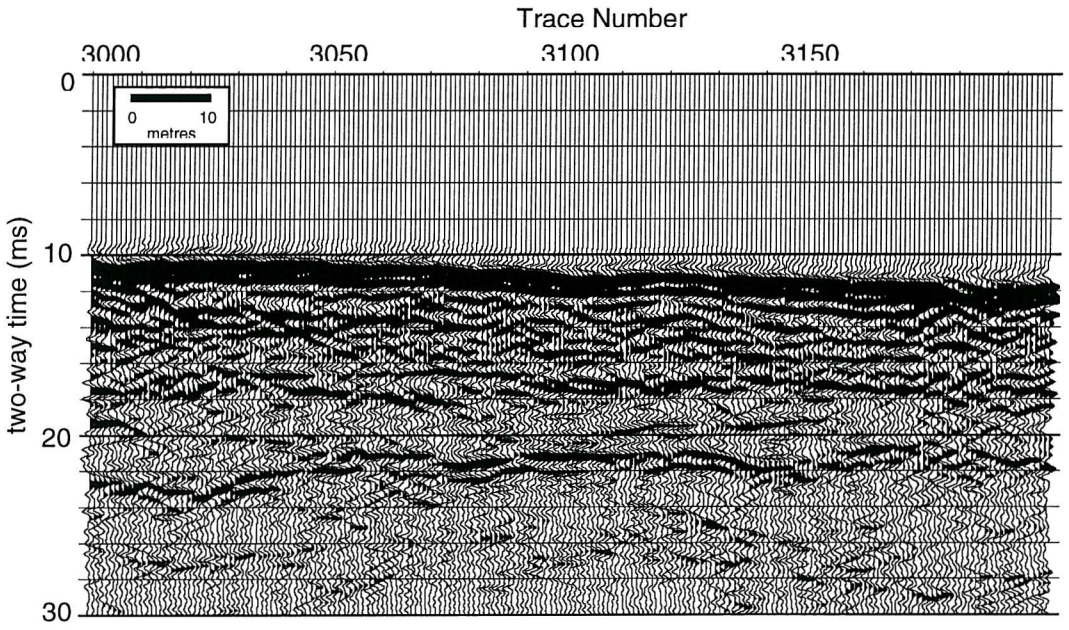

Figure 4.8: Final processed Chirp profile.

that for FX-deconvolution. A window over which the dip is fairly constant is chosen and each horizontal time slice is converted to a frequency slice. The operator moves laterally from trace to trace at a constant frequency, and treats each sample as the sum of a random noise component and a signal component which changes only by a constant phase shift, directly related to the dominant dip within the window (ProMAX 6.0 User Manual). Considering each frequency slice separately, the signal power plus noise power is estimated by summing the products of each sample and its complex conjugate. Each product contains a signal-squared plus noise-squared amplitude, plus cross products of signal and noise which cancel out if the signal does not correlate with the noise. The frequency domain weighting filter is given by:

$$\text{weight}(f) = \frac{S(f)^2}{S(f)^2 + N(f)^2}\ , \qquad (4.2)$$

where S(f) is the signal component and N(f) the noise component of the data (ProMAX 6.0 User Manual). For high SNR data, the weighting filter yields a scale factor of nearly 1, and conversely for data of low SNR, the weight approaches zero.

The final processing step is the application of the dip scan stack algorithm to enhance coherent seismic events by a weighting process (ProMAX User Manual 6.0). This algorithm transforms the input time-domain profile into a user defined range (in this case ± 0.18 ms per trace) of dip stacked traces. Sample by sample, each trace is then weighted by semblance along the dip and transformed back into the time-domain; stronger, coherent events have greater weights and contribute proportionally more to the inverse transform (Figure 4.7d). Care must be taken in choosing the dip-range of the input profile, as an inadequate dip-range will produce misleading results. The final processed Chirp profile (Figure 4.8) is characterised by data of high SNR and favourable lateral reflector continuity, contributing to a cleaner and more interpretable profile. Although the final profile of Figure 4.8 has been converted to instantaneous amplitude earlier in the processing history, the section appears to possess polarity information. However, this negative component is attributable to additive effects caused by the application of the coherency-enhancing filters discussed above, and must not be interpreted as real events. Close comparison between Figures 4.6 and 4.8 and knowledge of the local geology (West, 1980) indicate the coherent reflection events in the final processed section are real events and not processing artefacts.

4.4 *Conclusions*

Correlation and deconvolution of Chirp data are greatly facilitated by detailed knowledge of the source-signature. An improvement of greater than 60 dB in SNR on the uncorrelated data is realised from correlating the FM reflected data with the transmitted pulse. Effective deterministic deconvolution is accomplished by designing an inverse filter based on the autocorrelation of the source waveform (the Klauder wavelet). Interpretability of the Chirp profile is further aided by the calculation of the instantaneous amplitude which smoothes the ringy appearance of the deconvolved data in time.

SNR and reflector continuity are enhanced by the application of a series of predictive filters. The effectiveness of these coherency enhancing methods benefits from the repeatability

of the source pulse, as the frequency of the signal content remains relatively constant throughout the correlated profiles, and is therefore readily distinguishable from any arbitrary noise component.

Chapter 5

Imaging wooden artefacts utilising Chirp sources[1]

5.1 *Introduction*

Over the past three decades, marine seismic reflection techniques (echosounders, sidescan sonars and sub-bottom profilers) have been used in the investigation of sites of maritime archaeological interest (McGhee *et. al.* 1968; Frey, 1971; Chauhan and Almeida, 1988; Rao, 1988; Redknap, 1990; Hobbs *et. al.*, 1994). Traditionally, the application of sub-bottom profiling techniques to maritime archaeology has been restricted by poor resolution and an inability to image the seabed in very shallow water depths.

Recent advances in both acquisition and processing techniques have culminated in the development of a system known as Chirp, a high-resolution, digital, frequency-modulated (FM) sub-bottom profiling system. Chirp has proven itself as a useful surveying tool in disciplines where high vertical resolution is a necessity, *e.g.* environmental and cable and pipe laying operations (Schock and LeBlanc, 1990; McGee, 1990). The authors believe that Chirp is the first suitable sub-bottom profiling technique required for detailed investigations of maritime archaeological sites.

5.2 *The seismic reflection method*

The success of the seismic reflection method is dependent upon the presence of resolvable acoustic impedance contrasts within the sub-surface. Acoustic impedances (the product of density, ρ, and compressional wave velocity, V_p) can be used to define the reflection coefficient, K_R, which is a measure of the strength of the reflection (Anstey, 1981):

$$K_R = \frac{\rho_2 V_{p2} - \rho_1 V_{p1}}{\rho_2 V_{p2} + \rho_1 V_{p1}}. \qquad (5.1)$$

A reflection will occur at a boundary if a contrast exists between the acoustic impedances of the media. The polarity of the reflection coefficient is dependent on whether there is an increase (positive reflection) or decrease (negative reflection) in ρV_p across the interface. In normal sub-surface geological situations, values of K_R fall into the range of ± 0.1 (Anstey, 1981), with the majority of the energy being transmitted.

[1] Quinn, R., Bull, J.M. and Dix, J.K., 1997, *Archaeological Prospection*, 4: 25-35.

5.3 *Wood structure and elasticity*

The compressional wave velocity in any material is dependent upon the state of isotropy of the material. Conventional seismic theory assumes material isotropy and therefore a single compressional wave velocity. Wood, however, is a composite, anisotropic material (Flinn and Trojan, 1981; Smith, 1986; Weidmann *et. al.,* 1990), and a single compressional wave velocity does not accurately characterise a wood species. An understanding of this anisotropy is fundamental in calculating compressional wave velocities for wood. The following section briefly examines the nature of wood anisotropy and comments on the variability in the elastic properties of wood.

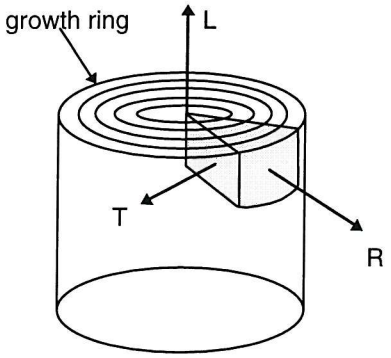

Figure 5.1 Diagram illustrating the three wood axes: L = Longitudinal, R = Radial and T = Tangential. (Modified from Weidmann *et. al.*, 1990).

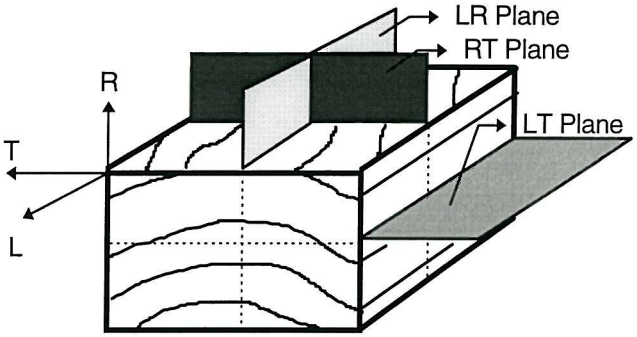

Figure 5.2: Diagram illustrating the three planes of elastic symmetry in wood: LR= longitudinal-radial plane, RT= radial-tangential plane and LT= longitudinal-tangential plane.

In order to correlate a given direction in a tree with its macrostructure the following set of axes is defined (Figure 5.1): the axis parallel to the tree stem is called the longitudinal axis (L), while the axis perpendicular to the annual growth rings is called the radial axis (R). The third axis, the tangential axis (T), is parallel to the growth rings and perpendicular to both the L and R (Hearmon, 1948; Flinn and Trojan, 1981; Smith, 1986; Weidmann *et. al.* 1990).

The theory of wood elasticity rests on the assumption that the gross material possesses three mutually perpendicular planes of elastic symmetry (Figure 5.2), and that it is perfectly elastic and homogeneous (Hearmon, 1948). Wood however is only an approximation to this ideal material. The longitudinal-tangential surface (generated by a line parallel to the axis of the tree and moving along the growth rings) is not a plane, but roughly cylindrical. The other two planes of elastic symmetry are more truly planar, but even in these some deviations occur due to growth irregularities (Hearmon, 1948).

The extent to which a specimen departs from the ideal material is dependent on the position of the specimen within the framework of the tree. If the distance of the specimen from the centre of the tree is large in comparison to the sample dimensions, the effect of curvature of the longitudinal-tangential plane is minimal (Hearmon 1948), and this surface is more truly planar. The values of elastic constants within a single tree can vary by 20% and specimens from different trees of the same species may differ by a factor of 2:1 (Hearmon, 1948). Throughout

this paper, when calculating compressional wave velocities in wood, the assumption of a planar longitudinal-tangential surface is made.

5.4 *Compressional wave velocities in wood*

The compressional wave velocity in a wood sample is dependent upon the orientation of the incident compressional wave relative to the axes/planes of elastic symmetry. Pure compressional waves are those in which the direction of particle displacement coincides with the direction of wave propagation. Pure compressional waves can therefore only occur in solids whose dimensions in all directions are greater than a wavelength (Cremer *et. al.,* 1973). Thus, only some seismic waves are pure compressional waves. When dealing with a natural material such as wood, samples are rarely (if ever) of sufficient extent in all directions to support pure compressional waves. This paper treats the wooden specimens as plates (thus mimicking planks of wood as used in ship construction), where at least one sample dimension is smaller than a single wavelength. Figure 5.3 outlines the three possible end-member cases for a compressional wave incident upon a wood sample. It must be stressed that these are end-member cases, and any intermediate case is possible.

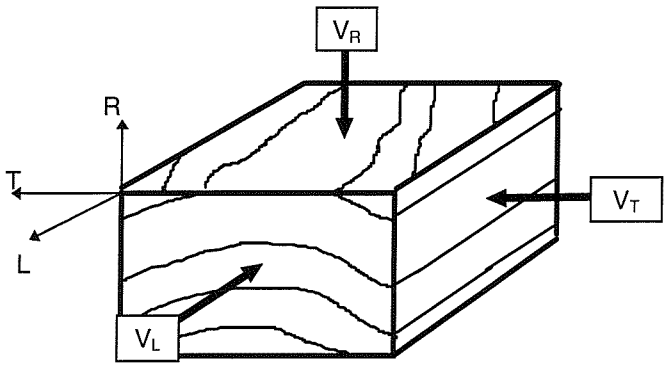

Figure 5.3: Diagram illustrating the three end-member cases (V_L, V_R and V_T) for a compressional wave incident upon a plank of wood.

The compressional wave velocity incident on a plate is calculated from:

$$v_p = \sqrt{\frac{E}{\rho(1-\mu^2)}}, \qquad (5.2)$$

(Cremer *et. al.*, 1973), where E is the Young's modulus (ratio of stress to strain in the tension direction), μ is Poisson's ratio (the ratio of lateral extension to longitudinal contraction) and ρ the density.

For the three independent cases outlined in Figure 5.3, the compressional wave velocities are calculated by:

$$v_L = \sqrt{\frac{E_L}{\rho(1-\mu_L{}^2)}} \qquad v_R = \sqrt{\frac{E_R}{\rho(1-\mu_R{}^2)}} \qquad v_T = \sqrt{\frac{E_T}{\rho(1-\mu_T{}^2)}} \qquad \text{(5.2 a,b,c)}$$

where the average Poisson Ratio in the direction of applied stress is used. Results of the calculated compressional wave velocities of the eleven wood species are listed in Table 5.1.

Wood Species	Density kgm^{-3}	E_L GNm^{-2}	E_R GNm^{-2}	E_T GNm^{-2}	μ_L	μ_R	μ_T	v_L ms^{-1}	v_R ms^{-1}	v_T ms^{-1}
Ash	670	15.8	1.51	0.80	0.49	0.38	0.20	5570	1620	1120
Beech	750	13.7	2.24	1.14	0.48	0.41	0.20	4870	1890	1260
Birch	620	16.3	1.11	0.62	0.46	0.41	0.20	5780	1470	1020
Maple	590	10.0	1.52	0.87	0.48	0.46	0.22	4690	1810	1250
Mahogany	530	12.4	0.97	0.48	0.43	0.43	0.22	5360	1500	980
Oak	660	5.3	2.14	0.97	0.42	0.39	0.19	3120	1960	1230
Walnut	590	11.2	1.19	0.63	0.56	0.39	0.20	5260	1540	1050
Poplar	380	9.7	0.89	0.41	0.36	0.36	0.17	5420	1640	1050
Douglas Fir	480	15.7	1.06	0.78	0.37	0.21	0.19	6160	1520	1300
Scots Pine	580	16.3	1.10	0.57	0.47	0.36	0.16	6010	1480	1000
Spruce	390	10.7	0.71	0.43	0.45	0.27	0.17	5870	1400	1070

Table 5.1: Table of wood density, Young's modulus (E), Poisson's ratio (m), and compressional wave velocities calculated from Equations 5.2 a-c for the eleven wood species. (Density, Young's modulus and Poisson's ratio data is from Hearmon, 1948).

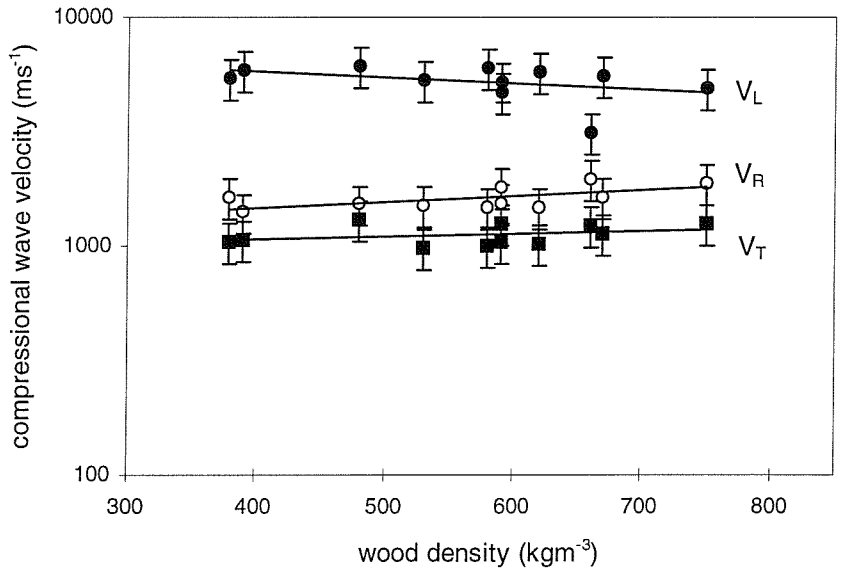

Figure 5.4: Log-linear plot of compressional wave velocity against density for the 11 wood species of Table 5.1. Errors of 20% on individual values are used (Hearmon, 1948).

Figure 5.4 is a log-linear plot of compressional wave velocity against density for the eleven wood species represented in Table 5.1. The compressional wave velocities along-grain (V_L) are consistently faster than those across-grain (V_R and V_T). Best-fit lines (least-squares method) plotted against the point distribution demonstrate a divergent relationship with

decreasing density for along-grain and across-grain values. This relationship indicates the anisotropy of wood decreases with increasing density.

5.5 *Experiment on oak samples from the* Mary Rose

British-built pre-19th-Century wooden ships were traditionally constructed from oak, with lesser components of mahogany, pine and elm (Adams *pers. comm.)*. In order to validate the theoretically derived compressional wave velocities, a series of experiments were carried out on an a suite of oak samples from the hull structure of the *Mary Rose* (King Henry VIII's flagship), which was wrecked off the south coast of England in 1545, and subsequently raised in 1982. The experimental work on the wood samples was conducted in conjunction with the Institute of Sound and Vibration Research at the University of Southampton. Two experimental configurations were used. The first set of experiments were designed around a 1.82 m oak beam taken from the hull of the wreck. Due to sample dimensions, only the compressional wave velocity in the longitudinal direction (V_L) was measured. The second set of experiments were conducted on a series of incrementally cored samples (5 mm diameter) taken from the outer portions of timbers which were in direct contact with the burial sediments.

Figure 5.5 shows the experimental configuration for the beam experiment. In order to ensure good contact between the wood and the force transducer, the beam was suspended from a stable platform by means of angled cables. At the opposite end of the sample, an accelerometer was attached via a self-tapping screw, ensuring minimal structural damage to the beam. Throughout the experiment, the sample was kept in a plastic coating to ensure minimal moisture loss, and was insulated from direct contact with the cables by means of heavy cotton padding.

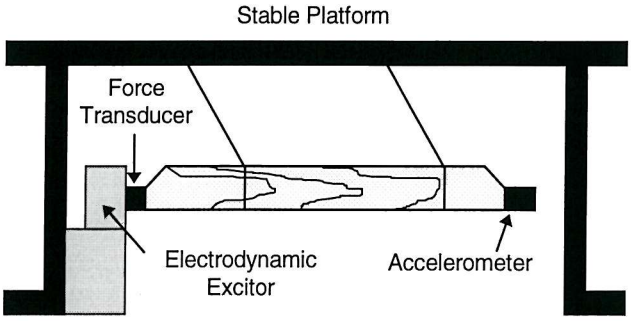

Figure 5.5: Schematic of the experimental configuration for the estimation of V_L from the oak sample taken from the *Mary Rose*.

Two experimental methods were employed to produce independent values for the compressional wave velocity of the beam in the longitudinal direction:

(1) The Phase-Delay Method

The phase at both ends of the beam was measured via the force transducer and the accelerometer, and the variation in phase ($\Delta\phi$) was recorded with change in frequency (Δf). The compressional wave velocity was then calculated from:

$$v_p = \frac{\Delta\omega\Delta x}{\Delta\phi}, \qquad (5.3)$$

where $\Delta\omega = 2\pi\Delta f$, Δx is the beam-length and $\Delta\phi$ is the phase delay.

(2) The Cross-Correlation Method

A compressional wave was transmitted down the length of the beam by the force transducer. The transmitted wave was measured initially at the force transducer and again at the accelerometer, and the resulting signals were cross-correlated. The correlation peak gave the transit time for the compressional wave to travel the beam-length. The compressional wave velocity was calculated by dividing the length of the sample (Δx) by the transit time (t):

$$v_p = \frac{\Delta x}{t}. \tag{5.4}$$

Graphical representation of the experimental results on the oak beam are shown in Figure 5.6. The linear relationship demonstrated between phase and frequency in Figure 5.6 (a) indicates that no interference from bending waves was introduced into the experiment and that the propagating compressional wave is frequency independent, thus validating the experimental methods employed.

The second set of experiments measured the Young's modulus (E) of the cored oak samples and the compressional wave velocity of each cored sample was subsequently calculated from:

$$v_p = \sqrt{\frac{E}{\rho}}, \tag{5.5}$$

where ρ is the density of the cored oak samples measured in the laboratory (average density of 997 kgm^{-3}).

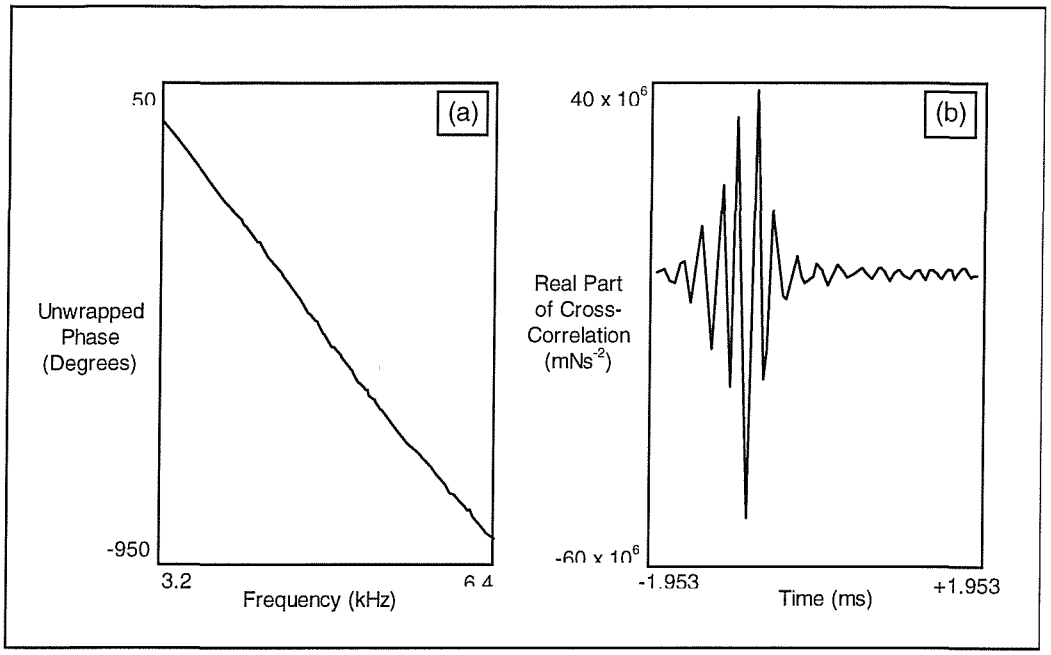

Figure 5.6: Graphical representation of the experimental results on the oak beam: (a) results from the phase-delay method; (b) results from the cross-correlation method.

5.6 *Comparison of theoretical and experimental results*

Table 5.2 summarises the theoretically derived oak values and experimental results for the oak beam. The data series agree within error limits, thus supporting the theoretically derived compressional wave velocities. Differences in velocity values may be explained by the large variations in elastic properties between individual wood specimens. Experimental work on the cored samples from the outer 5 cm of timbers from the *Mary Rose* (all values lie around 1,000 ms^{-1}) demonstrate that oak samples that have been in close proximal contact with the marine environment are degraded and possess more isotropic elastic properties. Evidence from the core samples suggest that structural degradation is most intense in the outer few centimetres of the oak specimens. The inner wood of the beam is more structurally sound and demonstrates less degradation than the core samples when compared to the theoretically derived compressional wave velocity of oak (Table 5.2).

Calculation Method	V_L (ms^{-1})	V_R (ms^{-1})	V_T (ms^{-1})
Theoretical	3,120 (± 20%)	1,960 (± 20%)	1,230 (± 20%)
Experimental: Phase Delay	2,370 (± 15%)	–	–
Experimental: Cross-Correlation	2,300 (± 15%)	–	–

Table 5.2: Table summarising the compressional wave velocities calculated for oak from theory and experiment.

These results correlate with the findings of Wilson *et. al.* (1993) who studied the degradation of oak from ships wrecked in the Indian Ocean (over the period 1629 to 1886) using geochemical techniques. These authors concluded that the degradation of outer wood samples (those in close contact with the marine environment) is due to loss of carbohydrates, whereas the inner wood of the timbers is protected from this loss and remains structurally sound. Furthermore, the authors concluded that inner wood samples are relatively undegraded when compared with modern oak and there appears to be no correlation between the age of wood and the degree of degradation.

5.7 *Reflection coefficients of wood samples from the marine environment*

In order to assess the probability of imaging buried wooden artefacts, a series of K_R calculations (Equation 5.1) were made using the densities and velocities of wood ($\rho_2 V_{p2}$) listed in Table 1 and published density and velocity information of unconsolidated marine sediments ($\rho_1 V_{p1}$) listed in Table 5.3. Results of the calculated reflection coefficients between the two media are listed in Table 5.4.

Lithology	Density ($kg\ m^{-3}$)	Compressional Wave Velocity (ms^{-1})
Sand	2,100	1,734
Sand-silt-clay	1,740	1,575
Clay	1,450	1,496

Table 5.3: Table of typical density and velocity values for unconsolidated marine sediments (Orsi and Dunn, 1991).

The resulting reflection coefficients range between -0.8 and +0.27, while the majority of the K_R values lie between -0.2 and -0.8, i.e. K_R values of wood buried in unconsolidated marine sediments are generally large and negative. The magnitudes of the reflection coefficients indicate that reflected disturbances possess 20 - 80 % of the incident amplitude and suggest wooden artefacts will be readily imaged by a suitable seismic reflection system. Anstey (1981)

Wood Species	K_R V_L in sand	K_R V_R in sand	K_R V_T in sand	K_R V_L in sand-silt-clay	K_R V_R in sand-silt-clay	K_R V_T in sand-silt-clay	K_R V_L in clay	K_R V_R in clay	K_R V_T in clay
Ash	[+0.012]	-0.541	-0.658	+0.153	-0.433	-0.570	+0.265	-0.333	-0.486
Beech	[+0.002]	-0.440	-0.588	+0.143	-0.318	-0.487	+0.255	-0.210	-0.393
Birch	[-0.008]	-0.600	-0.704	+0.133	-0.501	-0.625	+0.246	-0.408	-0.549
Maple	-0.136	-0.546	-0.663	[+0.005]	-0.439	-0.576	+0.121	-0.340	-0.493
Mahogany	-0.124	-0.642	-0.750	[+0.018]	-0.550	-0.681	+0.134	-0.464	-0.614
Oak	-0.278	-0.476	-0.635	-0.142	-0.359	-0.543	-0.026	-0.253	-0.455
Walnut	-0.080	-0.601	-0.709	+0.062	-0.502	-0.631	+0.177	-0.410	-0.556
Poplar	-0.277	-0.708	-0.802	-0.142	-0.629	-0.746	-0.026	-0.554	-0.689
Douglas Fir	-0.104	-0.666	-0.707	+0.038	-0.579	-0.629	+0.154	-0.497	-0.553
Scots Pine	-0.022	-0.618	-0.725	+0.120	-0.523	-0.651	+0.233	-0.433	-0.578
Spruce	-0.228	-0.739	-0.794	-0.090	-0.668	-0.736	+0.027	-0.598	-0.677

Table 5.4: Table summarising the reflection coefficients calculated for the 11 wood species of Table 5.1 buried in the marine sediments of Table 5.2. The K_R values in square brackets are unlikely to be imaged by reflection seismology as the contrast in acoustic impedances are too low to give rise to a distinct reflection.

states that values of $K_R = \pm 0.3$ are unusual in the earth as it is rare that such contrasting materials should be brought into contact. Clearly however, in the realm of maritime archaeology, such high order reflection coefficients are the norm rather than the exception.

5.8 *Chirp technology and acquired data*

Having established theoretically and experimentally that it is possible to image buried wooden artefacts in the marine environment, the authors surveyed a site of maritime archaeological interest using a combined array of a dual frequency side-scan sonar mounted on a Chirp towed transducer system. The *Invincible* site (Horsetail, East Solent, U.K.) was chosen as a test site as it offered the opportunity to acquire data over an 18th-Century oak wreck partially buried by unconsolidated sediments. The Invincible (originally L' Invincible), a 74 gun third rate, was captured from the French in 1747 and wrecked in 1758. The site of her loss, relocated in 1979, has been partially excavated and a large number of objects have been raised and conserved (Lavery, 1988).

The geophysical survey was conducted utilising a 100 kHz side-scan sonar combined with a 2 to 8 kHz swept frequency Chirp system in an average water depth of 6m. Throughout the survey, a transmit rate of four pulses per second was used in the acquisition of digital side-scan and sub-bottom data. Navigation data, with an accuracy of ±1m, was provided by a differential global positioning system (DGPS).

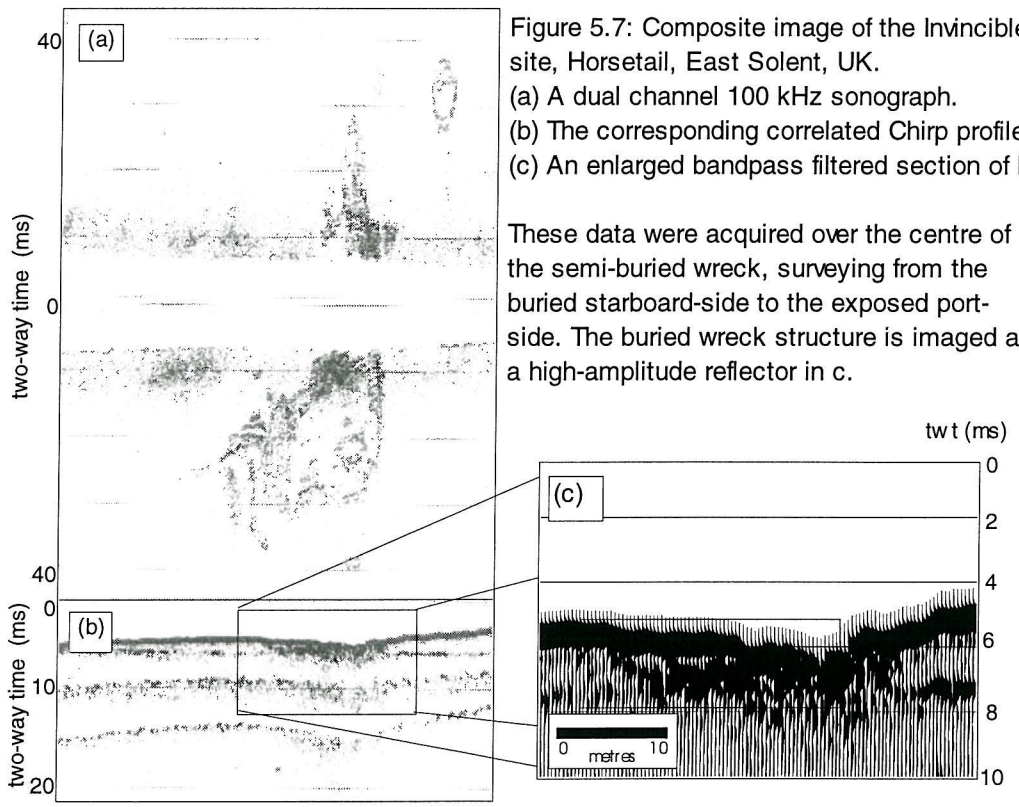

Figure 5.7: Composite image of the Invincible site, Horsetail, East Solent, UK.
(a) A dual channel 100 kHz sonograph.
(b) The corresponding correlated Chirp profile.
(c) An enlarged bandpass filtered section of b.

These data were acquired over the centre of the semi-buried wreck, surveying from the buried starboard-side to the exposed port-side. The buried wreck structure is imaged as a high-amplitude reflector in c.

Figure 5.7 is a composite image of one line acquired over the site. It is evident from the side-scan image that a large portion of the wreck was exposed on the seabed at the time of survey. The filtered profile of section (c) clearly images the buried port side of the wooden wreck, providing proof that reflection seismology can image buried wooden artefacts.

A reflection coefficient of the wreck (oak buried in unconsolidated marine sediments) was subsequently calculated to compare to the theoretically derived K_R values listed in Table 5.4. The reflection coefficient of the seafloor ($K_{R_{sf}}$) is estimated from the relative amplitudes of the primary seafloor reflector (A_p) and its first multiple (A_m) by:

$$K_{R_{sf}} = G\frac{A_m}{A_p}, \qquad (5.6)$$

(Anstey, 1977; Warner, 1990; Spence *et al.*, 1995). G is the correction made for spherical spreading , which is proportional to two-way time. As the two-way time of the first multiple is twice that of the primary, the value of G is equal to 2 in equation 5.6.

The reflection coefficient of the wreck reflector (K_{Rwreck}) is estimated by comparing the amplitude of the wreck reflector (A_{wreck}) with that of the primary seafloor reflector (A_p):

$$K_{R_{wreck}} = K_{R_{sf}} G\frac{A_{wreck}}{A_p}, \qquad (5.7)$$

(Warner, 1990; Spence *et al.*, 1995). The spreading correction (G) is equal to the two-way time for the deeper reflector divided by that of the seafloor primary for individual traces. A full explanation of the methodology for calculating reflection coefficients from Chirp data is outside the scope of this paper, however the results are presented:

$K_{R(sf)} = +0.43$

$K_{R(wreck)} = -0.27$

A comparison of the reflection coefficient of the wreck calculated from the Chirp data (-0.27) to those values predicted from theory in Table 5.4 (range: -0.03 to -0.64) indicates that the reflection coefficient calculated from the digital sub-bottom data falls centrally within the range predicted by the modelling, thus supporting the theoretical and experimental work outlined above. A more complete discussion on the calculation of the reflection coefficients from Chirp data and the associated errors are discussed in detail in Chapter 6.

5.9 *Conclusions and discussion*

- The anisotropy of wood decreases with increasing density, with compressional wave velocities parallel to the wood grain (V_L) being consistently faster than those across grain (V_R and V_T).

- Burial in marine sediments cause changes in the physical and elastic properties of the outer few centimetres of wood samples, causing outer wood to behave more isotropically. In contrast, inner wood displays less degradation in structural coherency. Elastic and physical properties remain relatively constant.

- Variations in reflection coefficients of wood buried in unconsolidated sediments (+0.27 to -0.79) are dependent upon the wood-species, sediment-type and burial and exposure histories.

- Reflection coefficients resulting from wood buried in unconsolidated marine sediments are typically large and negative. Reflection coefficients calculated for oak (historically the most common ship-building material) buried in sediments range between -0.03 and -0.64.

Theoretical, experimental and acquired sub-bottom data presented in this paper clearly indicate that wooden artefacts buried in unconsolidated marine sediments can be readily imaged by seismic reflection techniques. Due to the nature of seismic data acquisition, the ability to image wooden artefacts is not only dependent upon the acoustic impedance contrast that exists between the artefact and the burial sediment, but also upon the size of the target. This size restriction is a direct function of the acquisition parameters of the sub-bottom system. In practical terms, an artefacts' dimensions must be greater than 1m in the horizontal plane and greater than 12.5 cm in the vertical in order to be imaged by a Chirp system utilising a 2-8 kHz source at a system transmit rate of 4 pulses per second in water depths of less than 30m.

Figure 5.7, and the associated reflection coefficients calculated from the sub-bottom profile strongly support the authors belief that Chirp systems (combined with accurate navigation systems and sound survey methods) presently offer the most appropriate technology for non-invasive, high-resolution investigations of sites of maritime archaeological interest.

Chapter 6

The calculation of reflection coefficients from correlated Chirp data[1]

6.1 *Introduction*

In this chapter, a method for the calculation of reflection coefficients from normal-incidence correlated Chirp data is discussed. Having established both theoretically and experimentally that it is possible to image buried wooden artefacts utilising Chirp sources (Chapter 5), a maritime archaeological site was chosen to test the practical implications of seismic surveying over wreck-sites. The *Invincible* site (Horsetail, East Solent, UK) was chosen as a test site as it offered the opportunity to acquire Chirp and digital side-scan data over an 18th century oak wreck, partially buried by unconsolidated sediments[2]. Figure 6.1 is a composite image of one line acquired over the site. It is evident from the side-scan data (6.1 a) that a large portion of the wreck was exposed on the seabed at the time of surveying. The filtered profile of the Chirp section (6.1c) images the buried portion of the starboard side of the wreck as a high-amplitude reflector.

Reflection coefficients of the seafloor and wreck reflectors are calculated from these data to compare with the theoretically derived reflection coefficients of Chapter 5. Synthetic models characterising the seafloor and immediate sub-surface are presented, which examine the effects of decimetric-scale seafloor impedance changes on the polarity of the Chirp pulse.

6.2 *The calculation of reflection coefficients from Chirp sub-bottom data*

6.2.1 *Introduction*

The equation relating the normal incidence reflection coefficient (K_R) to density (ρ) and compressional wave velocity (V_p) above and below an interface is (Anstey, 1981):

$$K_R = \frac{\rho_2 V_{p2} - \rho_1 V_{p1}}{\rho_2 V_{p2} + \rho_1 V_{p1}}. \qquad (6.1)$$

The polarity of the reflection coefficient is dependent upon whether there is an increase (positive reflection or *compressional disturbance*) or decrease (negative reflection or *rarefaction*) in acoustic impedance (ρV_p) across the interface. The acoustic impedance contrast between seawater and the seafloor dictates that a compressional disturbance is expected from the seafloor, *i.e.* K_{Rsf} is positive.

[1] Data presented in 6.2 and 6.3 are in press: Bull, J.M., Quinn, R. and Dix, J.K., *Marine Geophysical Researches.*
[2] The *Invincible* wreck site is discussed in detail in Chapter 8.

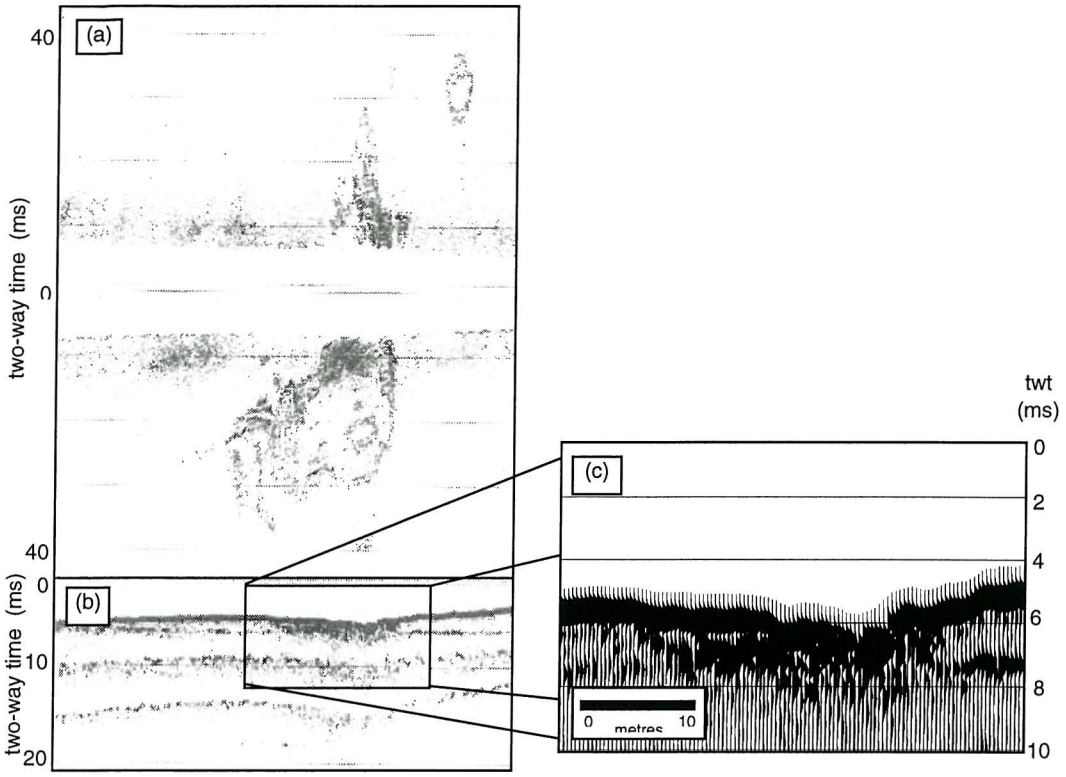

Figure 6.1: Composite image of the Invincible site, Horsetail, East Solent, UK:
(a) A dual channel 100 kHz sonograph; (b) The corresponding correlated Chirp profile;
(c) An enlarged bandpass filtered section of b.Trace interval = 0.5m.

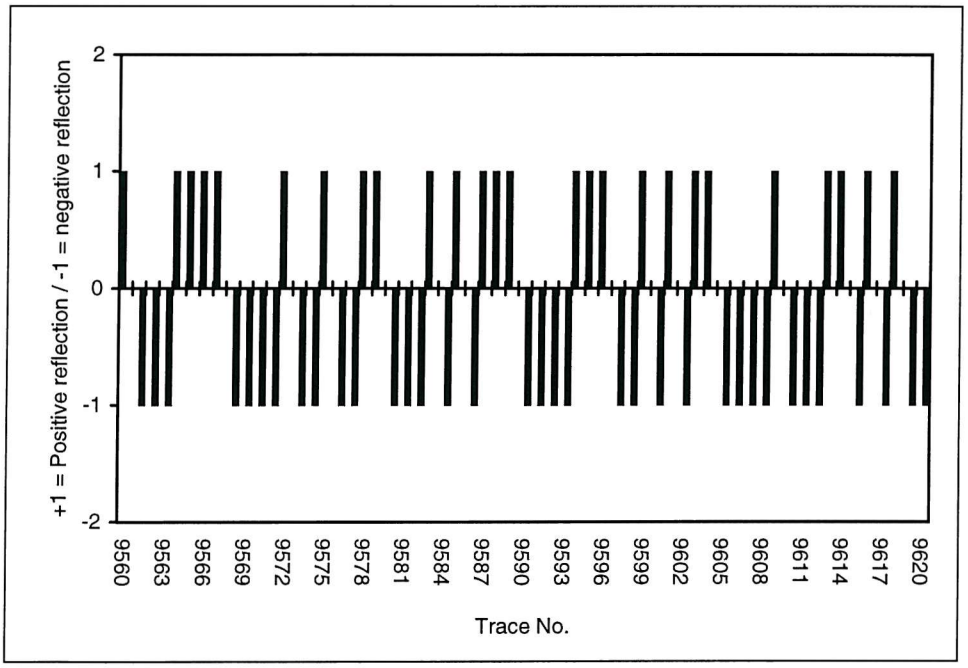

Figure 6.2: Diagram illustrating the random switch in the polarity of the Chirp pulse from the primary seafloor reflector of the *Invincible* site. Positive reflections are assigned a nominal value of +1 and negative reflections a value of -1.

The results from Chapter 5 indicate that the reflection from buried wooden artefacts is generally negative, with the reflection coefficient for oak (historically the most common ship-building material) buried in marine sediments ranging from -0.03 to -0.64.

6.2.2 *Methodology*

The reflection coefficient of the seafloor ($K_{R_{sf}}$) is estimated from the relative amplitudes of the primary seafloor reflector (A_p) and its first multiple (A_m) by:

$$K_{R_{sf}} = G\frac{A_m}{A_p}, \qquad (6.2)$$

(Anstey, 1977; Warner, 1990; Spence *et al.*, 1995). G is the correction made for spherical spreading , which is proportional to two-way time. As the two-way time of the first multiple is twice that of the primary, the value of G is equal to 2 in equation 6.2.

The reflection coefficient of a deeper reflector (K_{Rdr}) is estimated by comparing the amplitude of the deeper reflector (A_{dr}) with that of the primary seafloor reflector (A_p):

$$K_{R_{dr}} = K_{R_{sf}} G\frac{A_{dr}}{A_p}, \qquad (6.3)$$

(Warner, 1990; Spence *et al.*, 1995). The spreading correction (G) is equal to the two-way time for the deeper reflector divided by that of the seafloor primary for individual traces.

This analysis assumes that the air-water interface has a reflection coefficient of -1. For the high-frequency Chirp source used in this analysis, as the wavelength of the system approaches the wavelength of the waves induced on the sea-surface, the value of the air-water coefficient changes. Chapman and Scott (1964) derived an empirical relationship between the scattering strength (or reflection loss), the incidence angle (defined as the angle between the incident wave and the horizontal) and wind-speed for acoustic sources ranging from 100 to 6,400 Hz. Their results indicated that for the frequency range investigated, scattering was source frequency independent. Kuperman (1990) also considered the specular reflection and transmission of an acoustic plane wave at a randomly rough sea-surface using the Pierson-Moskowitz model spectrum for a fully developed sea. Kuperman (1990) derived reflection coefficients as functions of source frequency, incidence angle, wind speed and wind direction.

In the case study discussed below, at the time of data acquisition, the sea-state was calm. Assuming an angle if incidence of 80^{o} (typical for Chirp systems) and a maximum wind speed of 5 ms^{-1}, the relationships derived by Chapman and Scott (1964) and Kuperman (1990) indicate that the loss in reflection strength from the sea-surface for the case study below is c. 0.7-0.8 dB. Thus reflection coefficients may be underestimated by 8-10 %.

The effects of scattering by rough surfaces is considered to be sufficiently small to be ignored for the short travel paths considered here, and are not incorporated within the

expressions for the reflection coefficients in Equations 6.2 and 6.3. Frequency dependent absorption is also not incorporated into the expressions, but is discussed in Section 6.2.3.

6.2.3 *Results*

Reflection amplitudes are altered by many stages in seismic processing and hence when attempting to calculate absolute reflection coefficients it is most valid to work with single-fold unprocessed data. In the analysis below the original uncorrelated data has been correlated with the source sweep, but no further processing has been undertaken. Reflector polarity is determined by identifying the Klauder wavelet associated with the impedance response on each trace. Thus changes in the sign of the maximum of the cross-correlation function are interpreted as polarity changes.

The magnitude of the reflection coefficients calculated for the seafloor and the wreck reflector (K_{Rdr}) from the *Invincible* site are |0.43| and |0.26| respectively. The magnitude of K_{Rdr} is in agreement with that predicted from theory in Chapter 5. However, polarity information from the seafloor and deeper reflectors is inconsistent. Figure 6.2 shows the results of polarity analysis of 60 traces from the seafloor reflector. A value of +1 is assigned to a positive reflection, and -1 to a negative reflection. The resulting pattern displays a random switch in polarity from trace to trace. Although there is a bias towards a compressional disturbance from the seafloor (54% positive polarity) and rarefaction from the oak reflector (64% negative polarity) analysed in the *Invincible* data, the results are inconclusive.

Reflector	Magnitude of Reflection Coefficient $\|K_R\|$	Standard Deviation (σ)	Reflector Polarity (No trace mixing)	Reflector Polarity (Trace mixing = 3)	Reflection Coefficient K_R
Seafloor (primary)	|0.43|	0.18	54% positive 46% negative	79% positive 21% negative	**+0.43**
Deeper reflector (wreck)	|0.27|	0.12	36% positive 64% negative	31% positive 69% negative	**-0.27**

Table 6.1: Summary of the polarity and reflection coefficient information from a Chirp profile acquired over the *Invincible* site.

Due to this inconsistency in polarity information from the correlated Chirp data, a trace-mixing algorithm (a running average over traces with equal weight) is applied to the sub-bottom data to determine reflector polarities. A series of empirical tests determined that a 3 trace running mix is most effective in giving a consistent seafloor return. Figure 6.3 displays 5 adjacent traces from the *Invincible* data, emphasising the effectiveness of the trace-mixing

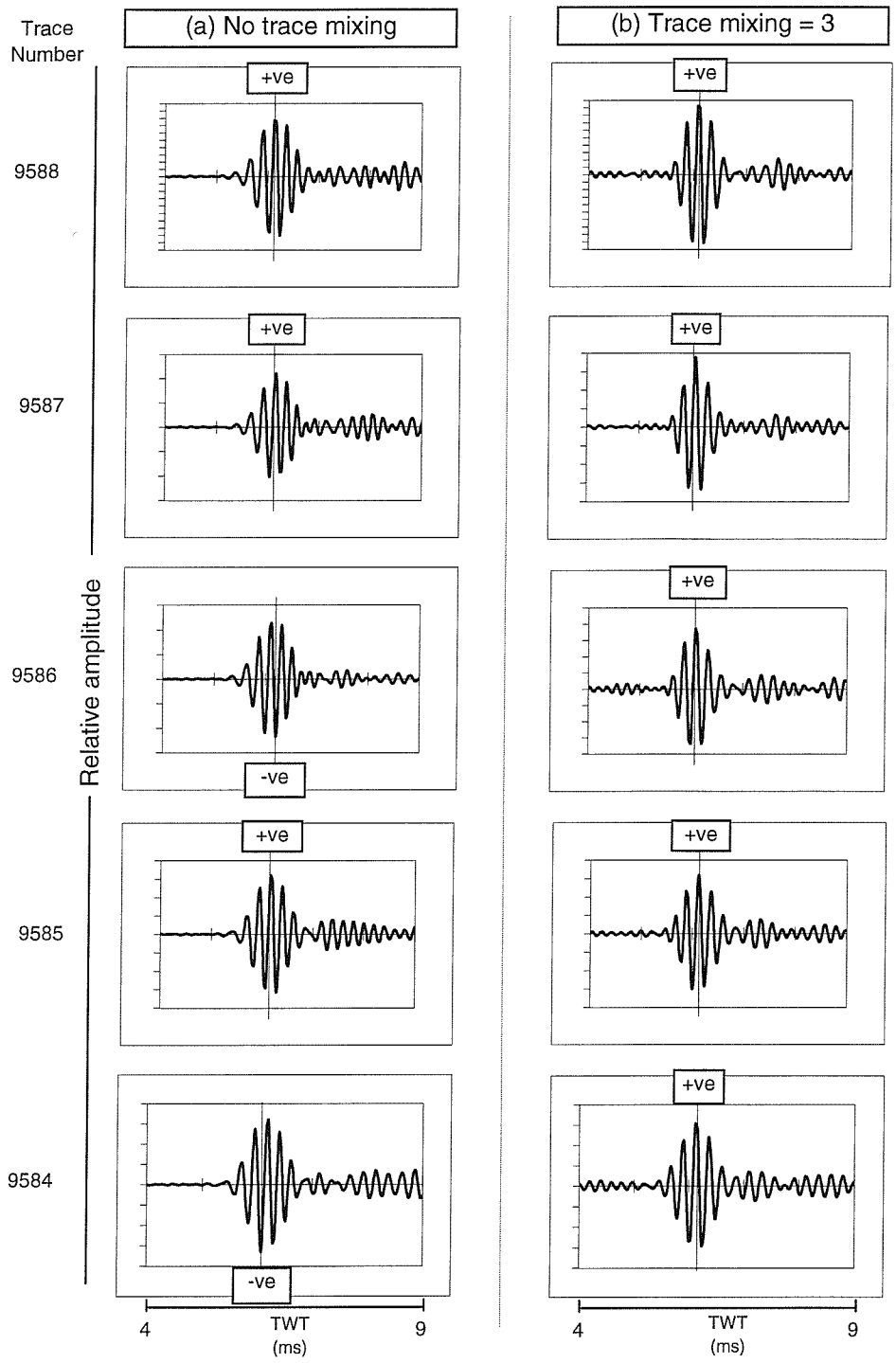

Figure 6.3: Diagram of 5 adjacent traces from the seabed reflector at the *Invincible* site. (a) Prior to trace-mixing: note the apparent random changes in reflector polarity (the position of the maximum amplitude is indicated by the vertical line): (b) The same 5 traces subsequent to the application of the trace mixing algorithm - all reflection events are now positive.

algorithm. Initially, three of the seafloor reflection events are positive and two are negative; subsequent to trace-mixing the five adjacent traces are all positive. Table 6.1 summarises the results of the polarity and reflection coefficient information.

For the shallow burial of wood (< 0.1 ms), the use of standard Q-correction techniques to correct for frequency dependent absorption (Sheriff and Geldart, 1995) suggest that the reflection coefficient calculated for the wood reflector may be underestimated by 30%. This, together with the errors caused by considering the air-water interface as a reflector with a coefficient of -1, implies that as a worst case scenario, the reflection coefficient calculated for the wood reflector may be under-estimated by 40%.

6.3 *Geoacoustic modelling of the seafloor*

6.3.1 *Introduction*

Clearly, information on reflector polarity is essential in determining true reflection coefficients from sub-bottom data. An understanding of observed polarity switches is fundamental for the characterisation of sub-bottom events. Any process which alters or controls the physical or elastic properties of sediment also changes the acoustic properties of that sediment (Richardson and Briggs, 1996). The scattering and propagation of high-frequency sound at and within the seafloor are controlled by the physical and geoacoustic properties of sediments (Richardson and Young, 1980) and surface layer roughness (Jackson and Briggs, 1992).

Schock (1996) compiled a database of vertical impedance profiles from the top 30 cm of core data for a variety of depositional environments around the globe. The salient feature observed from these data is that impedance profiles rarely show a step change in acoustic impedance at the seafloor, but rather display gradational changes, typically over the range of 5 to 20 cm. Schock (1996) attributes the changes to bioturbation and compaction, causing a decrease in the amplitude of reflections from the sediment structure. Instead of a step change at the interface between two sedimentary layers, a transition zone usually exists between successive sediment horizons, caused by sediment mixing and depositional processes.

Akal (1972) proposed that the porosity of marine sediments is the most important parameter causing variations in p-wave velocity, density and reflection coefficient. Bioturbation modifies the porosity, grain-size, density, fabric and general cohesion of unconsolidated marine sediments, generally lowering p-wave velocity and impedance of sediments (Richardson and Young, 1980).

Another factor influencing the attributes of seismic data is fine-scale sub-bottom layering. Mayer (1979) observed that high-resolution reflections from the top 10m of pelagic carbonates are often not caused by discrete geological horizons, but rather are interference composites caused by many small interfaces. A similar phenomenon is noted by Slowey *et al.* (1996) in high-resolution profiles from Eckernförde Bay. Impedance profiles produced from the Eckernförde data typically display small, closely spaced changes reflecting subtle sediment layering. The layer thickness is less than the wavelength of the seismic source, so reflections

from individual layers combine to form interference composites, so that the reflectors imaged on the high-resolution profiles do not correspond one-to-one with the sedimentary layers from core data.

In summary, any physical or biological activity that affects the cohesion, fabric and surface roughness of unconsolidated marine sediments, directly affects their fundamental acoustic properties.

6.3.2 *Synthetic modelling*

A geoacoustic model is a model of the seafloor with emphasis on values of those properties important in underwater acoustics and aspects of geophysics involving sound transmission (Hamilton, 1980). In general, a geoacoustic model details the thickness and physical properties of sediment layers comprising the seafloor.

In order to examine the effects of a layered seafloor on the behaviour of the Chirp pulse, a series of synthetics were produced by convolving the Chirp Klauder wavelet with geoacoustic models representing transitional zones within the seafloor and immediate sub-bottom. All modelling exercises conducted in this chapter are for a 32 ms, 2-8 kHz Chirp source (f_d = 5 kHz, λ_d = 0.3m for V_p = 1500 ms^{-1}), sampled at a rate of 40μs. The geoacoustic models of the seafloor are constrained by impedance variations between $1.54x10^6$ and $3.0x10^6$ $kgm^{-2}s^{-1}$ (Schock, 1996).

Two seafloor boundary conditions are modelled:

(a) *The transition zone model*

The *transition zone model* follows Schock (1996) in treating the seafloor as a stratified fluid. The model divides the fluid into layers that have a thickness much less than the acoustic wavelength. In this case, an interlayer thickness of 40 μs is used, corresponding to the sample interval of the Chirp data. Synthetics are produced by convolving the Klauder wavelet with impulse responses constructed over a transition zone of increasing vertical extent. Figure 6.4 shows *representative* models and their seismic response.

(b) *The surficial sediment model*

The *surficial sediment* model investigates the interaction of the Klauder wavelet with two spikes of increasing separation, representing a surficial sediment cover of increasing thickness. Figure 6.5 shows *representative* models and their seismic response.

The synthetic traces generated from both models indicate that small changes in vertical and horizontal impedance of the seafloor cause random switches in the polarity of the Klauder wavelet. In Figure 6.4 (a), the seismic response to the single spike is an exact replica of the Klauder wavelet, scaled by a factor dependent upon the amplitude of the spike. However, the seismic responses of subsequent transition zone (Figure 6.4) and surficial sediment (Figure 6.5) models indicate that the polarity of the reflected disturbance (determined

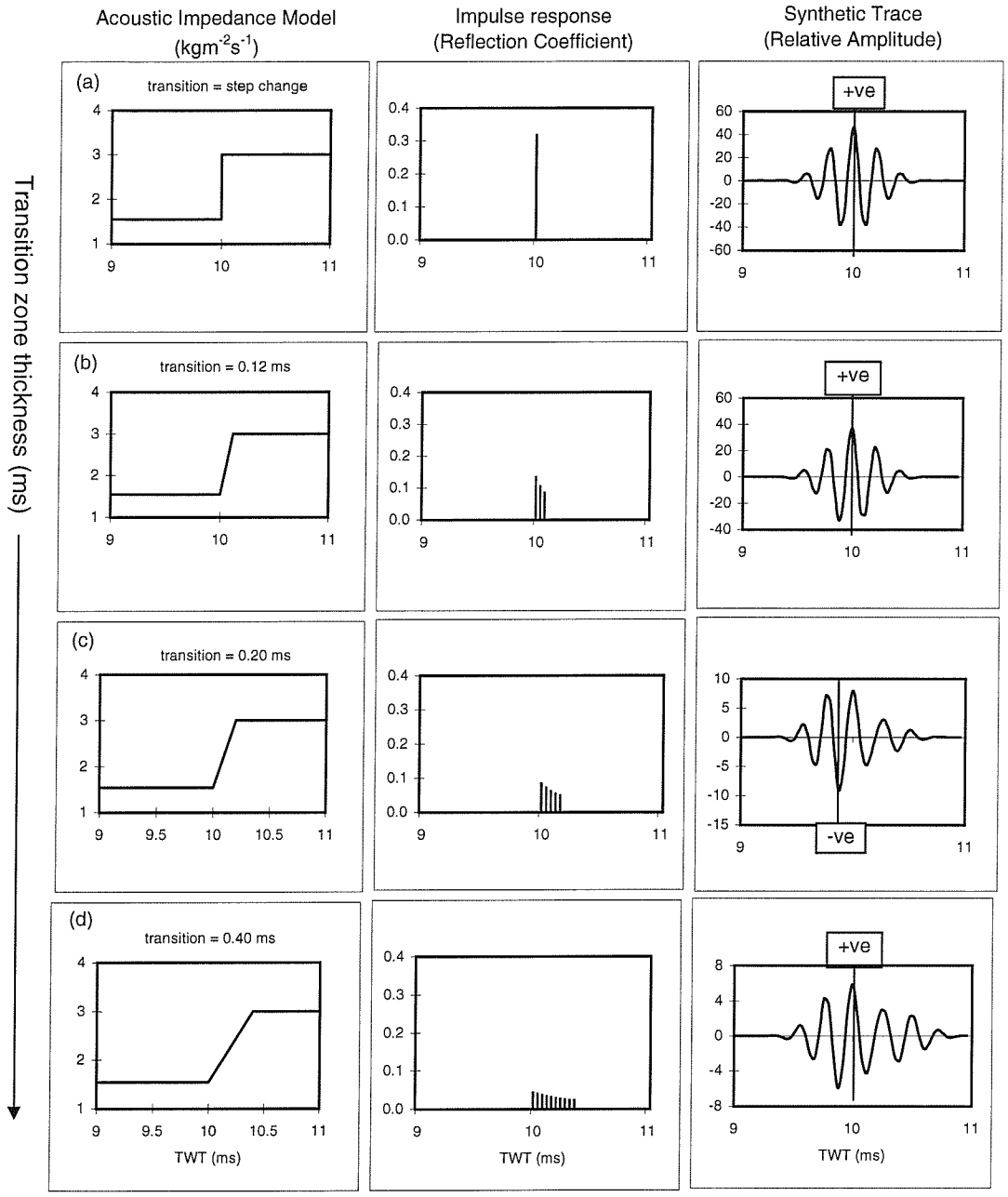

Figure 6.4: Diagram illustrating the effects of a seafloor transition zone on the Chirp wavelet. Acoustic impedance profiles are shown on the left hand side, impulse responses in the centre and the generated synthetic traces on the right.

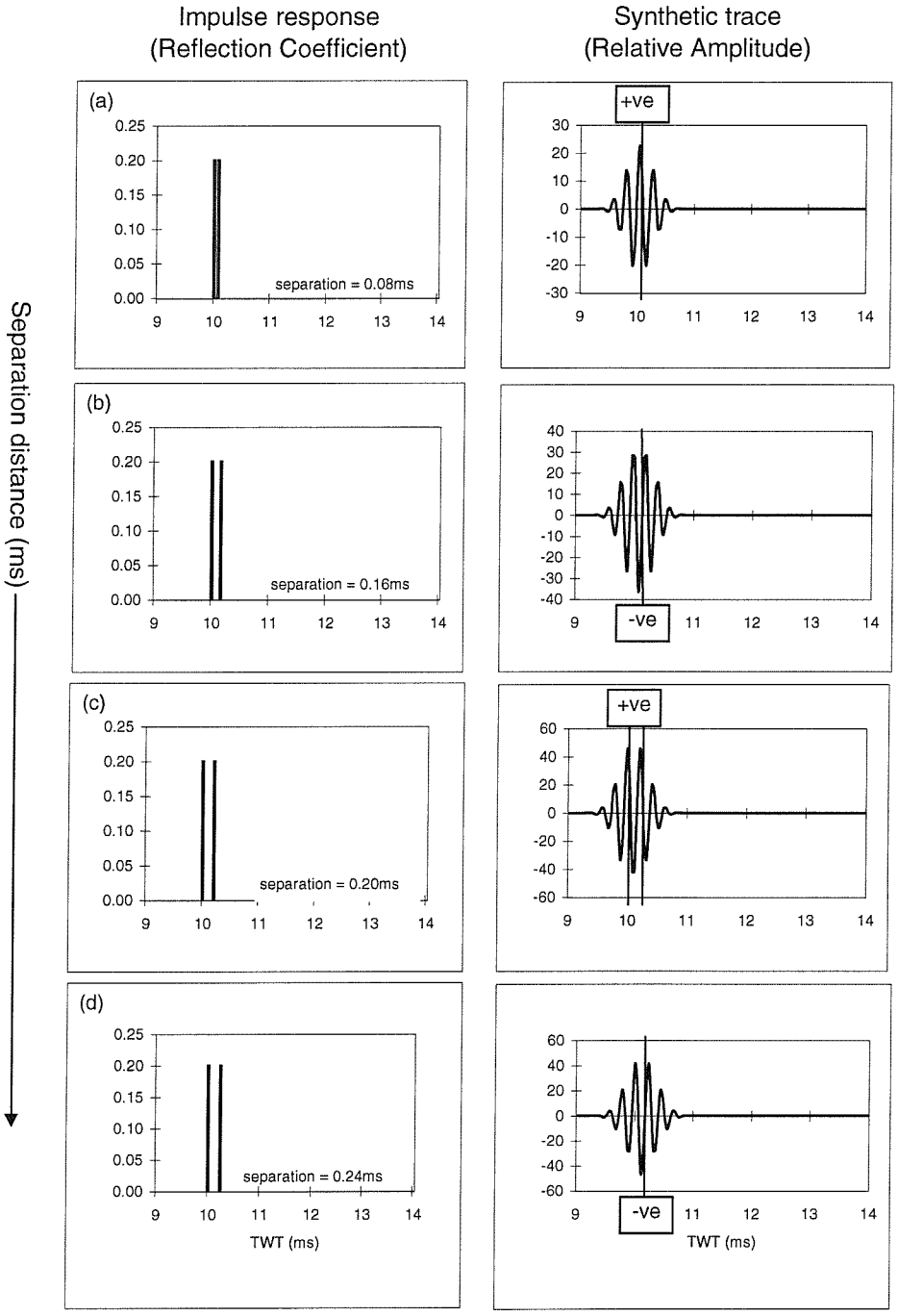

Figure 6.5: Diagram illustrating the effects of variable surficial sediment thickness on the Chirp pulse. The impulse responses are shown on the left and the correponding synthetic traces on the right.

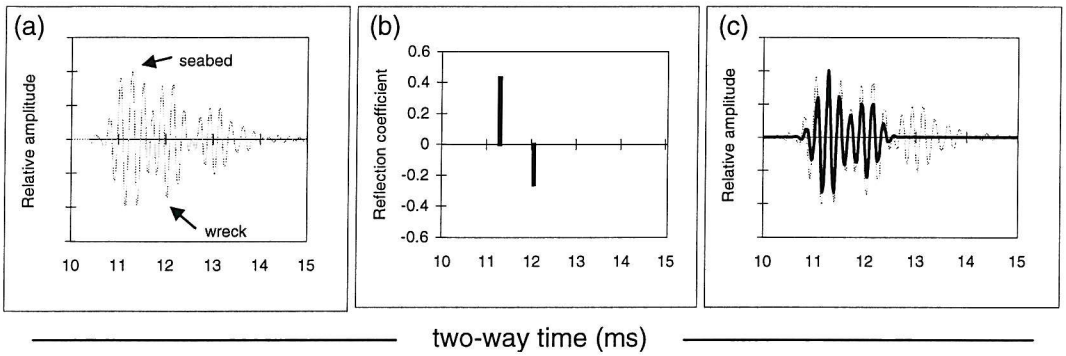

Figure 6.6: (a) Single correlated trace from the buried portion of the *Invincible.*
(b) The impulse response produced from the reflection coefficient calculations from the *Invincible* data. (c) Synthetic trace (heavy line) produced by convolving the Klauder wavelet with the impulse response. Note the excellent correlation between the synthetic (heavy line) and real data (fine line).

by the maximum/ minimum amplitude value) is randomly flipped between overall positive and negative. This switching of polarity is a direct result of interference effects caused by the interaction of reflections from each thin layer. The composite waveforms produced in the models destructively interfere with one another, causing the maximum/minimum amplitude value to vary from positive to negative. In the case of the transition zone model, the Klauder wavelet is effectively smeared over the length of the transition zone.

Schock (1996) concluded that a transition zone at the seabed acts as a low-pass filter, attenuating the high-frequency component of the seismic wavelet through destructive interference. Clearly, the transition zone not only affects the frequency component of the reflection data, but interference effects cause random polarity switches in reflection events. A similar phenomenon is observed from the surficial sediment models.

Other factors which may influence polarity reversals in Chirp data include the sea-state which can effect the angle of incidence of the seismic wave, and the width of the associated Fresnel zone. For a 2-8 kHz source, propagating in a medium of V_p = 1500 ms^{-1}, the limits of horizontal resolution (R_h) at a two-way travel time of 10 ms (7.5m) are: 3.11m $\geq R_h \geq$ 1.06m (Chapter 3, Section 3.3). Typically Chirp data has a trace interval of 0.6m and hence there is overlap in information on adjacent traces as the trace interval is less than the horizontal resolution of the system. This information overlap may directly contribute to the polarity reversals seen in real Chirp data.

6.4 Discussion and conclusions

The methodology used to calculate reflection coefficients from the *Invincible* data is validated by forward modelling. Figure 6.6 (a) shows a single trace through the seabed and buried wreck. The positions of the two reflectors are highlighted in the illustration. Figure 6.6 (b) displays the impulse response model constructed from the average reflection coefficients calculated from the data (K_{Rsf} = +0.43; K_{Rdr} = -0.26), with a separation of 0.76 ms corresponding to the vertical separation of the reflectors.

The synthetic response (heavy black line) is overlain on the real data (fine black line) in Figure 6.6 (c). Excellent correlation is noted between the real and synthetic data sets, validating the methodology used in the calculations. The difference in amplitudes of the synthetic and real data is readily attributable to the averaging on reflection coefficient information over each reflector.

In summary, the main conclusions from this chapter are:

- Small vertical and lateral changes in the impedance profile of the seafloor cause random switches in the polarity of the Chirp pulse from trace to trace.
- Reflection coefficients can be calculated from normal incidence Chirp data using amplitude-time relationships from single traces and polarity information from trace-mixing.
- The reflection coefficient calculated for oak (from an 18th Century wreck) buried in unconsolidated marine sediments agrees with theoretical and experimental predictions.

Chirp data: K_R = -0.27

Theory: K_R = -0.03 to -0.64,

thereby supporting the methodology used in calculations. Errors involved in calculations suggest that these figures may be underestimated by a maximum of 40%.

Chapter 7

Buried scour marks as indicators of palaeo-current direction - The *Mary Rose* wreck site[1,2]

7.1 *Introduction*

Over the past thirty years, various marine seismic reflection techniques have been used in the investigation of sites of archaeological interest, (McGhee *et. al.*, 1968; Frey, 1971; Redknap, 1990). During this period, success has been met with the use of high resolution side-scan sonar and echosounder systems to identify archaeological artefacts lying on the seabed. Such systems cannot penetrate the subsurface and are therefore unable to image buried artefacts. In consequence, a number of workers used sub-bottom profiling systems in an attempt to image buried features (Rao, 1988; Chauhan and Almeida, 1988). The suitability of these systems has been restricted by poor spatial resolution and an inability to image the seabed in very shallow water depths. Recent advances in both acquisition and processing techniques have culminated in the development of a system known as "Chirp", a high-resolution, digital, frequency-modulated (FM) sub-bottom profiling system (Schock and LeBlanc, 1990; Parent and O' Brien, 1993).

The aim of this paper is to show how Chirp profiling over buried wreck-sites can be used to infer palaeo-current directions at the time of wrecking and in the period until the wreck structure erodes to a level concordant with the contemporary seabed.

7.2 *Scour marks from the marine environment*

Scour marks are local depressions in a sediment caused by local non-uniformity of flow over the bed (Richardson, 1968). Scour features formed in different substrates in the marine environment have previously been described from sonographs (Werner and Newton, 1975; Caston, 1979; Werner *et. al.*, 1980). These erosional features are found associated with obstacles lying on, or partially buried within, the seafloor. This paper is predominantly concerned with one group of scour features, named wreck marks (Caston, 1979), which form in dynamic environments around ship wrecks.

Abundant wreck marks have been revealed by sonographs from an area of strong tidal currents in the Outer Thames Estuary, U.K. (Caston, 1979). Longitudinal wreck marks have been shown to extend for up to 1 km in the direction of flow of the stronger ebb or flood tidal current. Caston describes a gradational series of these wreck associated scour features, all of which parallel the peak current. The orientation and width of the wreck, relative to the current flow, have been demonstrated as significant factors in determining the length of the wreck marks (Caston, 1979).

[1] Quinn, R., Bull, J.M. and Dix, J.K., 1997a, *Marine Geology*, 140: 405-413.
[2] Quinn, R., Bull, J.M., Dix, J.K. and Adams, J.R.. 1997c, *International Journal of Nautical Archaeology*, 26 (1): 3-16.

The occurrence of double or single wreck marks has been shown to reflect the orientation of the wreck with respect to the peak tidal current flow. Single scour marks emanate from wrecks which measure an average of 13 m across the current and the mean length of these scour shadows is 130 m. Double scour marks, of mean length 400 m, are generated by wrecks with an average width across the flow of 60 m. The shortest and narrowest scour features were found associated with wrecks aligned with their long axis along the current, presenting streamlined shapes to the flow. The majority of scour depths recorded in the Thames Estuary was 1.5 m to 2 m. Caston (1979) demonstrated that wreck mark morphology is dependent on seabed lithology, with wreck marks on a sand floor being characterised by broad, shallow, longitudinally extensive troughs whereas those on gravel floors are relatively narrower, deeper and less extensive. An example of wreck marks is revealed in the sonograph of Figure 7.1. The unequal development of the wreck marks in each direction is due to the oblique alignment of the wreck relative to the peak tidal flow (from left to right).

7.3 *Reflection coefficients and wood*

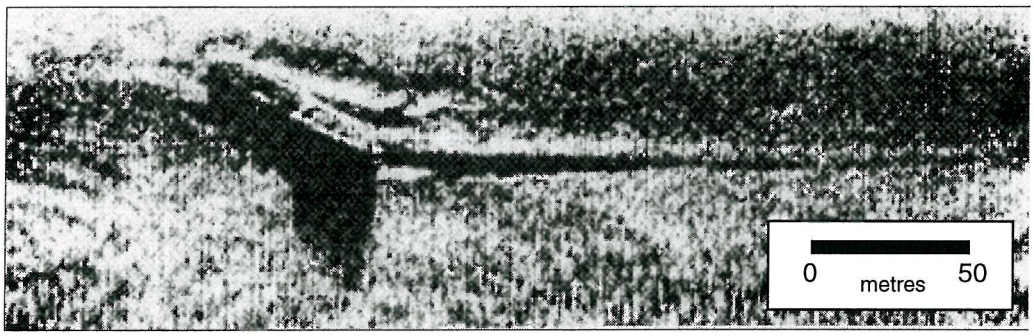

Figure 7.1: Sonograph showing a wreck (55 m long and a maximum of 14 m high) with scour hollows emanating from the bow and the stern. The unequal development of the wreck marks is due to the oblique alignment of the wreck relative to the peak tidal flow (from left to right).

The success of the seismic reflection method is dependent upon the presence of resolvable acoustic impedance contrasts within the sub-surface. Acoustic impedances (the product of density, ρ, and compressional wave velocity, V_p) can be used to define the reflection coefficient, K_R, which is a measure of the strength of the reflection (Anstey, 1981):

$$K_R = \frac{\rho_2 V_{p2} - \rho_1 V_{p1}}{\rho_2 V_{p2} + \rho_1 V_{p1}} \quad . \qquad (7.1)$$

In normal sub-surface geological situations, values of K_R fall into the range of ±0.1 (Anstey, 1981), with the majority of the energy being transmitted. In maritime archaeological situations however, values of K_R tend to have a broader range as anthropogenic materials such as wood are found in direct contact with unconsolidated marine sediments, resulting in higher acoustic impedance contrasts (Quinn *et. al.*, 1997b). Theoretical K_R values between wood and unconsolidated marine sediments can range between -0.8 and +0.3; although the majority of the

values are large and negative, typically between -0.3 and -0.7. This broad range is due to a combination of three factors: sediment type, wood species and the orientation of the incident compressional wave with respect to the planes of elastic symmetry in the wood.

Theoretical reflection coefficients of oak (historically the most common shipbuilding material for pre-19th Century, British-built boats) buried in unconsolidated, shallow marine sediments range between -0.03 and -0.63 (Quinn *et. al.*, 1997b). These K_R values are considerably higher than those encountered in normal sub-surface geological situations, and indicate a high probability of imaging wooden artefact material using an appropriate seismic reflection system.

7.4 *The Mary Rose site: A case study*

7.4.1 *Introduction*

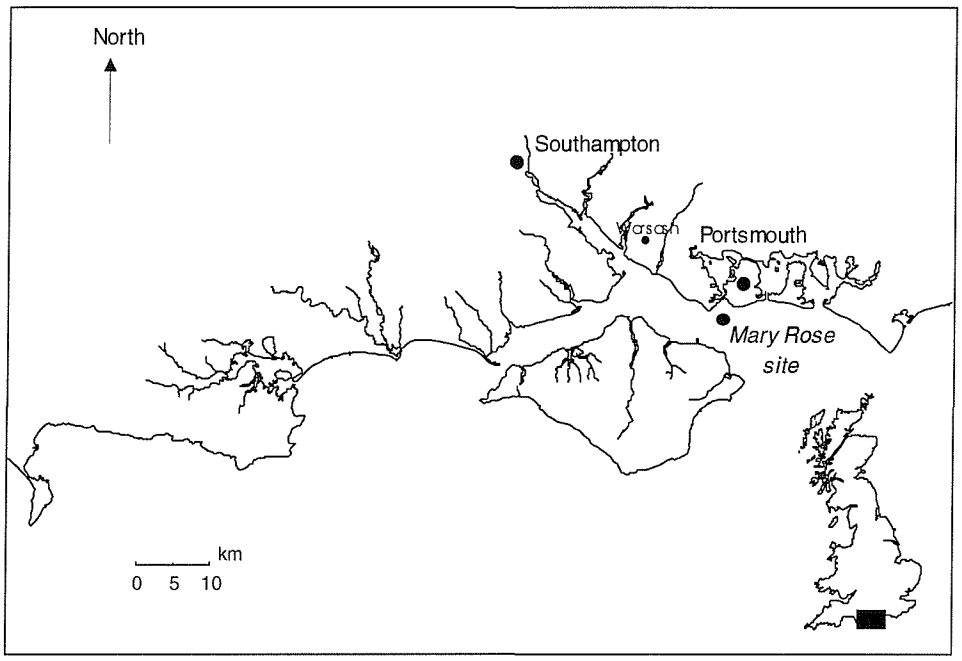

Figure 7.2: Location map of the Mary Rose site located at Spithead, East Solent, UK. The location of the DGPS land receiver station at Warsash is indicated.

The *Mary Rose*, King Henry VIII's flagship, was built in 1509 and subsequently wrecked in the East Solent on 19 July, 1545. The wreck was rediscovered during the late 1960's (Figure 7.2), and site excavation culminated with the raising of the hull remains in 1982. Events leading to the location, excavation and subsequent raising of the *Mary Rose* are well documented (McKee, 1982; Rule, 1982; Dobbs 1995). Today, the raised hull structure is on display in Portsmouth Dockyard, while the *Mary Rose* site itself remains one of 42 sites currently designated under the Protection of Wrecks Act, 1973. Fragments of the wreck remain buried beneath the seabed and the site is frequently monitored by the Mary Rose Trust.

During November 1994 the authors surveyed the excavated *Mary Rose* site using a Chirp sub-bottom profiler. The aims of the survey were to investigate the site for remaining wreck structure, to put the excavated site into a geological context with the advantage of detailed site knowledge supplied by the Mary Rose Trust and to assess the applicability of the Chirp system to marine archaeology.

7.4.2 *Survey equipment and methodology*

The geophysical survey was conducted in November, 1994 aboard SV *Mary Lisa*, using a 2 to 8 kHz swept-frequency Chirp system in an average water depth of 11m. Throughout the survey, a 32 ms pulse length and a system transmit rate of four pulses per second was used in the acquisition of digital sub-bottom data.

A pseudo 3-dimensional survey, of 10m line spacing, was conducted over the site (Figure 7.3), covering an area of approximately 350 x 250 m centred on the excavation hole. Eleven east-west and eighteen north-south lines were traversed, totalling over 6 km of Chirp data. The survey grid was designed to provide close 3-dimensional cover in order to image potential remaining wreck artefacts. Survey navigation, with an accuracy of ±1m was provided by a differential global positioning system (DGPS). For this survey, the land receiver station was located at Warsash (Figure 7.2), within line of site of the survey area.

7.4.3 *Data processing*

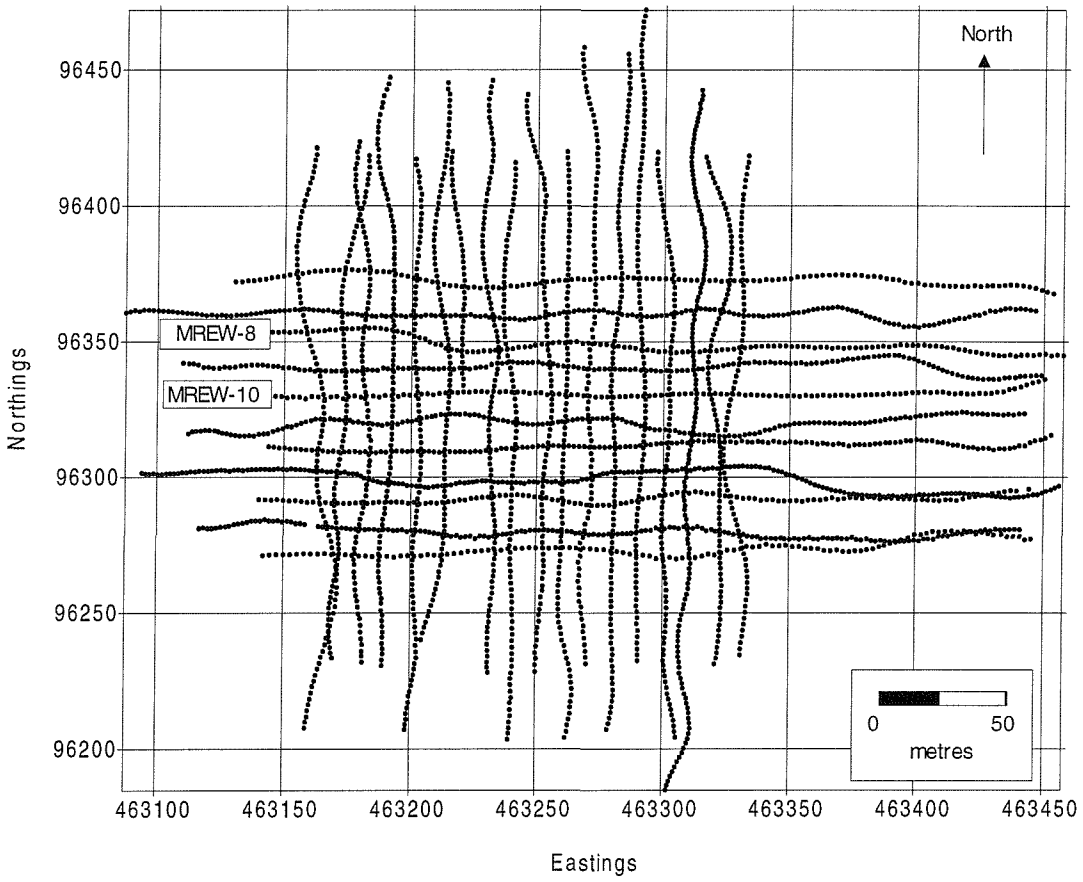

Figure 7.3: Shotpoint map of the 3-dimensional Chirp survey of the Mary Rose site, Spithead, East Solent, UK. The labelled lines are referenced in the text.

The seismic data were correlated with the known 2-8 kHz source sweep in real-time during acquisition. Each survey line was corrected for tidal variations over the survey period, and subsequently converted to ordnance datum. Further processing of the correlated Chirp data

included true amplitude recovery, bandpass filtering, FX deconvolution and the application of a dynamic signal-to-noise filter.

7.4.4 *Results and interpretation*

Examples of two processed sub-bottom profiles are displayed in Figures 7.4 and 7.5. Figure 7.4 is a portion of the east-west Chirp sub-bottom profile MREW-10 showing a cross-section of the present day morphology of the excavation hole. The local geology is characterised by horizontal/sub-horizontal intercalated muds, clays and sands overlying bedrock of varying topography (West, 1980; Adams, 1988).

The most striking feature recognised in the sub-bottom profiles over the entire site is the

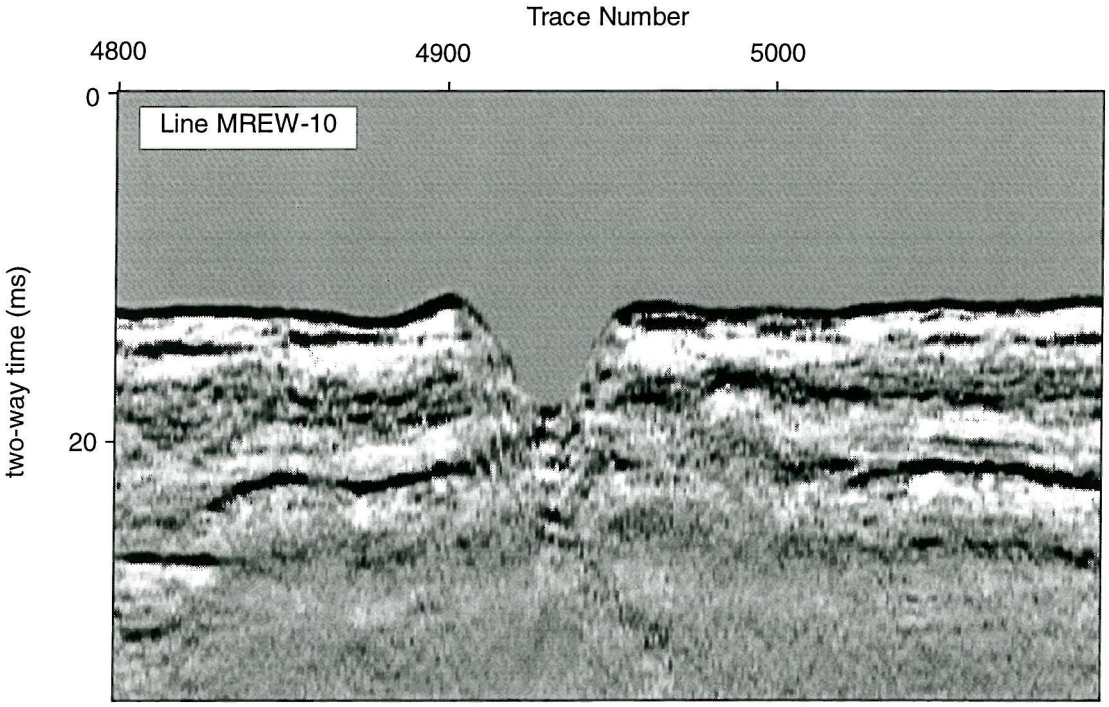

Figure 7.4: Processed portion of east-west orientated Chirp sub-bottom profile (acquired using a GeoAcoustics model 136A towed transducer system) MREW-10 showing a cross-section of the present day morphology of the excavation hole.

discrete "brightspot" (high amplitude reflector) observed in MREW-8 (Figure 7.5). A second such discrete anomalous reflector is observed approximately 30m to the south. These brightspot reflectors are unconformable with the local geology, where the horizontal/sub-horizontal soft-sediment horizons terminate abruptly adjacent to the high-amplitude reflectors. The base of the anomalies form erosive surfaces, clearly post-dating the stratigraphy at this time horizon. Examination of Figure 7.5 indicates the majority of the incident energy is reflected at this horizon, indicating a very high acoustic impedance contrast (K_R of approximately -0.3) between the filling material and the surrounding sediments.

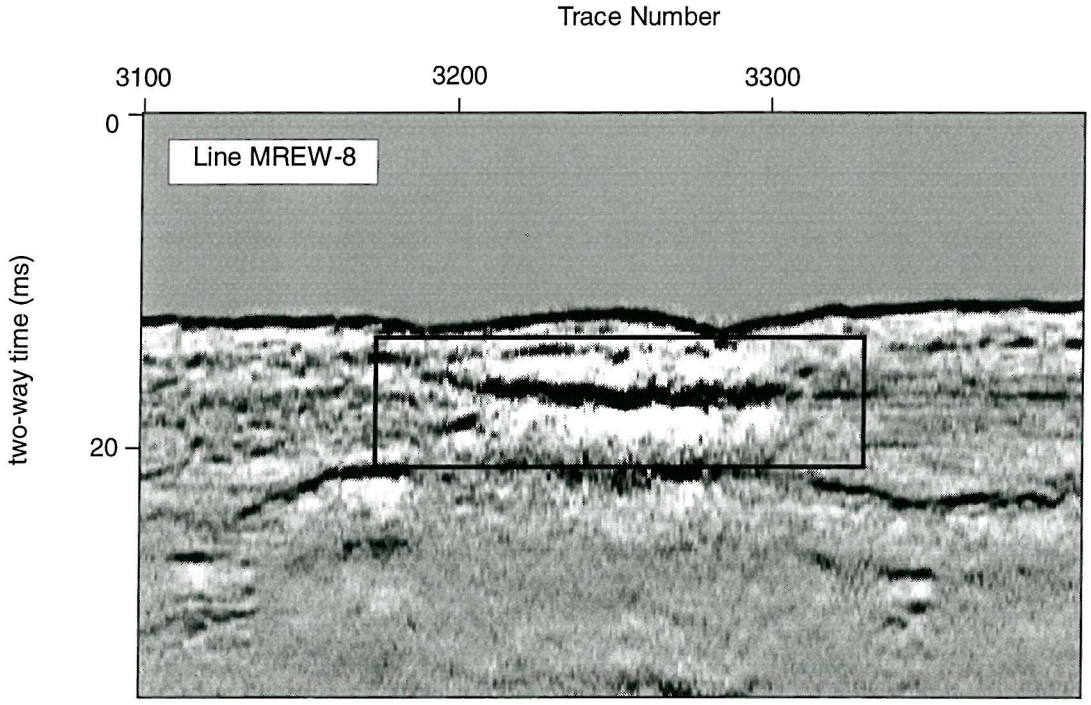

Figure 7.5: Processed portion of the Chirp sub-bottom profile MREW-8, displaying one of the "brightspot" anomalies (highlighted by the black box). The anomaly is characterised by a discrete high amplitude reflector of length 60 m.

In order to examine the spatial relationship between the excavation hole and the brightspots referred to above, 2-dimensional contour maps of the interpreted horizons were produced. The most prominent feature on the seafloor contour plot (Figure 7.6a) is the excavation hole (former position of the *Mary Rose*) located at the centre of the grid, measuring an average of 50 m by 20 m. In order to map the spatial extent of the brightspots, the maximum interpolated amplitude value was extracted from each trace in a 15 to 19 ms time window (thus encompassing the anomalies), normalised and subsequently interpolated across the survey area to produce the contour plot of Figure 7.6b. The resulting contour plot shows two east-west trending sub-parallel anomalies measuring approximately 50m in length, while the northern feature (with a maximum width of 20 m) is on average 5m broader than the southern anomaly. The base of these erosive features varies between 4.5 and 6 m below the seabed, while relief is limited to 1.5 m.

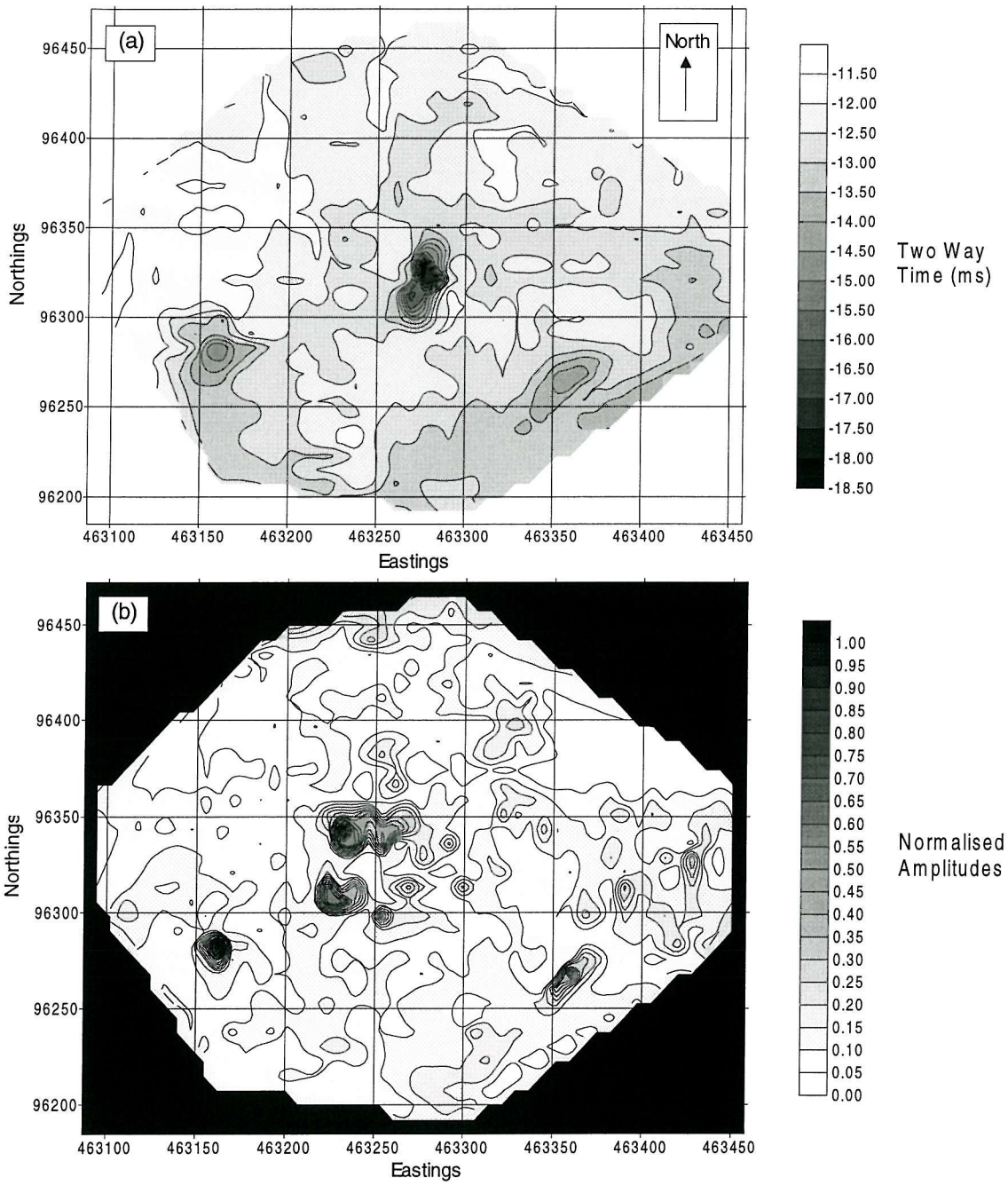

Figure 7.6: (a) A 2-dimensional time contour plot of the seafloor over the Mary Rose site. Topographic lows are shown as black, and highs as light-grey. (b) A 2-dimensional contoured amplitude map of the 15-19 ms time horizon. The normalised amplitude scale is from light-grey (minima) to black (maxima).

Figure 7.7 is a composite map of the *Mary Rose* site, where the position of the excavation hole is overlain on the east-west trending anomalies described above. The present-day peak tidal flow over the site is also indicated. When the *Mary Rose* sank in 1545, the hull lay heeled over on its starboard side in the seabed at an angle of 60° from the vertical (Rule, 1982). The nature of the obstruction the hull presented to easterly and westerly tidal flows was therefore very different. East-west currents passed over and around the irregular surfaces of the castling and decks, while those flowing west to east would have been deflected by the smoother form of the hull (Adams, *pers. comm.*). The authors propose that the anomalies recognised on the western margin of the

excavation hole are the manifestation of palaeo-scour features formed around the wreck of the *Mary Rose* soon after she sank.

Caston (1979) demonstrated that longitudinal wreck marks are shallow (typically 1.5 m to 2 m) relative to their widths and lengths and may be curved near to the wreck but the distal portion is always straight and parallel. This description is consistent with observations from the sub-bottom profiles (where maximum relief on the anomalies is 1.5 m) and the shape of the anomalies in plan view (Figure 7.7). When Figure 7.7 is viewed alongside Figure 7.1, good correlation is noted in the spatial relationship between the anomalies and excavation hole of the *Mary Rose* site, and the scour marks and the position of the wreck in the sonograph. The dimensions and erosive base of the anomalies are also consistent with wreck-associated scour features.

Additional supporting evidence for this interpretation comes from the morphology of the wreck marks in relation to the seabed lithology over the site. Caston (1979) states that wreck mark morphology is dependent upon seabed lithology, where scour features formed on sandy floors

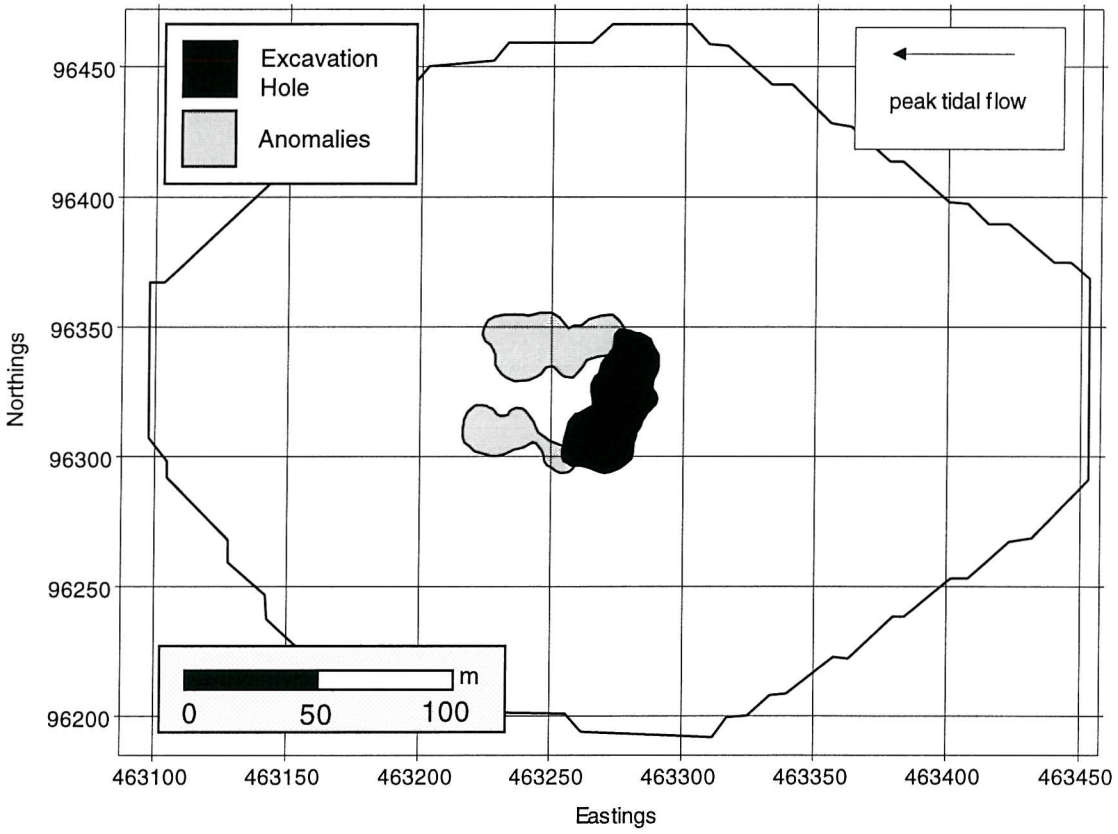

Figure 7.7: Composite map of the Mary Rose site displaying the position of the excavation hole (black) overlain on the spatial extent of the anomalies (grey) from Figure 7.6.

around wrecks consist of longitudinally extensive, broad, shallow troughs as opposed to narrower, deeper and less extensive features on gravel floors. The outline of the interpreted wreck marks on Figure 7.7 indicate these scour features are broad in comparison to the dimensions of the excavation hole. Belderson *et. al* (1982) demonstrated that wreck marks form in sandy substrates where mean near-surface peak spring tide range exceeds 75 cms^{-1}. The Tudor seabed on the *Mary Rose* site was a mix of clays and sands (Adams, *pers. comm.*) and the present day near-surface peak spring tide range is 80 cms^{-1} - a tidal range sufficient to scour wreck marks on the Tudor seabed. Assuming tidal strengths in this region have not changed appreciably over the past

450 years, a suitable tidal regime would have existed around the *Mary Rose* site, at the time of sinking, to produce longitudinal scour patterns. Furthermore, present day peak tidal current flow across the site is from east to west (275 to 279°, *Mary Rose* Trust *pers. comm.*). The geometry of the interpreted palaeo-scour features in relation to the former position of the wreck indicate that palaeo-current directions in Tudor times were broadly in the same orientation as the present day, indicating the regional tidal regime of the East Solent has not changed appreciably in the past 450 years.

The presence of these longitudinal scour features is previously unrecognised on the *Mary Rose* site. Large segments of the hull superstructure and the stern and bowcastles of the wreck eroded subsequent to sinking. The authors propose that a portion of this material survives as wreck fragments in the scour pits to the west of the excavation. In the years after sinking, the hull structure standing above the seabed in the water column gradually eroded and collapsed, so constituting progressively less of an obstruction to tidal flow (Rule, 1982). Hence, any depressions caused by the scouring action gradually filled in, sealing and preserving any timber elements and other objects deposited within. The resulting fill in the scour pits is therefore a stratigraphic record of this interrelated process and indicates a direct relationship between the morphology of the seabed obstruction and its associated scour features. Furthermore, the authors propose that the strong reflection from the interpreted wreck marks is due to the contrast between the fill material (a combination of oak wreck fragments and coarse grained sedimentary material deposited within these pits due to preferential deposition in topographic lows on the seabed) and the surrounding unconsolidated sediments.

7.5 *Conclusions and discussion*

The Chirp profiling technique has proven itself as a rapid, non-invasive investigative technique for buried archaeological sites, thus broadening the scope of the application of geophysics to marine archaeology. Rather than merely providing a technique for locating sites, high-resolution data acquired by Chirp sources can provide information regarding the nature and chronology of degradation of wreck-sites, and is therefore of particular utility in the protection and management of submerged archaeological material.

The Chirp profiles of the excavated *Mary Rose* site have imaged structures previously unrecognised on site, interpreted as infilled longitudinal scour features associated with the sinking and subsequent degradation of the *Mary Rose*. The fill material is believed to consist of wreck fragments and coarse sediment material preferentially deposited on the port side of the ship in scour hollows. These proposals indicate the authors' belief that the *Mary Rose* site has had a highly variable depositional history, ranging locally from a highly dynamic erosive environment subsequent to the initial wrecking, followed by a period of relatively high deposition rates in the scour pits once the wreck structure had degraded to a level concordant to the seabed, to a more quiescent period subsequent to the deposition of a "hard shelly layer" which sealed the Tudor levels (Rule, 1982).

Recognition and preservation of longitudinal palaeo-scour features has important implications. Information regarding the degradation and preservation of a wreck may be gleaned

from the morphology and content of these material traps. The dimensions of the infilled scour hollows indicate these features may be more easily recognisable on sub-bottom profiles than partially degraded wrecks. In extreme cases, where a wooden wreck is so completely degraded that the majority of the superstructure is fragmented, the wreck may not provide the concentration of coherent material required to produce a strong reflection, but material in scour pits may.

For the marine geologist, the identification of palaeo-scour marks associated with anthropogenic marine features (not only wrecks) can provide a useful tool in interpreting palaeo-current directions.

Chapter 8

The *Invincible* (1758) site - an integrated geophysical assessment[1]

8.1 *Introduction*

Invincible (originally *L'Invincible*), a 74 gun 3rd rate, was built at Rochefort, France in 1744, captured by the British in 1747 and subsequently lost off Portsmouth, in February 1758. The history of *Invincible* is well documented (Bingeman, 1981 and 1985; Lavery, 1988); her importance lies in the fact that at the time she was regarded as the finest 3rd rate and was used as the design basis for a whole new generation of ship (Bingeman, 1981). The location of *Invincible* was rediscovered in 1979 by Arthur Mack on Horsetail, East Solent, UK (50^0 44.34' N., 01^0 02.23' W. - Figure 8.1a). In September 1980, the Secretary of State designated the site under the Protection of Wrecks Act 1973 (1980 No. 2, 1980/1307). Subsequently an excavation licence was issued and the wreck has been the subject of an ongoing programme of excavation and survey since then. Figure 8.1b shows the results of diver investigations (with diver interpretation) of the site between 1983 and 1987. When inspected in March 1758, the wreck of *Invincible* was lying on her port side at an angle of about 30^o from vertical (Lavery, 1988: 104). Diver excavations conducted between 1984 and 1996 indicate the wreck is currently lying at an angle of approximately 45^o at her bow, 15^o at her stern and 30^o from vertical at midships (Bingeman, *pers. comm.*).

Today, the wreck of *Invincible* lies in an average water depth of 8 m, with surface currents over the Protected Area orientated northwest-southeast (Tidal Diamond E, 50^o 43.7' N; 01^o 03.8' W). Transverse bedforms interpreted from side-scan sonar data acquired over the site are aligned northeast-southwest, suggesting that prevalent bottom currents are orientated northwest-southeast, coincident with surface currents. Sediment analysis from the site reveals that the substrate comprises well-sorted, fine-grained (2.25-2.47ϕ) quartzose sands.

Two geophysical surveys were conducted over the *Invincible* site, on 26, May 1995 and 10, August 1997 (Figure 8.1c). The rationale was to investigate the processes of site formation, the change in the wreck site over the survey period of 26 months and to examine the effectiveness of marine geophysical surveying for archaeological site-monitoring. The following sections relay the results of this survey, propose a wrecking history for the site and discuss the potential use of geophysics as a management tool for the maritime archaeological resource.

[1] Quinn, R., Adams, J.R., Dix, J.K. and Bull, J.M., *International Journal of Nautical Archaeology*, in press.

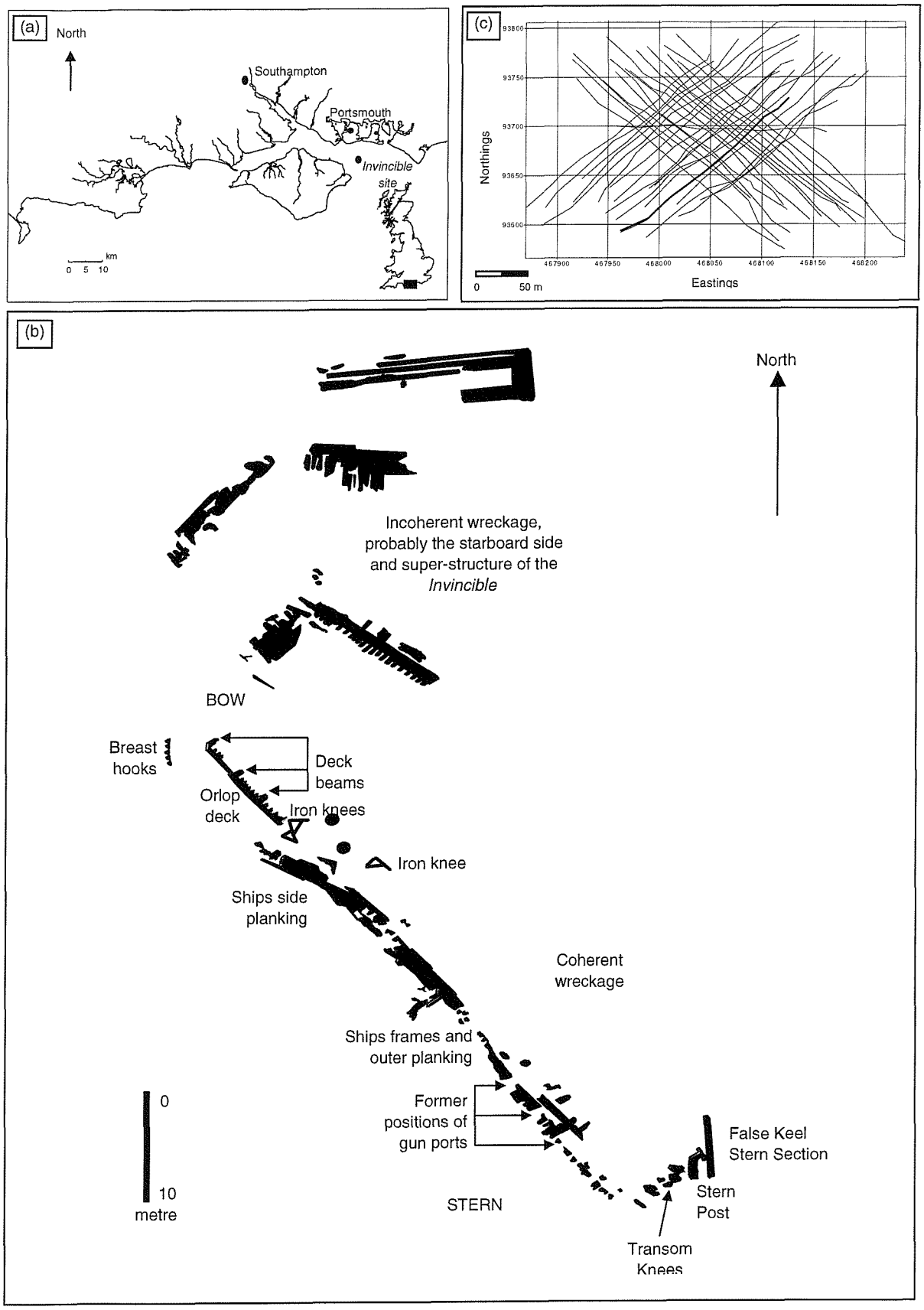

Figure 8.1: (a) Location map of the Invincible site, Horsetail, East Solent, UK. (b) Detailed plans of the Invincible (1758) wreck-site from 1984-1987, with diver interpretation (after Lavery, 1988). (c) Trackplot of the geophysical surveys conducted over the Invincible site; the 1995 and 1997 surveys utilised the same survey grid. The survey track highlighted by the heavy line corresponds to the geophysical data presented in the text.

8.2 *Survey equipment and methodology*

High-resolution sub-bottom geophysical surveys were conducted utilising a GeoAcoustics 2 to 8 kHz swept frequency Chirp sub-bottom profiling system (Figure 8.2). Throughout the surveys, a 32 ms pulse length and a system transmit rate of four pulses per second was used in the acquisition of digital sub-bottom data. The 1995 side-scan sonar survey utilised a 100 kHz digital side-scan system with a transmit rate of 4 pulses per second and the 1997 side-scan survey utilised a 500 kHz source (to provide higher resolution data), with a transmit rate of 10 pulses per second. Survey navigation was provided by a differential global positioning system (DGPS), with an accuracy of ± 1m. An area of 350 x 250 m was surveyed, centred on the site of *Invincible*. A total of 8 km of digital sub-bottom and side-scan data were acquired over the 2 surveys (Figure 8.1c).

Seismic-sections of the wreck-site were acquired at 10 m spacing using the Chirp profiler, while plan images of *Invincible* and the surrounding seabed were provided by the side-scan sonar. The geophysical instrumentation was deployed in co-registration mode, *i.e.* using coincident Chirp and side-scan pulse triggering to ensure the same portion of the wreck structure was imaged simultaneously during surveys. This survey methodology ensured that full 3-dimensional coverage of the wreck was obtained. Furthermore, a 4th dimension (time) was added by repeating the survey over a 26 month period.

Inherent in side-scan data of the sea-floor is a spatial distortion due to towfish altitude. This means that the initial return to the transceiver mounted on the towfish is almost vertical, and the returns from a distance are almost horizontal. Each data point in between has some lateral (or range) distortion (Fish and Carr, 1990). In order to correct for this lateral distortion, a slant range correction can be applied to side-scan sonographs to produce a laterally consistent interpretation of the seafloor.

Side-scan sonar data is in effect a tonal map of the seafloor. Dark areas on the sonograph indicate strong acoustic returns (and conversely light tones indicate weak returns), where the strength of the return is a function of material type and seafloor topography. Coarse sedimentary material and wood provides strong returns, while relatively fine-grained sediment returns weaker signals. Likewise, sub-bottom data recorded by the Chirp system is affected by the physical characteristics of the material causing the reflection of the transmitted pulse. Exposed or buried wooden artefacts present a high acoustic impedance contrast with surrounding unconsolidated sediments (Quinn *et al.*, 1997b), and so appear as strong (high-amplitude) reflectors on the sub-bottom profiles.

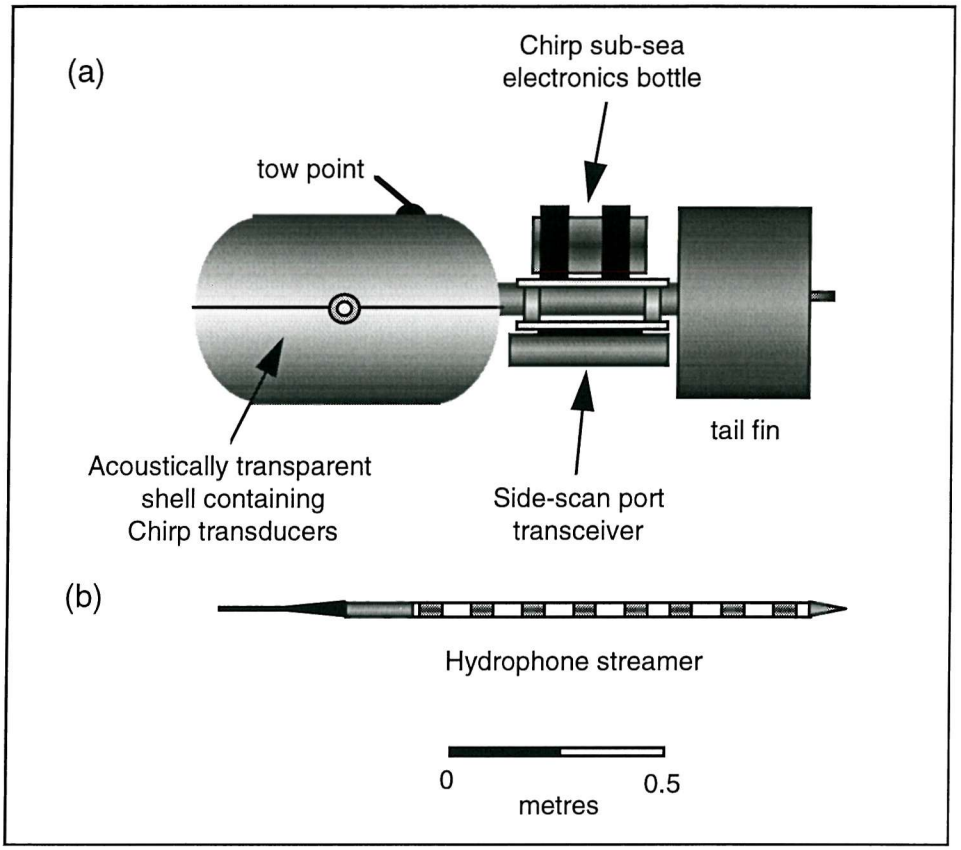

Figure 8.2: Diagram illustrating the combined Chirp and digital side-scan deployment configuration: (a) GeoAcoustics Model 136A towfish (b) 8-section neutrally buoyant hydrophone streamer. Throughout the survey, the sub-sea electronics bottles and side-scan transceivers are mounted on the towfish and the Chirp hydrophone is towed directly from the rear of the towfish.

8.3 *Results*

The results of the geophysical surveys are presented in the following three diagrams, and discussed in detail in the *Interpretation* section below. Figure 8.3 (a-d) is a composite image of the *Invincible* wreck site. Figures 8.3a and 8.3b show the results of the 1995 side scan and Chirp sub-bottom survey of the wreck-site. In the sonograph shown in Figure 8.3 (a), the port side is almost completely exposed, whilst the majority of the north-eastern portion of the wreck material is covered by a thin veneer of sand (average thickness of 0.75 m), evident in the Chirp sub-bottom profile of Figure 8.3b. Figure 8.3c is an enlarged, filtered portion of 8.3b, where the buried oak wreck structure is imaged as a high-amplitude reflector. An idealised midship section of the *Invincible* (after Lavery, 1988 - scaled to correspond to the Chirp profile), lying on her port side at an angle of 30° to vertical, is displayed in Figure 8.3d. A reflection coefficient (a measure of the strength of reflection) of -0.27 is calculated for the oak reflector (Bull *et al.*, in review). This large, negative reflection is diagnostic of buried wooden artefacts in the marine environment as identified from theoretical and experimental work (Quinn *et al.*, 1997b).

Figure 8.4 displays the results of the 1995 side-scan survey of the wreck-site. Figure 8.4a is the sonograph of the wreck, and 8.4b is the interpreted isometric plot (subsequent to slant-range correction) of the wreck-structure. Figure 8.5 displays the corresponding sonograph and isometric plot from the 1997 survey.

8.4 *Interpretation*

8.4.1 *Site formation processes*

Comparisons between the idealised midship section of *Invincible* (Figure 8.3d) and the sub-bottom profile in Figure 8.3c indicates that the extent of exposed and buried wreck structure imaged in the Chirp profile exceeds the maximum width of the vessel lying on her side at an angle of 30° to vertical (15 m), by more than 15 m at this position (*i.e.* a total width of 30 m at this point). Examination of the side-scan and sub-bottom data acquired over the whole of the wreck-site indicates that additional wreck structure to that outlined on the diver's plans is located to the north and north-east of what is labelled coherent wreck structure in Figure 8.1 (the port side of the ship). Evidence from the isometric plots in Figures 8.4 and 8.5 indicates that the majority of this additional wreck structure is structurally coherent, comprising a series of parallel and sub-parallel reflectors in the side-scan images.

Tidal data over the site (Tidal Diamond E) shows that the predominant tidal flow over the site is in the direction 311° (see rose diagram (a) in Figure 8.6), indicating the net material transport direction over the site is in a north-westerly direction. This does not explain the distribution of the fragmented wreck structure lying to the North and north-east of the coherent wreckage.

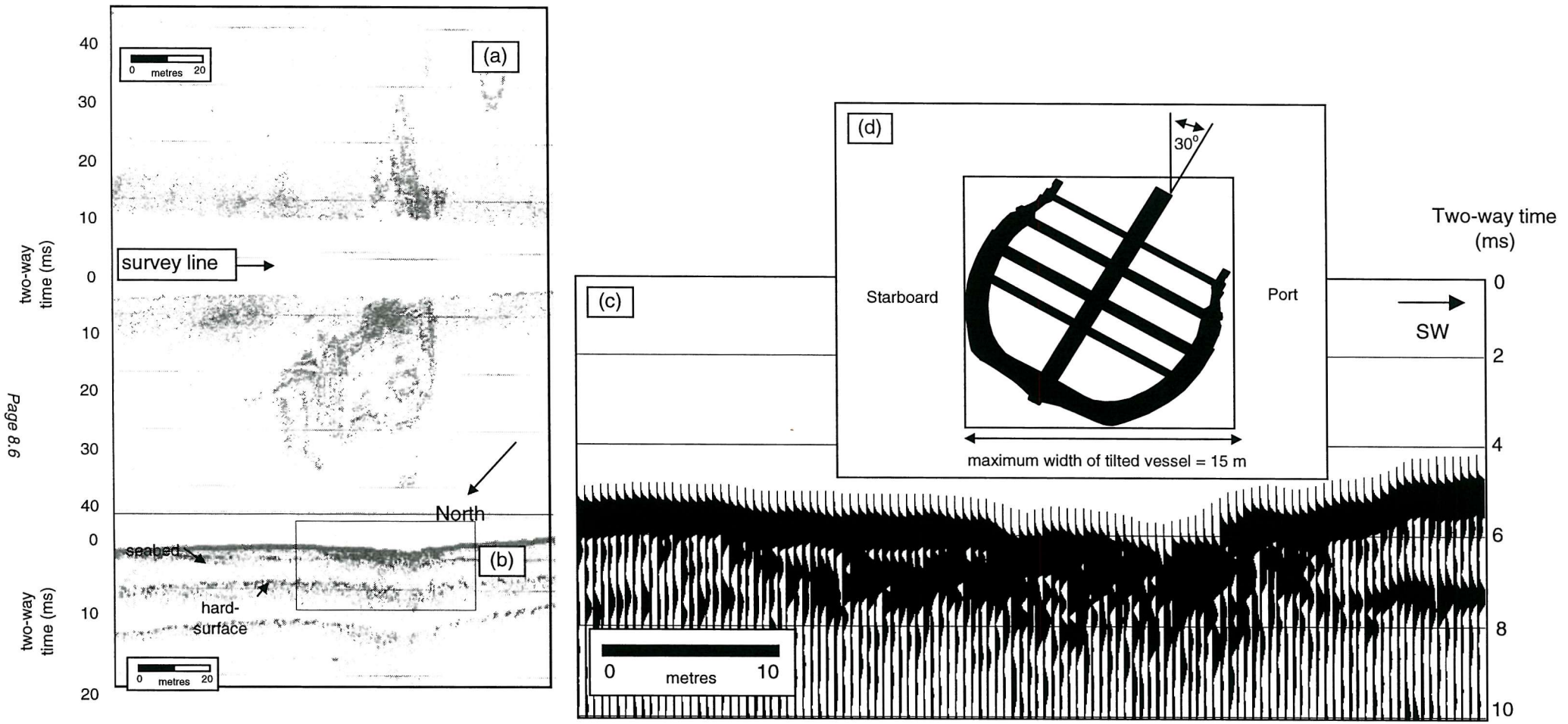

Figure 8.3: Composite image of the *Invincible* wreck-site: (a) 100 kHz side-scan sonograph of the wreck-site acquired in May 1995; (b) corresponding Chirp sub-bottom profile displaying a NE-SW orientated cross-section of the wreck-site; (c) enlarged band-pass filtered portion of (b); (d) idealised midship section of the *Invincible* (after Lavery, 1988) tilted at an angle of 30^0 from the vertical.

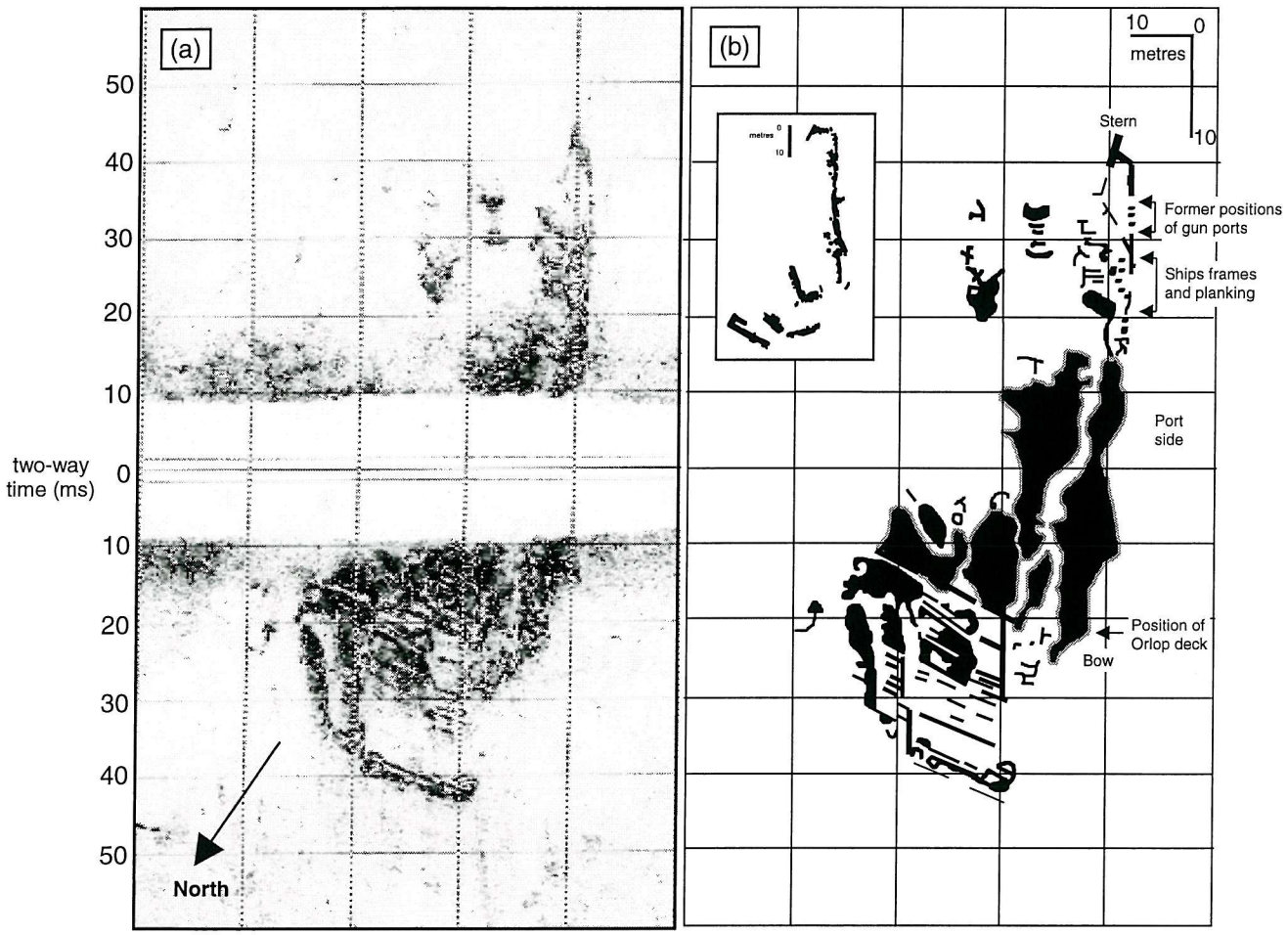

Figure 8.4: (a) Sidescan sonograph of the *Invincible* site acquired in May 1995; (b) corresponding isometric plot of the site, subsequent to slant-range correction. Diver's plans (after Lavery, 1988) are shown in the isometric plot for comparison.

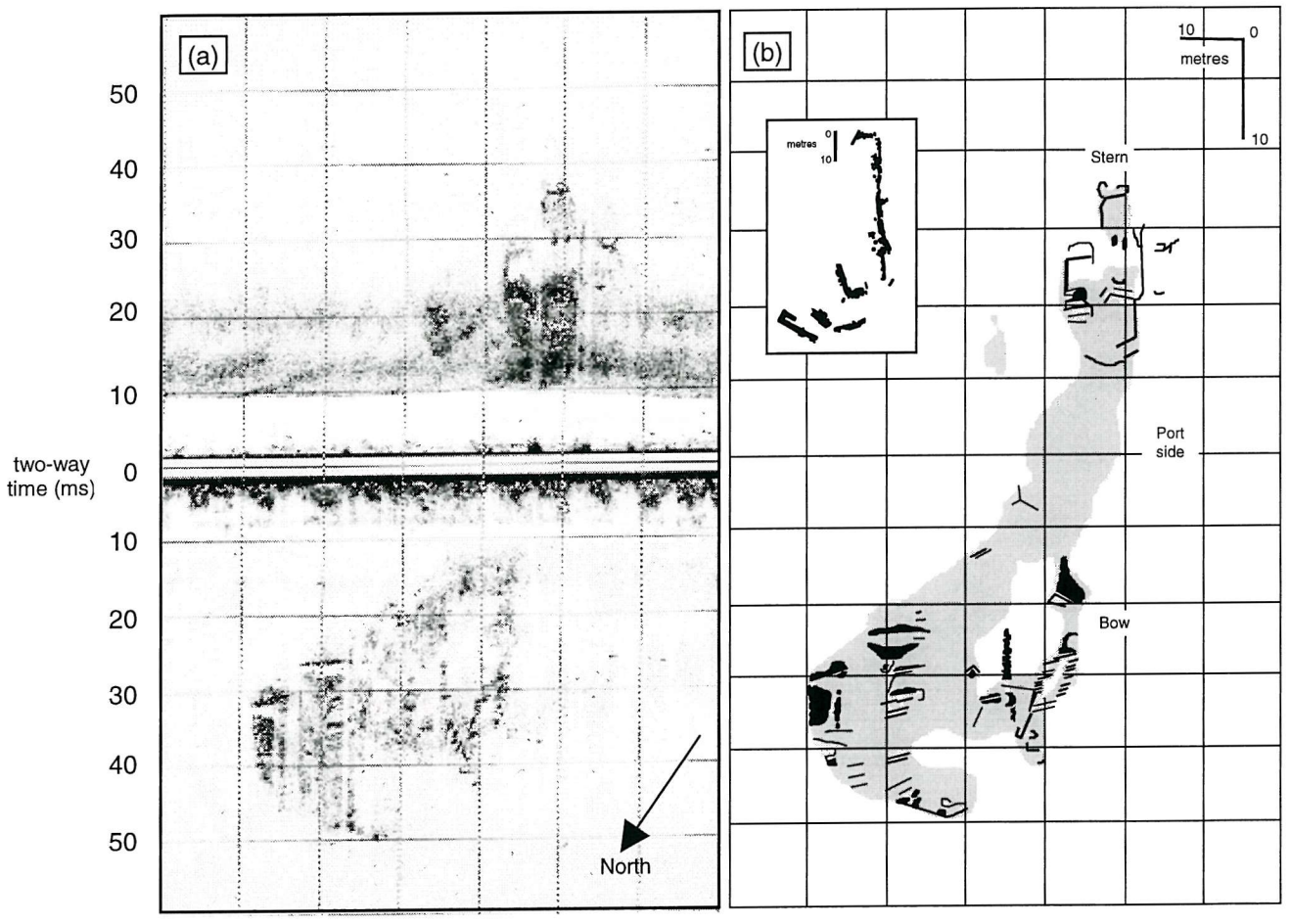

Figure 8.5: (a) Sidescan sonograph of the *Invincible* site acquired in May 1997; (b) corresponding isometric plot of the site, subsequent to slant-range correction. Diver's plans (after Lavery, 1988) are shown in the isometric plot for comparison.

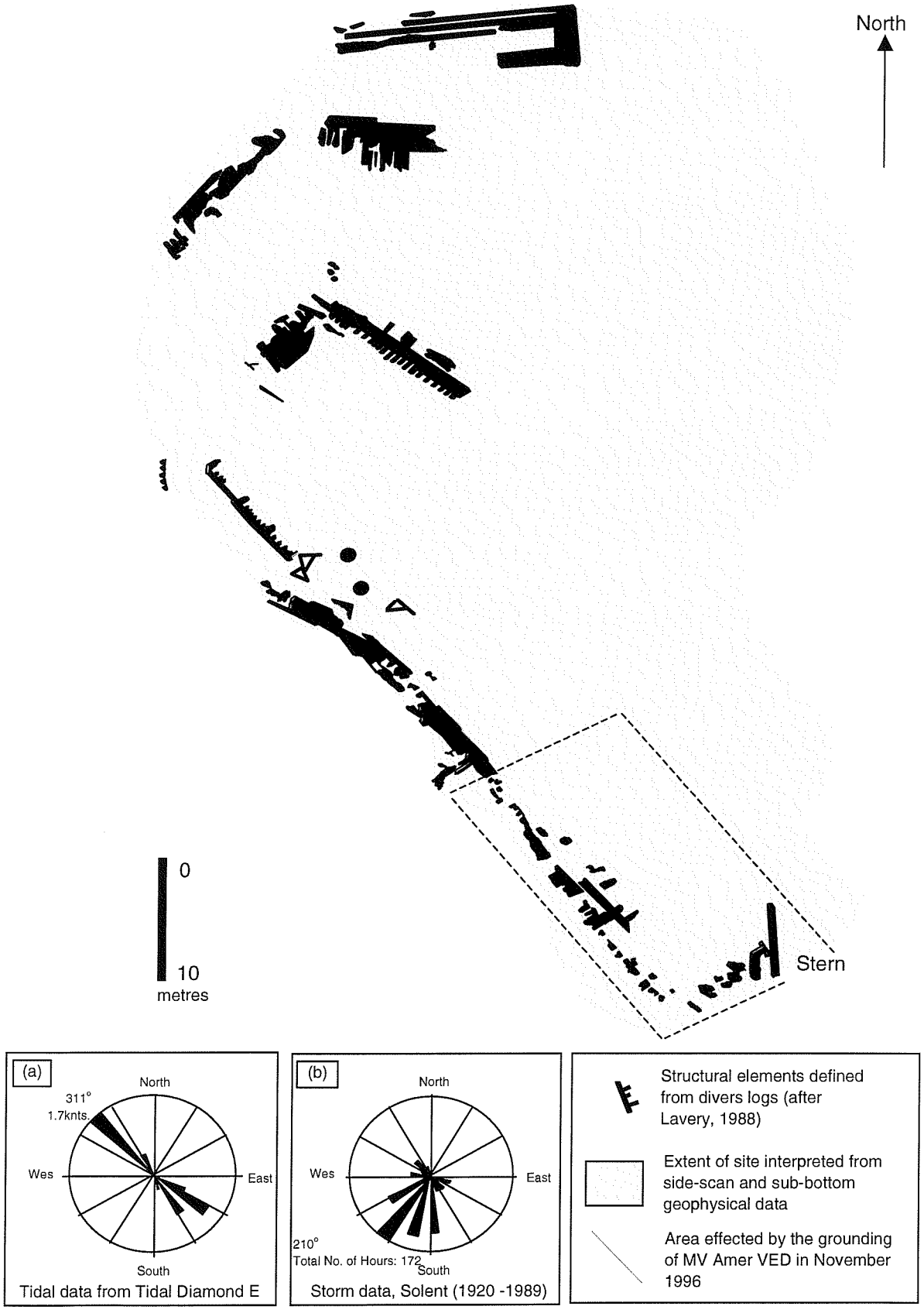

Figure 8.6: Synthesis diagram of the Invincible (1758) wreck-site including diver's plans (after Lavery, 1988), extent of the wreck site (from geophysical surveys), principle area of damage caused by the grounding of MV Amer VED within the Protected area and rose diagrams indicating (a) prevalent tides and (b) storm forces acting on the site.

However, storm data from the Solent over the past 70 years (see rose diagram (b) in Figure 8.6) reveals that more than 90% of storm events of Force 8 or higher were south and south-westerlies (Peace, *in press*), i.e. dominant storm wave action in the Solent acts in a north and north-easterly direction.

The *Invincible* wreck site lies in an average water depth of 8 m, a depth at which wave action due to heavy storm events would significantly affect a structure lying on and above the seabed. Figure 8.6 is a synthesis diagram in which the original diver's plans of the site are indicated, together with the extent of site interpreted from the geophysical records. It is proposed that the formation of the wreck-site has been dominated by destructive storm forces, rather than the more quiescent tidal forces acting on site.

These site formation processes operating on the *Invincible* site are in direct contrast to those proposed by the authors for the nearby *Mary Rose* wreck site (Quinn *et al.*, 1997c). The *Mary Rose* site lies in an average water depth of 12 m, a depth at which the effects of storm events is less noticeable. Whereas *Invincible* was a far larger vessel part of which remained above the surface after grounding, the *Mary Rose* hull was completely submerged. The *Mary Rose* also impacted several metres into the seabed, further reducing wave effect (Rule, 1982: 45; Quinn *et al.*, 1997c). Evidence that the *Mary Rose* hull structure still stood fairly high in the water column for many years is provided by the Elizabethan Admiral Sir William Monsom who reported being able to see her timbers (Rule, 1982: 41).

The historical account of the protracted struggle to refloat the *Invincible* after grounding states the ship had dug a bed for itself in the sandbank and was afloat except at low water (Lavery, 1988: 102). Then on the 22nd of February, the third day after striking the bank, the ship heeled violently breaking many timbers (Lavery, 1988: 102). When inspected in May 1758, she was described as "greatly twisted, waiving and cambered". It was concluded that the ship was 'bilged' and beyond recovery (Lavery, 1988: 104). It is hardly surprising that the hull should have taken a heavy battering during this period. Even before the capsize, water was already deep in the hold and it is possible the shingle ballast had shifted. Subsequent archaeological work established that *Invincible* had broken her back.

Once heeled over, the decks were exposed to the force of the prevailing seas. Sediment would have begun accumulating rapidly in the hull, further adding to the stress imposed on the structure. The reference to 'twisting' and 'waiving' is significant. With the lower hull held firm in the seabed by the weight of ballast and sediment, the starboard side would have taken the full force of storm-induced wave action, effectively levering it open. Once the starboard side had been torn away, the port side appears to have further subsided, possibly exacerbated by scour action, reaching the angle of heel observed during excavation.

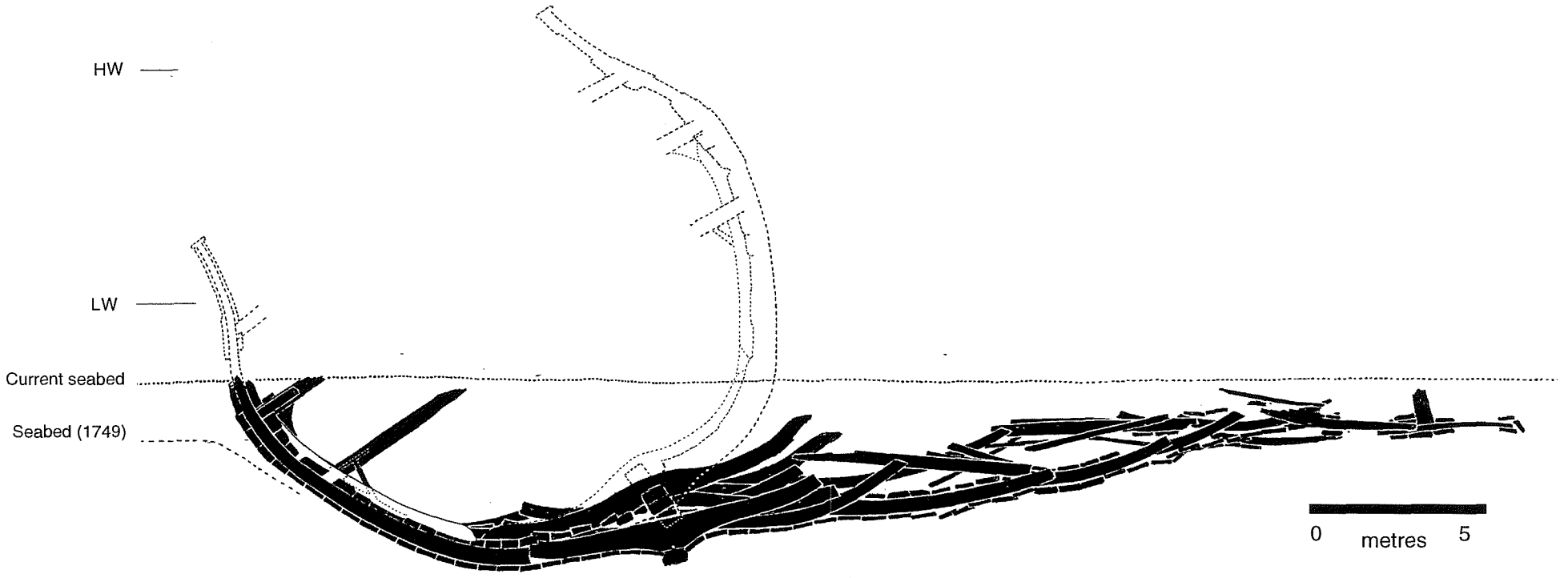

Figure 8.7: Midship section based on the *Triumph*, an exact copy of *Invincible*, where HW and LW indicate mean high and low water springs. The depth to the seabed in 1749 is estimated from contemporary descriptions (Lavery, 1988), and 'Current seabed' is an estimated mean relative to the surviving structure monitored during the excavations and survey (Illustration: Jon Adams).

The evidence therefore indicates that the *Invincible's* hull progressively hinged open, failing along the lines of weakness, presumably the alignments of futtock joints and beam scarfs. As the prevailing storm direction is from the SW the structure would tend to collapse outwards. This is supported by a probe survey carried out in 1990 that made several shallow, firm contacts up to 26m east of the port side structure (Bingeman, 1990: 5). Figure 8.7 shows a schematic midship section similar to *Invincible*, summarising the proposed wrecking process. The angle of heel is an estimated mean between the 46° measured at the bow and 15° at the sternpost. The authors propose that the continuous strong reflector in the sonagraphs is in fact largely coherent wreckage of the starboard side (Figure 8.7), lying at a low angle on the hard-surface imaged in the Chirp profile (Figure 8.3 (c)).

8.4.2 *Environmental impact*

In 1991, a sewage outfall was constructed 1,300 m to the west of the wreck-site. Tidal currents within the East Solent result in sewage being consistently swept over the Protected Area, presenting a hostile environment for diving archaeologists. Furthermore, on 19 November, 1996, MV *Amer* VED dragged her anchor and went aground within the *Invincible* Protected Area (Bingeman, 1996). The merchant vessel carried away the wreck buoy marking the site and was floated off later that night.

The development of transverse bedforms (interpreted from side-scan sonar data), along with diver observation (Lavery, 1988: 108), indicate the sandy substrate over the *Invincible* site is mobile, alternatively exposing and covering sections of the wreck structure with time. This is supported by evidence from side-scan data (Figures 8.4 and 8.5), indicating that overall exposure of the wreck was greater in May 1995 than in August 1997. However, the length of acoustic shadows in the 1997 sonographs indicate that the seabed level in the northern portion of the wreck-site was lower in August 1997, exposing proportionally more of the timbers at this position to environmental disturbance.

Comparisons between the two vintages of side scan data (Figures 8.4 and 8.5) indicate the stern section of the wreck-site has been affected by the grounding of MV *Amer* VED within the Protected Area on 19th November 1996. Diver inspection in December 1996 and April 1997 concluded that substantial damaged was caused to the wreck site by the merchant vessel over a distance of at least 20 m to her port side and stern quarter (Bingeman, 1996). These findings are consistent with interpretation of the side scan traces. The false keel section and sternpost, which are clearly imaged in the 1995 side scan data (Figure 8.4), are absent in the 1997 data (Figure 8.5). Furthermore, the stern section and port side of the wreck in the 1997 data are less structurally complex than the corresponding section in the 1995 sonograph, indicating overall structural degradation to this portion of the wreck (confirmed by diver observation, Bingeman, 1996).

8.5 *Discussion*

The interpretation of marine high-resolution seismic reflection and side-scan sonar data, in conjunction with local meteorological data, have culminated in a wrecking history of *Invincible*. It is proposed that the arrangement of the wreck-site was primarily controlled by south-westerly storm forces acting over the site. Distribution of wreck material was constrained by storm-associated wave action in a north-easterly orientation, which deposited the bulk of fragmented wreck structure to the north and north-east of the *in-situ* port side.

The proximity of the sewage outfall and shipping channels close to the wreck-site make it a hazardous site for diver investigation. Marine geophysical techniques are particularly suited to hostile environments, such as areas where marine pollution, poor visibility and other anthropogenic hazards can significantly affect the performance of the diving archaeologist. The high correlation between the seismic reflection data, the historical sources and archaeological observation demonstrates the integrated geophysical approach adopted here is an efficient, non-intrusive investigative technique. The differences seen in the 1995 and 1997 datasets also demonstrate it is an effective strategy for the monitoring of archaeological sites, whether hazardous or not.

Of particular relevance to management is the ability of current geophysical techniques to demonstrate the true areal extent of a site. In the surveys of both the *Mary Rose* (Quinn *et al.*, 1997b) and of *Invincible*, geophysical survey has shown the extent of the site to be greater than was apparent through direct observation. Although the respective project staff knew the sites extended beyond the areas investigated during excavation and recording, this was difficult to quantify. Enhanced ability to define the extent of an archaeological site has implications for site management, for example in determining the appropriate size of a protected area around those historic wrecks designated under the Protection of Wrecks Act 1973.

Increasing emphasis is being placed on national and regional initiatives designed to quantify the submerged archaeological resource and compile Sites and Monuments Records (Ferrari, 1995; English Heritage, 1996). A key element of their rationale is their active role in heritage management, particularly in archaeological assessment, site monitoring, and the identification of threat. In this light, repeated 3-dimensional (Chirp and side scan) surveys over archaeologically sensitive areas in the proximal coastal zone offer a highly effective strategy for managing the marine archaeological resource.

Chapter 9

Discussion and conclusions

9.1 Conclusions

The main conclusions are grouped below under their respective Chapter titles:

9.1.1 *The effective resolution of Chirp sources:*

(a) The limits of vertical resolution (R_v) of Chirp sources are defined by:

$$\frac{2}{\Delta f} \geq R_V \geq \frac{1}{\Delta f},$$

where Δf is the bandwidth of the transmitted signal.

(b) The limits of horizontal resolution (R_h) of Chirp sources are defined by:

$$\frac{V_p twt}{2} \tan\frac{\theta_d}{2} \geq R_h \geq \frac{V_p}{2}\sqrt{\frac{twt}{f_d}},$$

where V_p is the compressional wave velocity of the material above the reflector, twt the two-way travel time to the reflector and θ_d the beam-angle of the Chirp source associated with the dominant frequency component, f_d.

9.1.2 *Optimal processing of Chirp data*

Processing of uncorrelated Chirp data is facilitated by knowledge of the Chirp source-signature:

(a) Effective deterministic deconvolution is accomplished by designing an inverse filter based on the Chirp Klauder wavelet.

(b) Interpretability of Chirp sub-bottom data is aided by the calculation of the instantaneous amplitude.

(c) SNR and reflector continuity are enhanced by the application of predictive filters: FX-deconvolution, dynamic S/N filter and dipscan stack.

(d) An improvement of greater than 60 dB in SNR on the uncorrelated data is obtained by correlating the sub-bottom data with the source-signature.

9.1.3 *Imaging wooden artefacts utilising Chirp sources*

(a) The anisotropy of wood decreases with increasing density. Compressional wave velocities parallel to the wood grain (V_L) are faster than those across the grain (V_R and V_T).

(b) Experimental work on wood samples from a 16th Century oak wreck indicate that burial in marine sediments cause changes in the physical properties of the outer few centimetres of wood samples, leading to isotropy of compressional wave velocities. Inner wood is unaffected by burial.

(c) Theoretical reflection coefficients calculated for wood buried in unconsolidated marine sediments are typically large and negative.

(d) Theoretical reflection coefficients of oak (historically the most common construction material in British-built pre-19th Century boats) range from -0.03 to -0.64.

(e) Variations in reflection coefficients of wood buried in unconsolidated marine sediments are dependent upon wood species, sediment-type, exposure histories and the orientation of the incident compressional wave.

(f) Reflection seismology using Chirp sources can readily image buried wooden artefacts. The success of the method is primarily dependent upon the resolution of the profiling system and the size and structural coherency of the target.

9.1.4 *The calculation of reflection coefficients from correlated Chirp data*

(a) Reflection coefficients are calculated from Chirp sub-bottom data using amplitude-time relationships from single traces and polarity information from trace mixing.

(b) The average reflection coefficient calculated from an oak wreck (The *Invincible*) buried in unconsolidated marine sediments (K_R = -0.26) agrees with theoretical and experimental predictions (K_R = -0.03 to -0.64). Errors involved in the calculation of reflection coefficients from Chirp data suggest the results may be underestimated by a maximum of 40%.

(c) Small changes in the seafloor impedance profile, related to variable surficial sediment thickness and the presence of seafloor transition zones, causes random polarity changes in the Chirp pulse.

9.1.5 *Case Study I: The* Mary Rose *wreck-site*

Chirp profiles of the excavated *Mary Rose* site have imaged structures previously unrecognised on site, interpreted as infilled longitudinal scours features associated with the wrecking and subsequent degradation of the hull structure. Fill material is believed to comprise wreck fragments and coarse grained sedimentary material (probably ships ballast) preferentially deposited in scour hollows on the port side of the wreck.

9.1.6 *Case Study II: The* Invincible *(1758) wreck-site*

Distribution of wreck material on the *Invincible* site is constrained by storm associated wave action in a north-easterly orientation, depositing the bulk of fragmented wreck structure to the north and north-east of the *in-situ* port side. Evidence suggests that current site stability is controlled by a combination of tidally induced currents and anthropogenic activity.

9.1.7 *General conclusions*

(a) In terms of resolution, data quality and flexibility, Chirp profilers currently offer the most appropriate geophysical technology for the investigation of buried archaeological material.

(b) Combined Chirp and side-scan sonar data acquisition, together with systematic survey methodologies, can provide a suite of data for the investigation of submerged archaeological sites.

(c) The acquisition of digital data facilitates quantitative analysis of marine archaeological sites, enabling the calculation of reflection coefficients to classify buried material and the spatial and quantitative mapping of buried archaeological material through amplitude mapping.

9.2 Discussion

The Chirp profiling technique has proven itself as a rapid, inexpensive, non-invasive investigative technique for sites of archaeological significance. Marine seismic reflection techniques are particularly suited to hostile environments such as areas where marine pollution and poor visibility have adverse effects on the performance of the diving archaeologist. Information regarding wrecking history and site formation processes can be interpreted from detailed and systematic surveys.

4-dimensional investigations (repeated Chirp and side-scan surveys) over sites within the near coastal zone are an effective management tool for the submerged archaeological resource. Sites lying in shallow waters, close to anthropogenic influences such as sewage outfalls and shipping channels, can be rapidly and cost-effectively monitored using a combined array of Chirp and side-scan sonar.

The archaeogeophysical case studies of the designated *Mary Rose* and *Invincible* sites indicate seismic reflection surveys can detail the true areal extent of site. In both cases, the extent of site defined by the geophysical surveys is greater than that predicted by previous diver-based archaeological surveys. Currently, the Protection of Wrecks Act 1973 restricts unauthorised interference within a radius of 50m to 300m around designated sites. The *Mary Rose* site extends a minimum of 70m to the west of the excavated area and the *Invincible* site exceeds diver's estimation of the areal extent by a minimum of 20m, scales on the same order as those currently protected by legislation. A truer representation of the extent of site can therefore be estimated from non-intrusive geophysical investigations.

In many respects, success in the application of high-resolution reflection seismology to marine archaeology in the long term depends on the acceptance of method by the archaeological community. Marine geophysical surveying can never replace the discipline of underwater archaeological excavation, but has enormous potential as a management technique. Much depends on the attitude of government agencies (at local and national level) as to the future role of marine geophysical surveying in underwater archaeology.

9.3 Further work

In order to obtain optimum resolution *and* penetration, the Chirp pulse is a wideband swept-frequency source with a Gaussian-shaped power spectrum. However, an inherent problem with the swept-frequency source is polarity switching associated with small vertical and lateral impedance changes at the seafloor. The inconsistency in polarity information from Chirp reflection data causes problems in determining reflection coefficient polarities when characterising sub-bottom materials/horizons. One method of extracting true polarities from Chirp sub-bottom data would be to lower the dominant frequency and bandwidth of the source-signature, thereby reducing the destructive interference effects of the high-frequency component. Reducing the frequency content of the Chirp source would also allow a coarser sampling interval to be used. Both these factors would aid in determining true polarity information. Using this method, a full high-resolution survey may be conducted using the conventional wideband source. A select area may then be re-surveyed using the lower frequency, narrow-band source, thereby acquiring both high-resolution data to aid interpretation and low-resolution data to aid reflection coefficient calculation. The addition of this option to the current Chirp system would require minimal research and development costs, and would aid the application of Chirp technology to characterisation of sub-bottom materials.

The investigation of metal-hulled vessels and wooden vessels with metallic components or ordnance, would be aided by the addition of a marine magnetometer to survey equipment. Ideally a fourth, albeit expensive, addition would be a swath bathymetry system providing seafloor topography with centimetric resolution. However, additional survey systems inherently imply more data, and so increase survey, processing and interpretation times and costs.

As with any research applicable to outside disciplines, one problem encountered is in relaying the results and potential applications to the user community. The future role of high-resolution geophysical surveying in the realm of marine archaeology is dependent upon acceptance of this investigative technique by the archaeological community. The archaeologist's perception of geophysics is sometimes dismissive, as often, no tangible or physical result is apparent. This perception has to change for geophysics to be accepted as a valid and appropriate method for the investigation of archaeological sites. Therefore, future work in this area may be best served by relaying the available techniques and results to the archaeological community, whether this is by publication, conference presentation or ideally, collaborative research with archaeologists.

Appendix

A.1 *FORTRAN 77 code to process navigation data (position.f)*

This code reads the edited HYPACK™ (ship-board navigation package) file, giving the boat's position in seconds since the start of day and writes an output file containing easting, northing and the time in hours, minutes and seconds to match the time fixes on the Chirp/side-scan data.

```
      program position

      parameter (isize=#)

c     WHERE # = NUMBER OF LINES IN INPUT FILE

      real x(isize),y(isize),t(isize),ts(isize)
      integer th(isize),tm(isize)
      i=1
      open(unit=1,file='*.dat')
      open(unit=2,file='*.xyt')

c     WHERE *.dat = INPUT FILE
c     *.xyt = OUTPUT FILE

      do while (i .le. isize)
      read (1,*) x(i),y(i),t(i)

c HOUR CONVERSION

      th(i)=t(i)/3600
      rest=3600*th(i)
      remainder=t(i)-rest

c MINUTE CONVERSION

      tm(i)=remainder/60
      rest2=60*tm(i)
      remainder2=t(i)-rest-rest2

c SECOND CONVERSION

      ts(i)=remainder2
      print *, ts(i)
      i=i+1
      end do
      write (2,50) (x(i),y(i),th(i),tm(i),ts(i),i=1,isize)
50    format (f9.2,3x,f9.2,3x,I2,1x,I2,1x,f11.2)
      close(unit=1)
      close(unit=2)
      end
```

A.2 *Amplitude analysis: C-shell script "maxmin"*

This code processes the output from the *Amplitude Scanning* algorithm in ProMAX™ 6.0 and outputs a 2-column ASCII file containing the trace number and maximum interpolated amplitude value. The code then combines the output file with the corresponding navigation file to produce a 4-column ASCII file (trace number, northing, easting, amplitude) which can be used to plot 2D or 3D amplitude contour plots in a user-defined range.

```
#       code reads output file from Amplitude Scanning algorithm in ProMAX
#       and writes a 2-column ASCII file containing trace number and the maximum
#       amplitude defined value from the use-defined time window.

awk '/CDP=/' ifn > ifn.cdp

#       where ifn is the output file from ProMAX

awk '{print $2}' ifn.cdp > cdp
rm -f ifn.cdp
awk '/Maximum/' ifn > ifn.max
awk '{print $4}' ifn.max > max
rm -f ifn.max
paste cdp max > ifn.ca

#       code combines processed navigation data with amplitude data
#       and writes a 4-column ASCII file of: trace number, northing, easting and maximum
#       amplitude for importation into GMT
#       note: navigation file and amplitude data must be in the same directory

paste fn.xy ifn.ca > fn.xyca
awk '{print $3, $1, $2, $4}' fn.xyca > fn.cxya
rm -f fn.xyca
```

Archaeological Diving Unit (A.D.U.), 1997. The Protection of Wrecks Act, 1973. http://www.standrews.ac.uk/~www_shir/deswreck.html

Adams, J.R., 1988. Unpublished Internal Report, Mary Rose Trust, Portsmouth.

Akal, T., 1972. The relationship between the physical properties of underwater sediments that effect bottom reflections. Marine Geology, 13: 251-266.

Anstey, N.A., 1977. Seismic interpretation: the physical aspects. International Human Rights Development Corporation, Boston.

Anstey, N.A., 1981. Seismic Prospecting Instruments: Signal Characteristics and Instrument Specifications. Geoexploration Monographs, 1. Gebruder Borntraeger, Berlin.

Belderson, R.H., Johnson, M.A. and Kenyon, N.H., 1982. Bedforms. In: A.H. Stride (Editor), Offshore tidal sands: processes and deposits. Chapman and Hall, London, pp. 27-57.

Bingeman, J.M., 1981. HMS *Invincible* (1758) wreck site. International Journal of Nautical Archaeology, 10(2): 154-156.

Bingeman, J.M., 1985. Interim reports on artefacts recovered from *Invincible* (1758) between 1979 and 1984. International Journal of Nautical Archaeology, 14(3): 191-210.

Bingeman, J.M., 1990. 1990 Report: *Invincible* Wreck Site. Internal Report.

Bingeman, J.M., 1996. *Invincible* (1758) historic wreck site damage report following the grounding of *MV Amer VED* on 19th November 1996. Report to the Department for Culture, Media and Sport.

Bull, J.M., Quinn, R. and Dix, J.K., *in press.* Reflection coefficient calculation from marine high-resolution seismic reflection (Chirp) data. Marine Geophysical Researches.

Canales, A., 1984. Random Noise Reduction, 54th Annual Conference. Society of Exploration Geophysicists, Atlanta, Georgia.

Caston, G.F., 1979. Wreck marks: indicators of net sand transport. Marine Geology, 33: 193-204.

Chauhan, O.S. and Almeida, F., 1988. Geophysical tools as a tool to explore submerged marine archaeological sites. In: S.R. Rao (Editor), Marine Archaeology of Indian Ocean Countries. National Institute of Oceanography, Goa, pp. 3-5.

Chapman, R.D. and Scott, H.D., 1964. Surface backscattering measured over an extended range of frequencies and grazing angles. J. Acoust. Soc. Am. 36: 1735-1737.

Clarebout, J.F., 1976. Fundamentals of Geophysical Data Processing: With applications to Petroleum Prospecting. McGraw-Hill, International Series in the Earth and Planetary Sciences.

Clay, C.S., 1977. Acoustical Oceanography. John Wiley and Sons, USA.

Cleere, H., 1989. Archaeological heritage management in the modern world, 9. Unwin Hyman, London.

Cremer, L., Heckl, M. and Ungar, E.E., 1973. Structure-borne sound: structural vibrations and sound radiation at audible frequencies. Springer, Berlin.

Department of Environment, 1990. Planning Policy Guidance Note 16: Archaeology and Planning.

Department of Environment, 1992. Planning Policy Guidance Note 20: Coastal Planning.

Dobbs, C.T.C., 1995. The raising of the *Mary Rose*: Archaeology and salvage combined, Underwater Technology, pp. 29-35.

English Heritage, 1996. The National Inventory of Maritime Archaeology for England. Royal Commission on the Historical Monuments of England.

Ferrari, B., 1995. Integrated Management of Archaeology in Coastal Waters. In Berry, Q. and Brown, W. (Eds.), Managing Ancient Monuments: An Integrated Approach. Clwyd.

Fish, J.P. and Carr, A.H., 1990. Sound Underwater Images. Lower Cape Publishing, Orleans, MA.

Flinn, R.A. and Trojan, P.K., 1981. Engineering materials and their applications. Houghton Mifflin, Boston.

Frey, D., 1971. Sub-bottom survey of Porto Longo Harbour, Peleponnesus, Greece. The International Journal of Nautical Archaeology, 1: 170-175.

Gulunay, N., 1986. FX-deconvolution and the complex Wiener prediction filter for random noise reduction, 56th Annual Conference. Society of Exploration Geophysicists, Houston, Texas.

Hamilton, E.L., 1980. Geoacoustic modeling of the seafloor. Journal of the Acoustical Society of America, **68**(5): 1313-1340.

Hearmon, R.F.S., 1948. The elasticity of wood and plywood. His Majesty's Stationary Office, London.

Hobbs, C.H., Blanton, D.B. Gammisch, R.A. and Broadwater, J., 1994. A marine archaeological reconnaissance survey using side-scan sonar, Jamestown, Virginia, USA. Journal of Coastal Research, 10(2): 351-359.

Hunter, J. and Ralston, I. (Editors), 1993. Archaeological resource management in the UK: an introduction. Sutton, Stroud.

Jackson, D.R. and Briggs, K.B., 1992. High-frequency bottom scattering: Roughness versus volume scattering. Journal of the Acoustical Society of America, **92**(2): 962-977.

Jenkins, F.A. and White, H.E., 1957. Fundamentals of Optics. McGraw-Hill, New York.

Joint Nautical Archaeology Policy Committee (JNAPC), 1989. Heritage at Sea: Proposals for the better protection of archaeological sites underwater.

Kearey, P. and Brooks, M., 1991. An Introduction to Geophysical Exploration, 2nd Edition. Blackwell Sciences Ltd..

Kallweit, R.S. and Wood, L.C., 1982. The limits of resolution of zero-phase wavelets. Geophysics, 47: 1035-1046.

Koefoed, O., 1981. Aspects of vertical seismic resolution. Geophysical Prospecting, 29: 21-30.

Kuperman, W.A., 1990. Coherent component of specular reflection and transmission at a randomly rough two-fluid interface. J. Acoust. Soc. Am., 58: 365-370.

Lavery, B., 1988. The Royal Navy's first *Invincible*. Invincible Conservations Ltd., Portsmouth.

LeBlanc, L.R., Mayer, L., Rufino, M., Schock, S.G. and King, J., 1992a. Marine sediment classification using Chirp sonar. Journal of the Acoustical Society of America, 91: 107-115.

LeBlanc, L.R., Panda, S. and Schock, S.G., 1992b. Sonar attenuation modelling for classification of marine sediments. Journal of the Acoustical Society of America, 91: 116-126.

Mayer, L., 1979. The origin of fine scale acoustic stratigraphy in deep-sea carbonates. Journal of Geophysical Research, 84: 6177-6184.

Mazel, C., 1985. Technology for Marine Archaeology. Oceanus, 28(1): 85-89.

McGee, T.M., 1990. The use of marine seismic profiling for environmental assessment. Geophysical Prospecting, 38: 861-880.

McGhee, M.S., Luyendyk, B.P. and Boegmann, D.E., 1968. Location of an ancient Roman shipwreck by modern acoustic techniques - a critical look at marine technology, Marine Technology Society, 4th Annual Conference, Washington, D.C.

McKee, A., 1982. How we found the *Mary Rose*. Souvenir Press, London.

Orsi, T.H. and Dunn, D.A., 1991. Correlations between sound velocity and related properties of glacio marine sediments: Barents Sea. Geo-Marine Letters, 11: 79-83.

Panda, S., LeBlanc, L.R. and Schock, S.G., 1994. Sediment classification based on impedance and attenuation estimation. Journal of the Acoustical Society of America, 95: 3022-3055.

Parent, M.D. and O' Brien, T.F., 1993. Linear swept FM (Chirp) sonar seafloor imaging system, Sea Technology, 49-55.

Peace, R.M., *in press.* The Nature, Scale and Pace of Coastal Change between Wootton Creek and Ryde Pier. In Tomalin, D.A. (Ed.), Wootton Haven: Coastal and Port Archaeology in a Dynamic Environment.

ProMAX™ User Manual 6.0., 1995. Advance Geophysical Corporation.

Quinn, R., Bull, J.M. and Dix, J.K., 1997a. Buried scour marks as indicators of palaeo-current direction. Marine Geology, 140: 405-413.

Quinn, R., Bull, J.M. and Dix, J.K., 1997b. Imaging Wooden Artefacts using Chirp Sources. Archaeological Prospection, 4: 25-35.

Quinn, R., Bull, J.M. and Dix, J.K., *in review.* Optimal processing of marine high-resolution seismic reflection (Chirp) data. Marine Geophysical Researches.

Quinn, R., Bull, J.M., Dix, J.K. and Adams, J.R., 1997c. The *Mary Rose* site - geophysical evidence for palaeo-scour marks. The International Journal of Nautical Archaeology, 26(1): 3-16.

Quinn, R., Dix, J.K., Bull, J.M. and Adams, J.R., *in press.* The *Invincible* (1758) site - an integrated geophysical assessment. The International Journal of Nautical Archaeology.

Rao, T.C.S., 1988. Geophysical techniques to locate pre-historic sites and artefacts on the continental shelf. In: S.R. Rao (Editor), Marine Archaeology in Indian Ocean Countries. National Institute of Oceanography, Goa, pp. 73-77.

Redknap, M., 1990. Surveying for underwater archaeological sites: signs in the sands. The Hydrographic Journal, 58: 11-16.

Richardson, P.D., 1968. The generation of scour marks near obstacles. Journal of Sedimentary Petrology, 38(4): 965-970.

Richardson, M.D. and Young, D.K., 1980. Geoacoustic models and bioturbation. Marine Geology, 38: 205-218.

Richardson, M.D and Briggs, K.B., 1996. In situ and laboratory geoacoustic measurements in soft mud and hard-packed sand sediments: Implications for high-frequency acoustic propagation and scattering. Geo-Marine Letters, 16: 196-203.

Ricker, N., 1953. Wavelet contraction, wavelet expansion, and the control of seismic resolution. Geophysics, 18: 769-792.

Rule, M.H., 1982. The *Mary Rose*: the excavation and raising of Henry VIII's flagship. Conway Maritime Press, London.

Schock, S.G., 1996. Predicting vertical seismic profiles of sediment properties from seismograms, Oceanology International, Brighton, 1-20.

Schock, S.G and LeBlanc, L.R., 1990. Chirp sonar: a new technology for sub-bottom profiling, Sea Technology, 35-39.

Schock, S.G., LeBlanc, L.R. and Mayer, L.A., 1989. Chirp subbottom profiler for quantitative sediment analysis. Geophysics, 54: 445-450.

Schock, S.G., LeBlanc, L.R. and Panda, S., 1994. Spatial and temporal design considerations for a marine sediment classification sonar. IEEE Journal of Oceanic Engineering, 19(3): 406-415.

Sheriff, R.E. and Geldart, L.P., 1995. Exploration Seismology, Cambridge University Press.

Smith, W.F., 1986. Principles of material science and engineering. McGraw Hill.

Slowey, N.C., Bryant, W.R. and Lambert, D.N., 1996. Comparison of high-resolution seismic profiles and the geoacoustic properties of Eckernforde Bay sediments. Geo-Marine Letters, 16: 240-248.

Spence, G.D., Minshull, T.A. and Fink, C., 1995. Seismic studies of methane gas hydrate, offshore Vancouver Island. In: B. Carson, Westbrook, G.K., Musgrave, R.J. and Suess, E. (Editors), Proceedings of the Ocean Drilling Program, Scientific Results, 163-174.

Taner, M.T., Koehler, F. and Sheriff, R.E., 1979. Complex seismic trace analysis. Geophysics, 44(6): 1041-1063.

Warner, M.R., 1990. Absolute reflection coefficients from deep seismic reflections. Tectonophysics, 173: 15-23.

Weidmann, G., Lewis, L. and Reid, R., 1990. Structural Materials. Materials in Action Series, Open University. Butterworth Scientific Ltd., London.

Werner, F. and Newton, R.S., 1975. The pattern of large-scale bedforms in the Langeland Belt (Baltic Sea). Marine Geology, 19: 29-59.

Werner, F., Unsold, G., Koopmann, B. and Stefanon, A., 1980. Field observations and flume experiments on the nature of comet marks. Sedimentary Geology, 26: 233-262.

West, I.M., 1980. Geology of the Solent Estuarine System. NERC Publication Series C, 22: 6-17.

Widess, M.B., 1973. How thin is a thin bed? Geophysics, 38: 1176-1180.

Wilson, M.A., Godfrey, I.M., Hanna, J.V., Quezada, R.A. and Finnie, K.M., 1993. The degradation of wood in old Indian Ocean shipwrecks. Organic Geochemistry, 20(5): 599-610.

Wynn, J.C., 1986. Archaeological Prospection. Geophysics, 51(3): 533-537.

Yilmaz, O., 1987. Seismic data processing. Investigations in Geophysics, No. 2. Society of Exploration Geophysicists, Tulsa, Oklahoma.